ELECTROLESS DEPOSITION OF AMORPHOUS IRON-ALLOY COATINGS

by

JACOB K. BLICKENSDERFER

Submitted in partial fulfillment of the requirements

for the degree of Doctor of Philosophy

Thesis Advisor: Professor Rohan Akolkar

Department of Chemical and Biomolecular Engineering

CASE WESTERN RESERVE UNIVERSITY

January, 2018

CASE WESTERN RESERVE UNIVERSITY

SCHOOL OF GRADUATE STUDIES

We hereby approve the dissertation of

Jacob K. Blickensderfer

Candidate for the Doctor of Philosophy degree*

(signed) Rohan Akolkar
(chair of the committee)

Heidi Martin

Mark De Guire

Uziel Landau

Date: 10-17-17

*We also certify that written approval has been obtained for any proprietary material contained therein.

DEDICATION

This thesis is dedicated to my family for always showing love, support and patience.

TABLE OF CONTENTS

DEDICATION **2**

TABLE OF CONTENTS **3**

LIST OF TABLES **5**

LIST OF FIGURES **6**

ACKNOWLEDGEMENTS **12**

LIST OF SYMBOLS **13**

CHAPTER 1. INTRODUCTION **19**

1.1 Amorphous Nickel Alloys – Use and Future Outlook 19
1.2 Amorphous Iron-Alloys for Potentially Replacing Nickel-Alloys 20
1.3 Electroless Iron Deposition using Borohydride and Hypophosphite Reductants 24
1.4 Fundamentals of Palladium Activation 27
1.5 Objectives 30

CHAPTER 2. DIRECT ELECTROLESS DEPOSITION OF IRON BORON ON COPPER **32**

2.1 Experimental Procedure 35
2.1.1 Materials *35*
2.1.2 Methods *36*
2.2 Development of Activation-Free Electroless FeB Process 38
2.2.1 Limitations of Previously Reported Electroless FeB Process *38*
2.2.2 Development of Activation-Free Electroless FeB Deposition Process *43*
2.3 Materials Characterization of Electroless FeB Films 47
2.4 Conclusions 53

CHAPTER 3. ROLE OF PALLADIUM ACTIVATION IN ELECTROLESS DEPOSITION OF IRON PHOSPHORUS COATINGS **54**

3.1 Experimental Procedure 57
3.1.1 Materials and Electrolyte Composition *57*
3.1.2 Mixed Potential Measurements During Electroless FeP Deposition *58*
3.1.3 Polarization Measurements of Hypophosphite Oxidation *59*
3.1.4 Polarization Measurements of the Hydrogen Evolution Reaction *59*
3.1.5 Polarization Measurements of Iron Deposition *60*
3.2 Critical Role of Pd-Activation in Enabling FeP Deposition 63
3.3 Polarization Studies to Characterize the Effect of Substrate Pd-Activation on the Electroless FeP Mixed Potential 67
3.3.1 Hypophosphite Oxidation on Pd-Activated Cu Substrates *67*
3.3.2 Polarization Behavior of the Iron Deposition Half-Reaction *68*

3.3.3 Predicting the Electroless FeP Mixed Potential by Applying Mixed Potential Theory to Partial Polarization Curves *74*
3.5 CONCLUSIONS 78

CHAPTER 4. MATHEMATICAL MODEL FOR THE PREDICTION OF THE SURFACE MIXED POTENTIAL DURING EARLY STAGES OF ELECTROLESS IRON DEPOSITION 80

4.1 EXPERIMENTAL PROCEDURE 81
4.1.1 Materials and Electrolyte Composition *81*
4.1.2 Methods *82*
4.2 MATHEMATICAL MODEL FOR PREDICTING THE SURFACE MIXED POTENTIAL DURING EARLY STAGE ELECTROLESS FE DEPOSITION ON PD-ACTIVATED CU 84
4.2.1 Rates of Anodic and Cathodic Reactions during Electroless Fe Deposition *84*
4.2.2 Current Density – Mixed Potential Relationship *87*
4.2.3 Experimental Determination of the Kinetics Parameters in Eq. [4.20] *91*
4.2.4 Predicting the Electroless Mixed Potential as a Function of the Palladium Surface Coverage .. *96*
4.3 TIME EVOLUTION OF THE PD SURFACE COVERAGE DURING ACTIVATION TREATMENT 98
4.3.1 Mixed Potential Transients during Palladium Activation *98*
4.3.2 Kinetics Model of the Pd Surface Action Process *103*
4.3.3 Modeling Pd Coverage as a Function of Pd-Activation Time 107
4.4 MATHEMATICAL MODEL FOR PREDICTING THE MIXED POTENTIAL DURING ELECTROLESS FEP INITIATION ON A PD-ACTIVATED CU SUBSTRATE. 109
4.5 CONCLUSIONS 111

CHAPTER 5. CONCLUSIONS AND FUTURE WORK 113

5.1 CONCLUSIONS 113
5.2 OUTLOOK AND FUTURE WORK 114

APPENDIX A. CORROSION RESISTANCE OF ELECTRODEPOSITED AMORPHOUS IRON PHOSPHOROUS 117

A.1 EXPERIMENTAL PROCEDURE 117
A.1.1 Materials and Electrolyte Composition *117*
A.1.2 Methods *119*
A.2 CORROSION RATE OF ELECTRODEPOSITED AMORPHOUS FEP 119
A.3 CONCLUSIONS 121

BIBLIOGRAPHY 122

LIST OF TABLES

Table I: System Parameters for Modelling Initial Electroless FeP Mixed Potential as a Function of Pd-Activation Time……..……. 111

LIST OF FIGURES

Figure 1.1: The Iron Pillar of Delhi. The chemical composition of this iron pillar, specifically its P-content (0.15 at. %), has rendered its resistance to corrosion for approximately sixteen centuries. The excellent corrosion resistance has spurred interest in the corrosion behavior of various iron-alloys……..…….... 21

Figure 1.2: Schematic for the deposition of Fe on Cu using an Al sacrificial anode.[36] As Al dissolves, electrons released by the oxidation reaction travel from the sacrificial anode through an external circuit into the Cu substrate. At the Cu substrate, these electrons are consumed in the iron plating reaction. …… 23

Figure 1.3: Schematic representation of the deposition of Fe on Pd-activated Cu using sodium borohydride (BH_4^-) as the reducing agent. Borohydride is oxidized on the catalytically active substrate and electrons from this oxidation reaction travel through the substrate to be subsequently used in iron plating…….……. 25

Figure 1.4: Schematic representation of the deposition of Fe on Pd-activated Cu using sodium hypophosphite as a reducing agent. Hypophosphite is oxidized on the catalytically active substrate and electrons from this oxidation travel through the substrate to be subsequently used in iron deposition. If the electrolyte composition is optimally chosen, the oxidation half reaction also proceeds rapidly on the deposited Fe surface. This allows sustained electroless plating for thick-film fabrication……..… 27

Figure 1.5: Schematic of the Pd-activation process. The copper substrate is immersed in an acidified $PdCl_2$ electrolyte where the Cu spontaneously dissolves. Electrons from this dissolution (oxidation) reaction are subsequently used to reduce Pd^{2+} to metallic Pd. This process continues until the substrate is either physically removed from the activation electrolyte or the substrate surface is completely covered by Pd so that dissolution of underlying Cu is not possible……. 28

Figure 2.1: Schematic for of the electroless deposition of FeB on Cu. Borohydride (BH_4^-) is oxidized to form metaborate ions (BO_2^-), releasing electrons (e^-). These electrons are subsequently used to reduce Fe^{2+} to metallic iron (Fe^0) on the copper substrate. The potential at which these reactions occur is called the mixed potential (E_{mix}) and is measured with respect to a reference electrode in a two-electrode configuration…….…….. 34

Figure 2.2: Polarization curves for borohydride (BH) oxidation on Cu (blue) and on Fe (red), as well as the polarization curve for the net reduction current (black). Borohydride (BH) oxidation was studied using a 'Fe^{2+}-free' bath containing low (0.050 M) borohydride content, and the net reduction current was studied using a 'borohydride-free' bath. Application of the mixed potential theory to the oxidation and reduction half-reactions indicates that electroless Fe nucleation on the Cu substrate is thermodynamically possible, but growth on the freshly nucleated iron layer is prohibited because the non-catalytic iron surface shifts the mixed potential into an anodic region where iron deposition does not occur.[61]…….…. 42

Figure 2.3: Effect of varying borohydride concentration on the mixed potential during electroless FeB plating. Increasing borohydride concentration shifts the mixed potential cathodically as desired.[61]……..……. 44

Figure 2.4: Polarization curves for borohydride (BH) oxidation on Cu (blue) and on Fe (red), as well as the polarization curve for the net reduction current (black). Borohydride (BH) oxidation was studied using a 'Fe^{2+}-free' bath containing high (0.300 M) borohydride content, and the net reduction current was studied using a 'borohydride-free' bath. Application of the mixed potential theory to the oxidation and reduction half-reactions indicates that electroless Fe deposition can now be sustained as the borohydride begins to oxidize on freshly plated iron. This is due to the cathodic shift of the mixed potential compared to the previously used low (0.050 M) borohydride concentration electrolyte. This puts the mixed potential on iron in a region where iron deposition is thermodynamically permitted.[61]……...……..… 46

Figure 2.5: FIB cross-section of an electroless FeB film plated over a PVD-Cu substrate, imaged using SEM. Electroless plating time is 30 min leading to an average plating rate of 0.24 μm/hr. The electroless bath contained 0.30 M sodium borohydride, 0.05 M ferrous ammonium sulfate, 0.13 M potassium sodium tartrate and 0.05 M boric acid. Bath pH was 11 and bath temperature was 41 ºC.[61]……..……... 48

Figure 2.6: XPS of electroless FeB films obtained from the same bath as in Figure 2.5, *i.e.*, using a high (0.30 M) concentration of borohydride. XPS confirms Fe (at 69.2 at. %) and B (at 30.8 at. %). The oxygen peak is likely due to surface oxidation upon air exposure....49

Figure 2.7: XRD of electroless FeB films obtained from the same bath as in Figure 2.5, *i.e.*, using a high (0.30 M) concentration of borohydride. The lack of an iron peak is indicative of amorphous structure. The strong XRD peaks detected at 2θ = 43.6, 50.7 and 74.3 are attributed to the polycrystalline Cu substrate used to grow the electroless FeB films. The weak XRD peaks detected at 2θ = 45.6 and 48.4 (inset) are attributed to iron and boron surface oxides, respectively.[61]…… 50

Figure 2.8: Electrochemical corrosion tests comparing electroless FeB films produced from the same bath as in Figure 2.5, *i.e.*, using a high (0.300 M) concentration of borohydride. Polarization tests were conducted in a 3.5 wt.% NaCl solution. Tests indicate a corrosion current density of 31.1 μA/cm^2 for FeB compared to 3.6 μA/cm^2 for NiP. As comparison, the corrosion current density of pure Fe metal is typically ~600 μA/cm^2 and thus FeB has acceptably high corrosion resistance.[61]…….……... 52

Figure 3.1: Schematic of the process used to obtain iron deposition polarization in the complete electroless FeP system. First, iron was deposited potentiostatically on a platinum RDE from a complete electroless FeP electrolyte (a). The RDE with deposited iron was then removed from the complete electroless FeP electrolyte and placed in an acid electrolyte (b) where all of the plated iron was dissolved into Fe^{2+} potentiostatically (c). The Fe^{2+} was then further oxidized to Fe^{3+} and the limiting current of this reaction was measured to determine the initial amount of iron plated (d)…….……..… 61

Figure 3.2: (a) Mixed potential of a Pd-activated substrate in an electroless FeP electrolyte as a function to the substrate Pd-activation time. As activation time increases, the mixed potential shifts in the negative (cathodic) direction. The Pourbaix diagram for iron (b) indicates that at mixed potentials anodic to -1.01 V vs SHE (at pH~15, *red dot*), metallic iron deposition is thermodynamically prohibited [*red region* of (a)]. With sufficient activation time, the mixed potential shifts cathodic enough [*blue region* of (a)] to be in the region where metallic iron deposition is favored. RDE rotation speed = 2000 RPM……...…….…….…. 64

Figure 3.3: XPS depth profiling of an electroless FeP film (mixed potential = -0.95 V vs SHE) deposited after activating the substrate with Pd for a short activation time (60 s). XPS analysis shows that the film is a surface iron oxide layer with a thickness in the range of about 20 nm. The lack of any metallic iron plating is consistent with the analysis presented in Figure 3.2b. Process conditions during electroless deposition were electrode area = 0.196 cm^2; RDE rotation speed = 2000 RPM. Electroless bath composition is provided in section 3.1.1……...…… 65

Figure 3.4: XPS depth profiling of an electroless FeP film (mixed potential = -1.05 V vs SHE) deposited after activating the Cu substrate with Pd for 1000 s. XPS analysis shows that, while there is a surface oxide present due to air exposure, the bulk of the film is metallic iron. This result is consistent with the analysis using the Pourbaix diagram presented in Figure 3.2b. Electroless deposition conditions: Electrode area = 0.196 cm^2; RDE rotation speed = 2000 RPM. Electroless bath composition is provided in section 3.1.1…… 66

Figure 3.5: Hypophosphite oxidation polarization on a Cu substrate after activating it with Pd for various activation times. As Pd-activation time increases, the coverage of Pd on the substrate increases. This increase in Pd coverage leads to a higher hypophosphite oxidation current. Electrode area = 0.196 cm^2; RDE rotation speed = 2000 RPM. Electrolyte composition is discussed in section 3.1.1…….. 68

Figure 3.6: The expected limiting current density, determined via the Levich equation, as a function of the Fe^{2+} concentration (*red*) is compared to that experimentally measured on an RDE using an electrolyte containing the specified concentration of Fe^{2+} (*blue*). Good agreement between the two is noted. Electrode area = 0.196 cm^2; RDE rotation speed = 2000 RPM. Electrolyte contained 0.6 M H_2SO_4 (pH = 0.2) with Fe^{2+} concentrations ranging from 0.01 mM to 250 mM…….... 71

Figure 3.7: For the three trials, iron was first deposited potentiostatically (-1.05 V vs SHE) from a electroless FeP electrolyte and the weight gain of the working electrode was measured (*blue*). The deposited iron was then dissolved in an acid electrolyte and the limiting current of Fe^{2+} oxidation was measured. Based on this limiting current, the plated Fe mass was calculated (*red*). The two methods of mass measurement match reasonably well. Electrode area = 0.196 cm^2; RDE rotation speed = 2000 RPM……..... 72

Figure 3.8: Polarization behavior of iron deposition in an electroless FeP plating electrolyte. The behavior was determined using the method described in section 3.1.5. Iron deposition reaches a limiting current at cathodic potentials because of diffusion limitations. Electrode area = 0.196 cm^2; RDE rotation speed = 2000 RPM…… 74

Figure 3.9: Polarization curves for all cathodic and anodic reactions on a substrate that was Pd-activated for 100 s (*i.e.*, low Pd coverage). In order to achieve charge conservation, the net cathodic currents must match the net anodic currents. This occurs at -0.98 V vs SHE, which is the estimated mixed potential of the system. This potential is not cathodic enough to initiate the electroless deposition of Fe – a prediction consistent with observations in Figure 3.2 and 3.3. Electrode area = 0.196 cm^2; RDE rotation speed = 2000 RPM…….. 76

Figure 3.10: Polarization curves of cathodic and anodic reactions on a Cu substrate activated with Pd for 1000 s (*i.e.*, high Pd coverage). Charge conservation requires that the net cathodic current must be equal to the net anodic current. This occurs at -1.04 V vs SHE which is the mixed potential of the electroless Fe deposition system. Thus, the mixed potential is in a region where Fe^{2+} reduction to Fe occurs, and thus electroless Fe deposition is possible. Electrode area = 0.196 cm^2; RDE rotation speed = 2000 RPM…….…… 78

Figure 4.1: Butler-Volmer kinetics for hypophosphite (HP) oxidation on Pd (*blue*). Experimental polarization data (*red*) was collected on a rotating disc electrode (details provided in section 4.1.2). The best fit parameters were: exchange current density ($i_{0,1}$) of 5.92 mA/cm^2 and charge transfer coefficient (α_1) of 1.76…….…… 92

Figure 4.2: Comparison between Bulter-Volmer theory (*blue*) and experimental data (*red*) for the hydrogen (H_2) evolution reaction on Pd and Cu substrates. Experimental polarization data was collected on a rotating disc electrode (details provided in section 4.1.2). The best fit parameters in the Butler-Volmer equation are as follows: exchange current density for H_2 evolution on Pd ($i_{0,3}$) is 0.102 mA/cm^2 and charge transfer coefficient (α_3) is 0.25; exchange current density for H_2 evolution on Cu ($i_{0,4}$) is 0.059 mA/cm^2 and charge transfer coefficient (α_4) is 0.24…….…… 94

Figure 4.3: Tafel kinetics (Eq. 4.19) for the iron deposition partial current during electroless Fe plating (*blue*). Experimental polarization data points were collected on a rotating disc electrode under conditions described in section 4.1.2. Following kinetics parameters provide the best agreement between theory and experiment: exchange current density ($i_{0,5}$) of 0.13 mA/cm^2 and charge transfer coefficient (α_5) of 1.80……..…… 95

Figure 4.4: Model prediction of the surface mixed potential during electroless FeP deposition as a function of the Pd coverage provided by activation. Iron is deposited only in the region where the mixed potential is cathodic to the reduction potential (–0.99 V vs SHE, blue region). When the mixed potential is anodic to the reduction potential (red region), only iron oxide formation is possible as shown in Chapter 3. It is thus inferred that a minimum Pd coverage of 10.6% is required for spontaneous electroless iron deposition under the conditions employed in this study.....……...……. 97

Figure 4.5: Repeated trials showing the change of the surface mixed potential (ΔE_{mix}) over time during Pd-activation of Cu RDE. Results of several trials are shown to highlight the noise associated with the mixed potential measurements. In spite of the noise, the general trends (graduate drift in mixed potential in the positive direction) appear reproducible... 99

Figure 4.6: Experimental data for the change in mixed potential during Pd-activation is shown (*red*, left y-axis). On the right y-axis, the corresponding Pd coverage is shown. Both variables change linearly with respect to time per Eq. 4.48 and Eq. 4.50…….…….. 108

Figure 4.7: Model of the electroless FeP mixed potential as a function of Pd-activation time. The model indicates that the minimum activation time needed to achieve iron deposition is 278 s (shown as *red* dot). Experimental observations have indicated that the minimum activation time necessary for iron deposition is 300 s (section 3.2). Good agreement between model and experimental data is noted……..……..…….. 110

Figure A.1: Mass loss of amorphous FeP (*blue*) and NiP (*red*) in a 3.5 wt. % sodium chloride electrolyte measured using a QCM. Mass loss with time is converted into corresponding corrosion current densities (i_{corr}). The corrosion current density of FeP (i_{corr} = 2.6 µA/cm^2) is within an order of magnitude of the corrosion current density of NiP (i_{corr} = 0.9 µA/cm^2)……..…… 120

ACKNOWLEDGEMENTS

I would like to thank my advisor Professor Rohan Akolkar for the opportunity to work with and learn from him. He has shown dedication to the success, both academically and beyond, of me and all of his students and continuously strives to promote an atmosphere of learning and cooperation.

I also appreciate the many group members of Professor Akolkar's Electrochemical Materials Fabrication Group that I have worked with throughout my graduate studies. Thank you Stephen, Jack, Alan, Ajay, Page, Sherry, Alex, Dai, Kailash, Karun, Ryan, Darshika, Adam and Katie for all of the thought provoking discussions and constant willingness to help a fellow group member.

I was fortunate to have not only support via funding, but also the continued encouragement and technical knowledge of many employees of Atotech. Thank you especially to Yoko and Arnd for always being willing to brainstorm with me.

I want to thank the entire Chemical & Biomolecular Engineering department at Case Western, my committee and the many others who have helped along the way.

Finally, I want to thank my family: my parents, Kelly and Dave, my siblings, Taryn and Nathan, and my grandparents Bob, Marilyn and Pat. They have supported and loved me not just during my graduate studies, but throughout my whole life and made me who I am today.

LIST OF SYMBOLS

A	area
Al	aluminum
BH	borohydride
C_b	bulk concentration
C_O	concentration of oxidized species
Co	cobalt
C_R	concentration of reduced species
C_S	concentration at electrode surface
Cu	copper
D	diffusion coefficient
DI	deionized
e^-	electron
E_{mix}	electroless mixed potential
E_o	equilibrium potential
E_{red}	reduction potential
F	Faraday constant
Fe	iron

FeB	iron boron
FeP	iron phosphorus
FIB	focused ion beam
HER	hydrogen evolution reaction
HP	hypophosphite
I	current
i	current density
I_1	hypophosphite oxidation current on Pd
i_1	hypophosphite oxidation current density on Pd
I_2	hypophosphite oxidation current on Cu
I_3	hydrogen evolution current on Pd
i_3	hydrogen evolution current density on Pd
I_4	hydrogen evolution current on Cu
i_4	hydrogen evolution current density on Cu
I_5	iron deposition current
i_5	iron deposition current density
I_6	Cu oxidation current
i_6	Cu oxidation current density
I_7	Pd deposition current
i_7	Pd deposition current density
i_{corr}	corrosion current density
I_L	limiting current
i_L	limiting current density

i_o	exchange current density
k	first order reaction rate constant
m	mass
M	molar mass
n	number of electrons
Ni	nickel
NiP	nickel phosphorus
O	oxygen
ORR	oxygen reduction reaction
P	phosphorus
PCB	printed circuit board
Pd	palladium
PVD	physical vapor deposition
QCM	quartz crystal microbalance
R	universal gas constant
RDE	rotating disk electrode
SCE	Saturated Calomel Electrode
SEM	scanning electron microscopy
SHE	Standard Hydrogen Electrode
Si	silicon
t	time
T	temperature
TaN	tantalum nitride

$t_{critical}$	minimum Pd-activation time needed for electroless FeP deposition
V_{mix}	mixed potential during Pd-activation
XPS	X-ray photoelectron spectroscopy
XRD	X-ray diffraction
α	charge transfer coefficient
Γ_S	saturation Pd surface concentration
δ	diffusion boundary layer thickness
ΔV_{mix}	change in mixed potential during Pd-activation
η	overpotential
θ_1	Pd coverage during electroless deposition
θ_2	Cu coverage during electroless deposition
θ_3	Pd coverage during Pd-activation
θ_4	Cu coverage during Pd-activation
ν	kinematic viscosity
ω	angular rotation rate

Electroless Deposition of Amorphous Iron-Alloy Coatings

Abstract

by

Jacob K. Blickensderfer

Amorphous iron alloys are a potentially benign alternative for replacing nickel-phosphorus films commonly used in electronics and surface finishing applications. In addition to being environmentally friendly, the amorphous iron alloys provide excellent corrosion resistance, solderability and micro hardness. In this work, electroless deposition of two such iron alloys, i.e., iron boron (FeB) and iron phosphorus (FeP), is investigated.

A process for electroless deposition of FeB without the use of substrate activation is developed. Mixed potential behavior and polarization behavior of individual half-reactions occurring during electroless FeB deposition are characterized, and then used to elucidate the process conditions necessary for activation-free electroless FeB deposition. Corrosion resistance of amorphous FeB films deposited using this newly developed process is tested and the corrosion current is determined to be 31.1 $\mu A/cm^2$, which is an order of magnitude lower than that typical of crystalline Fe deposits.

Unlike FeB deposition, electroless FeP plating critically needs substrate activation by palladium (Pd). The role of substrate (Cu) activation by Pd in enabling electroless FeP deposition is studied in depth. Specifically, it is demonstrated that a critical Pd surface coverage of 10.6% is essential for spontaneous electroless FeP deposition to commence.

Below this critical Pd coverage, the surface is catalytically inactive for FeP deposition. A mechanistic model that incorporates surface heterogeneity due to partial Pd coverage of Cu and the effect of this heterogeneity on electrocatalysis of the reductant oxidation reaction during electroless deposition is presented. Model predictions are compared to experimental observations of the electroless surface mixed potential to gain insights into the mechanism by which Pd catalyzes electroless FeP deposition. Implications of these findings to the optimization of pretreatment and activation processes commonly used in electroless deposition systems is discussed.

CHAPTER 1. Introduction

1.1 Amorphous Nickel Alloys – Use and Future Outlook

Amorphous nickel is widely used as a coating layer in the surface finish and electronics industries. Amorphous nickel films are usually deposited using electrodeposition or electroless deposition. One particular application of interest is the use of amorphous nickel in printed circuit boards (PCB) where it is used to prevent the formation of intermetallic compounds due to the intermixing between the copper substrate and the tin-alloy solder layer during subsequent heat treatment. The prevention of intermetallic compound formation is critical in these PCBs as their formation leads to large stresses in the tin solder layer. Over time, compressive stress caused by intermetallic formation combined with other sources of stress leads to the formation of tin whiskers.[1-4] These whiskers can cause shorts in the PCB, which has been known to create failure in electronics devices in numerous critical applications.[5-7]

In addition to preventing intermetallic compound formation, amorphous nickel alloys also provide a highly solderable surface that protects the underlying layers of the

PCB from mechanical and chemical damage due to their high micro-hardness and corrosion resistance.[8-16] The amorphous characteristic of the Ni-alloys (that provides the aforementioned desirable properties) is achieved through the co-deposition of secondary elements such as boron or phosphorus.

Nickel and nickel-compounds are strong allergens with 28.0% of the adult population suffering from contact allergies with nickel.[17,18] In addition, nickel and nickel compounds have also been shown to be both toxic and carcinogenic.[19,20] Due to this, the use of nickel is regulated in the European Union under the 'Nickel Directive'.[21] Regulation of nickel is likely to become more stringent with time and thus a benign alternative material must be investigated to replace amorphous nickel in PCB applications.

1.2 Amorphous Iron-Alloys for Potentially Replacing Nickel-Alloys

Iron, which is both benign and inexpensive, is one possible candidate to replace amorphous nickel. In spite of the fact that iron itself corrodes spontaneously, some iron-alloys show excellent resistance to corrosion. This corrosion resistance of iron-alloys has been a topic of much interest due largely to the Iron Pillar of Delhi. This iron pillar, shown in Figure 1.1, has had very little corrosive attack despite having existed for over sixteen centuries in a climate where corrosive attack on iron is expected.[22] Numerous studies have investigated this iron pillar and the general consensus among material scientists is that its corrosion resistance is due to the high phosphorus content of the iron pillar.[23-28] Studies of

this pillar have inspired development of corrosion resistant amorphous iron-alloys for industrial applications.

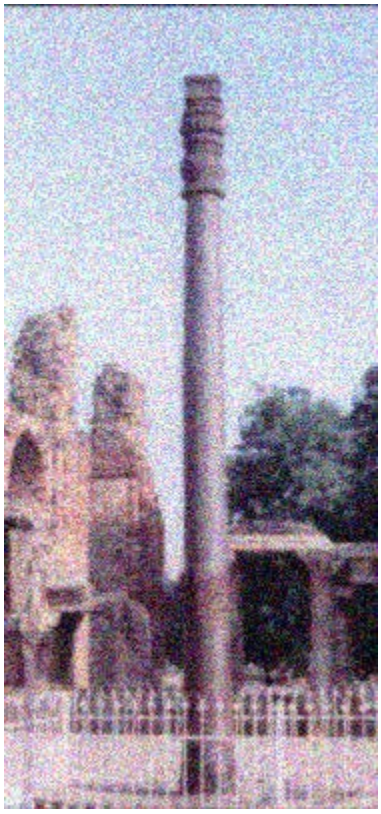

Figure 1.1: The Iron Pillar of Delhi. The chemical composition of this iron pillar, specifically its P-content (0.15 at. %), has rendered its resistance to corrosion for approximately sixteen centuries. The excellent corrosion resistance has spurred interest in the corrosion behavior of various iron-alloys.

Analogous to nickel alloys, it has been shown that alloying iron with a secondary element such as boron or phosphorus leads to iron films that are amorphous and exhibit high micro-hardness, corrosion resistance and solderability.[29-35] These secondary elements are usually incorporated via reactions involving the reducing agent in an electroless plating

process. For example, phosphorus incorporation in electroless iron phosphorus deposition (FeP) results from the use of sodium hypophosphite (NaH_2PO_2) as the reducing agent. The electroless process chemistry is described below.

Electroless iron plating on a copper substrate was first demonstrated by Ruscior and Croiala using an aluminum sacrificial anode in electrical contact with the substrate.[36] The sacrificial anode shifts the potential of the substrate surface to which it is contacted such that electroless Fe plating commences.[36-39] In this process, aluminum is oxidized and dissolves into the solution:

$$Al^0 \rightarrow Al^{3+} + 3e^- \quad [1.1]$$

The electrons from this oxidation reaction are then used in the plating of iron onto the desired substrate:

$$Fe^{2+} + 2e^- \rightarrow Fe^0 \quad [1.2]$$

The net reaction for this system is shown in Eq. 1.3:

$$2Al^0 + 3Fe^{2+} \rightarrow 2Al^{3+} + 3Fe^0 \quad [1.3]$$

This process of Fe deposition via the use of a sacrificial anode is summarized in Figure 1.2. Using a sacrificial anode is not ideal for many processes because it requires an electrical

connection to all surfaces that are to be plated. Such an arrangement utilizing a sacrificial anode contact is not practical in processes which require plating of many small electrically isolated features, such as metallization of PCBs. This process (Figure 1.2) also does not work when using non-conductive substrates. Therefore, there is a need for the development of true electroless processes mediated by solution-phase reducing agents, as discussed below.

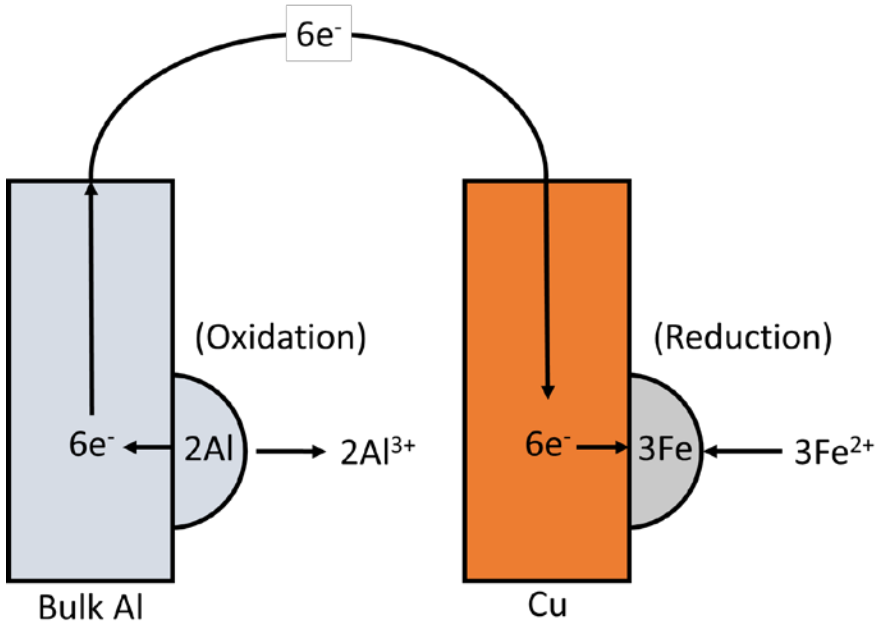

Figure 1.2: Schematic for the deposition of Fe on Cu using an Al sacrificial anode.[36] As Al dissolves, electrons released by the oxidation reaction travel from the sacrificial anode through an external circuit into the Cu substrate. At the Cu substrate, these electrons are consumed in the iron plating reaction.

1.3 Electroless Iron Deposition using Borohydride and Hypophosphite Reductants

In recent years, the use of sodium borohydride as a reducing agent has been studied in the context of electroless Fe deposition. Borohydrides are strong reducing agents and can enable electroless Fe plating without the use of sacrificial anode contacts as discribed by Ruscior and Croiala.[40-42] In this borohydride-based electroless Fe deposition process, borohydride is oxidized on a catalytic palladium (Pd) activated substrate:

$$BH_4^- + 8OH^- \rightarrow BO_2^- + 6H_2O + 8e^- \quad [1.4]$$

The electrons produced in this reaction are then consumed in iron deposition via the same reaction shown in Eq. 1.2. Thus, the net reaction for the electroless borohydride system is shown in Eq. 1.5:

$$BH_4^- + 8OH^- + 4Fe^{2+} \rightarrow BO_2^- + 6H_2O + 4Fe^0 \quad [1.5]$$

The borohydride-enabled electroless Fe deposition process is summarized in Figure 1.3.

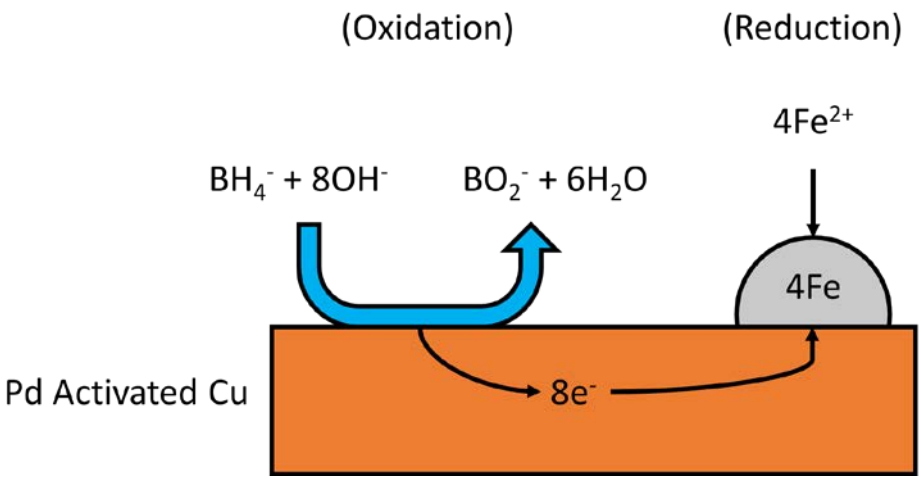

Figure 1.3: Schematic representation of the deposition of Fe on Pd-activated Cu using sodium borohydride (BH_4^-) as the reducing agent. Borohydride is oxidized on the catalytically active substrate and electrons from this oxidation travel through the substrate to be subsequently used in iron deposition.

Unfortunately, due to the toxicity of boron and boron-containing compounds, boron is another element that is under scrutiny and regulation by the European Union, with the Scientific Committee on Consumer Safety proposing regulation of boron by 2010.[43] Thus an electroless process utilizing a hypophosphite-based reductant that provides amorphous FeP alloys is in much demand from the industry.

Electroless FeP deposition without the use of a sacrificial anode has not been achieved to date. The main challenge here is that hypophosphite-based reducing agents are not effectively oxidized on surfaces such as the substrate (typically Cu). Even if palladium-activation is applied, the resulting iron deposit (formed in the initial stages of growth) shuts down further plating because iron is a weak catalyst for the hypophosphite oxidation reaction. Chapter 3 of this thesis describes a new electrolyte formulation for the sustained

electroless deposition of FeP. In a typical hypophosphite-mediated electroless Fe deposition process, hypophosphite is oxidized on a catalytic Pd-activated substrate:

$$H_2PO_2^- + 3OH^- \rightarrow HPO_3^{2-} + 2H_2O + 2e^- \quad [1.6]$$

The oxidation step provides electrons for the deposition of iron (shown in Eq. 1.2). The net reaction for this hypophosphite-based electroless system is shown in Eq. 1.7:

$$Fe^{2+} + H_2PO_2^- + 3OH^- \rightarrow Fe^0 + HPO_3^{2-} + 2H_2O \quad [1.7]$$

The hypophosphite-based electroless iron deposition process is summarized in Figure 1.4. It will be shown in Chapter 3 that, by optimal design of the plating electrolyte composition, reaction 1.6 proceeds favorably both on the Pd-activated substrate as well as the Fe deposited during early stages of the film growth.

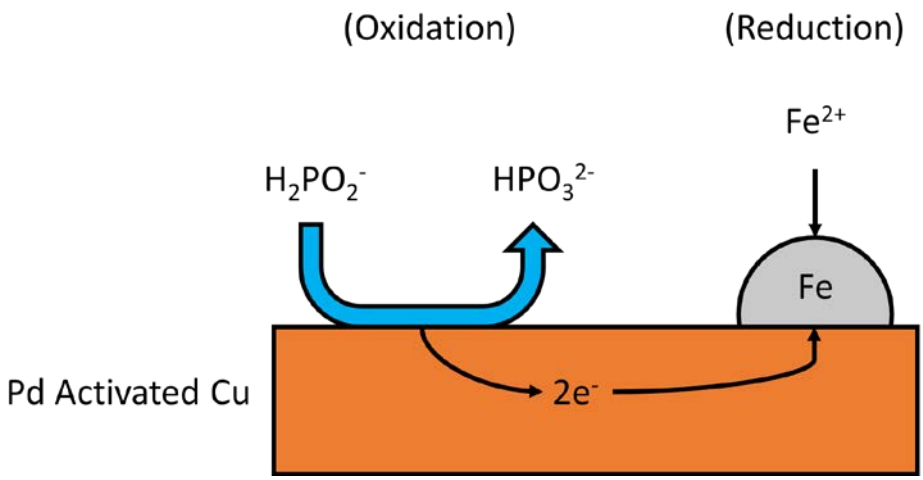

Figure 1.4: Schematic representation of the deposition of Fe on Pd-activated Cu using sodium hypophosphite as a reducing agent. Hypophosphite is oxidized on the catalytically active substrate and electrons from this oxidation travel through the substrate to be subsequently used in iron deposition. If the electrolyte composition is optimally chosen, the oxidation half reaction also proceeds rapidly on the deposited Fe surface. This allows sustained electroless plating for thick-film fabrication.

1.4 Fundamentals of Palladium Activation

For electroless deposition, it is imperative that the substrate be catalytic towards the oxidation of the reducing agent. Palladium activation is a common technique used to impart catalytic activity to an otherwise catalytically inactive substrate. During palladium activation, the substrate (e.g., Cu) is immersed in an acidified Pd^{2+}-containing electrolyte. The less noble copper then dissolves and is spontaneously replaced by the more noble palladium. Copper oxidation proceeds via:

$$Cu^0 \rightarrow Cu^{2+} + 2e^- \qquad [1.8]$$

The electrons released by the copper oxidation reaction are then used in the reduction of the Pd^{2+} from the activation electrolyte. This results in the formation of Pd^0 that gradually covers the substrate surface:

$$Pd^{2+} + 2e^- \rightarrow Pd^0 \quad [1.9]$$

The net reaction for palladium activation is thus shown in Eq. 1.10:

$$Pd^{2+} + Cu^0 \rightarrow Pd^0 + Cu^{2+} \quad [1.10]$$

The entire palladium activation process is summarized in Figure 1.5.

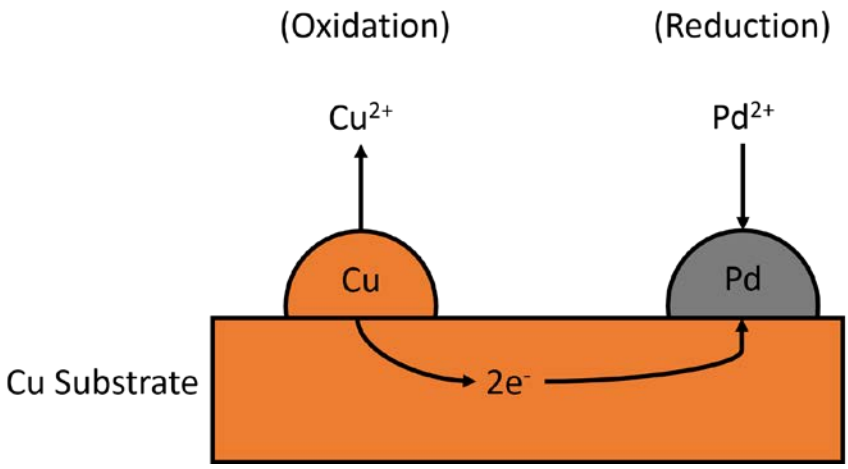

Figure 1.5: Schematic of the Pd-activation process. The copper substrate is immersed in an acidified $PdCl_2$ electrolyte where the Cu spontaneously dissolves. Electrons from this dissolution (oxidation) reaction are subsequently used to reduce Pd^{2+} to metallic Pd. This process continues until the substrate is physically removed from the activation electrolyte or the substrate surface is completely covered by Pd so that dissolution of the underlying Cu is no longer possible.

Ideally, the use of Pd-activation in an electroless process should be limited. Pd-activation adds an additional process step that increases the overall electroless process complexity, decreases throughput and substantially increases the raw material costs. The $PdCl_2$ used for activation is produced by dissolving Pd metal in aqua regia and reacting it with excess chlorides. Pd metal is a platinum group metal that has had an average price of $19,000-$26,000 USD per kg.[44,45] Additionally, the price of this metal is very volatile.[43-45] The volatile nature of the price of palladium stems from its production being primarily limited to just two countries, Russia and South Africa, with each country controlling approximately 40% of the palladium produced in any given year.[45, 47-51] While trade deals and national politics may affect the price of palladium to some extent due to the limited number of large scale producers, an even greater possibility for sudden decrease in the supply of Pd can be due to the instability of the mining industry in South Africa. A lack of safety and economical regulations of the mining industry in South Africa leads to very frequent strikes by miners.[52-54] This, coupled with frequent loss of power from South Africa's inconsistent electric grid often results in decreased Pd production in one of the world's top Pd producers.[52] In addition to supply risks, it is also expected that the demand for Pd will increase as more stringent requirements are made for automobile catalytic converters due to environmental concerns.[45] Increase in demand with a decrease in supply could cause the price of Pd to rapidly increase. As such, in application of surface coatings via electroless deposition (where materials and manufacturing cost must be tightly controlled), the use of $PdCl_2$ in the Pd-activation step must be minimized or ideally completely eliminated. Activator chemistries that minimize Pd use are in fact being developed by major chemical suppliers such as Atotech GmbH.

1.5 Objectives

The specific objectives of the present work are:

1) Develop a process for the electroless deposition of amorphous iron boron (FeB) and iron phosphorus (FeP) alloys as potential replacement for amorphous nickel which is currently used in the electronics and surface finish industries.

2) Use electrochemical polarization measurements to characterize the kinetics of oxidation and reduction reactions, thereby enabling a process for electroless deposition of FeB on copper without the use of a Pd-activation step or a sacrificial anode.

3) Characterize the critical role of Pd-activation in enabling electroless FeP deposition and develop a mechanistic understanding of the effect of substrate activation on the partial reactions during electroless FeP deposition.

4) With the aim of minimizing the Pd utilization during activation needed to catalyze electroless FeP deposition, develop a mathematical model for predicting the minimum Pd surface coverage necessary to catalyze sustained electroless iron deposition.

These objectives are addressed in Chapters 2-4 and key conclusions are summarized in Chapter 5.

In Chapter 2, electrochemical polarization measurements of the oxidation and reduction reactions in the electroless FeB system are reported and these are used to develop

optimal conditions for electroless deposition of FeB without the use of Pd-activation or a sacrificial anode. Films fabricated using this optimized electroless process are characterized via scanning electron microscopy (SEM), X-ray photoelectron spectroscopy (XPS) and X-ray diffraction to understand their composition and amorphous character. In addition, the corrosion resistance behavior of these FeB films is characterized.

In Chapter 3, mixed potential measurement during electroless FeP deposition combined with XPS analysis is used to characterize the role of Pd-activation in enabling electroless FeP deposition. Polarization measurements of oxidation and reduction reactions are used to show how hypophosphite oxidation is effectively catalyzed by Pd-activation. Mixed potential theory is then applied to characterize the effect of Pd-activation time on the surface mixed potential and the ability to initiate electroless Fe plating and sustain its growth.

In Chapter 4, a mathematical process model is developed to correlate the surface Pd coverage and the electroless mixed potential. Relevant kinetics and mass-transport parameters are determined from experimental polarization data. The model predicts the minimum Pd-activation time needed to impart sufficient catalytic activity to a Cu substrate so as to initiate electroless plating. Model predictions of the variation of the electroless mixed potential and critical activation time are compared with experimental data presented in Chapter 3. Reasonable agreement between model predictions and experiments is noted.

CHAPTER 2. Direct Electroless Deposition of Iron Boron on Copper

As was discussed in Chapter 1, electroless-deposited iron boron (FeB) is one possible alternative material for replacing nickel phosphorus (NiP). When Fe is alloyed with a suitable alloying element such as boron (B) at concentrations in excess of 18 at. %, the resulting alloy has an amorphous character.[30,37] During electroless deposition of FeB, the reducing agent present in the electroless bath, *i.e.*, sodium borohydride, provides the means for incorporation of B into the Fe deposit. The amorphous nature of the deposited FeB alloy leads to desired physical properties including superior wear resistance, corrosion resistance, and solderability.[29-34]

During electroless deposition, Fe^{2+} is reduced to metallic iron on the surface of the substrate via the reaction:

$$Fe^{2+} + 2e^{-} \rightarrow Fe^{0} \qquad [2.1]$$

In order for this reaction to proceed, electrons must be supplied by an oxidation reaction. This oxidation reaction involves the reducing agent borohydride (BH_4^-) and is shown below:

$$BH_4^- + 8OH^- \rightarrow BO_2^- + 6H_2O + 8e^- \quad [2.2]$$

Thus, the net reaction for electroless FeB deposition is shown in Eq. 2.3:

$$BH_4^- + 8OH^- + 4Fe^{2+} \rightarrow BO_2^- + 6H_2O + 4Fe^0 \quad [2.3]$$

This reaction (Eq. 2.3) must occur spontaneously for electroless FeB deposition to proceed. The electroless process is summarized in Figure 2.1, which also depicts the means for measuring the surface mixed potential during electroless deposition.

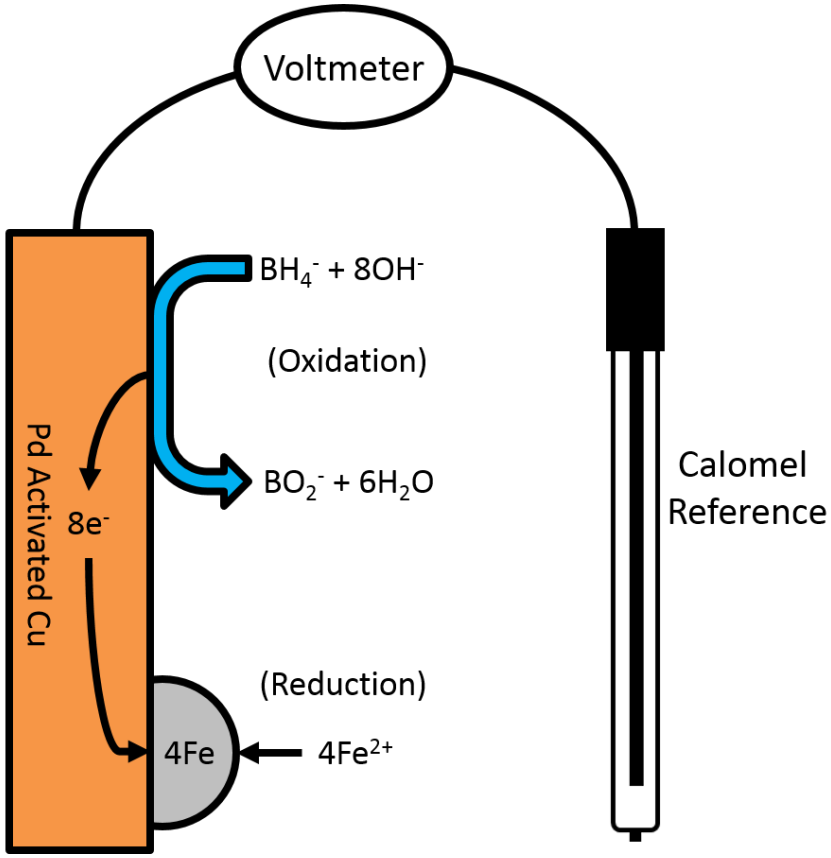

Figure 2.1: Schematic for of the electroless deposition of FeB on Cu. Borohydride (BH_4^-) is oxidized to form metaborate ions (BO_2^-), releasing electrons (e^-). These electrons are subsequently used to reduce Fe^{2+} to metallic iron (Fe^0) on the copper substrate. The potential at which these reactions occur is called the mixed potential (E_{mix}) and is measured with respect to a reference electrode in a two-electrode configuration.

The kinetics of the borohydride oxidation reaction (Eq. 2.2) are highly dependent on the electrode surface on which it occurs. In order for electroless deposition to proceed, the substrate must be catalytic towards this reaction. In previous studies of electroless Fe deposition, increased substrate catalytic activity needed for electroless FeB has been achieved via the use of palladium (Pd) activation. Pd surface activation is known to

catalytically activate the surface by accelerating the kinetics of the borohydride oxidation half reaction (Eq, 2.2).[40,41] Use of Pd-activation, however, adds an additional process step leading to an increase in overall cost and complexity of the electroless FeB process.

In this chapter, an electroless process for directly depositing FeB on Cu is described. Unlike previous studies, our electroless process eliminates the need for Pd-activation of the Cu substrate. Electrochemical polarization measurements of the oxidation and reduction half-reactions are used to optimize process parameters leading to activation-free FeB deposition. The physical properties of the FeB films deposited using our electroless process are characterized using various surface analysis and electrochemical techniques and these results are reported.

2.1 Experimental Procedure

2.1.1 Materials

Electroless deposition was performed from an aqueous electrolyte containing 0.05 M ferrous ammonium sulfate [$Fe(NH_4)_2(SO_4)_2{\cdot}6H_2O$, Pulver], sodium borohydride [$NaBH_4$, Acros] as reducing agent, and 0.13 M potassium sodium tartrate [$C_4H_{12}O_{10}KNa{\cdot}4H_2O$, Acros] as complexing agent. A range of sodium borohydride concentrations (0.02–0.30 M) was tested. Electrolyte pH was adjusted to pH 11 using sodium hydroxide [NaOH, Fisher], and 0.05 M boric acid [H_3BO_3, Acros] served as pH

buffer. Millipore spec (18.2 MΩ) deionized (DI) water was used to prepare all aqueous solutions. The DI water was purged with high purity argon for 1 hour before use.

High purity (99.98%) copper foil was used as the substrate for electroless plating. Prior to experimentation, the substrate copper foil was degreased with acetone, immersed in 2 M sulfuric acid (H_2SO_4) and rinsed with DI water. In cases where an iron substrate was required, iron was electroplated onto the Cu foil from an electrolyte containing 0.05 M ferrous ammonium sulfate, 0.13 M potassium sodium tartrate, 0.05 M boric acid at pH =11 and 41 ^oC. For electroplating Fe, the Cu foil was held at a potential of –1.05 V vs Standard Hydrogen Electrode (SHE) for 20 min, yielding an iron deposit of ~1 μm. After experiments, substrates were rinsed with DI water and dried in argon.

2.1.2 Methods

A three-electrode configuration placed in a jacketed electrochemical cell was used to measure polarization characteristics. The working electrode was either Cu foil or Cu foil pre-plated with Fe (using conditions described in section 2.1.1). The reference electrode was a saturated calomel electrode (SCE, Radiometer Analytical) and the counter electrode was a platinum wire electrode (Encompass). Hot water was circulated through the jacketed cell using a recirculating bath to ensure a constant temperature of 41 ^oC and the electrolyte was continuously purged with argon.

To measure polarization of the borohydride oxidation half-reaction, a 'Fe^{2+}-free' bath was used. This bath contained only the reducing agent (sodium borohydride), the complexing agent (sodium potassium tartrate) and the pH buffer (boric acid) with pH adjusted to 11 using sodium hydroxide. Polarization of the hydrogen evolution reaction was studied from a similar electrolyte except that this electrolyte did not contain the reducing agent (sodium borohydride).

To collect polarization of the two predominant reduction half-reactions, *i.e.* iron deposition and hydrogen evolution, a 'borohydride-free' half bath was used with an electrolyte containing all species except for the reducing agent (sodium borohydride). Thus, this electrolyte contained the iron salt (ferrous ammonium sulfate), the complexing agent (sodium potassium tartrate) and the pH buffer (boric acid) with pH adjusted to 11 using sodium hydroxide. All polarization scans were measured using a slow scan rate of 2 mV/s.

Mixed potential during electroless Fe deposition was also measured. The electrolyte for such measurements was the complete electroless bath described in the materials section (2.1.1). For mixed potential measurements, a two electrode set-up was employed. The copper foil served as the working electrode and SCE was used as the reference electrode.

Upon electroless deposition of FeB coatings, their corrosion resistance was evaluated. Corrosion resistance was measured in a 3.5 wt.% sodium chloride salt solution

(NaCl). The deposited material to be corrosion tested was immersed into the salt solution and polarization measurements were carried out at 2 mV/s over a 600 mV potential window centered around the corrosion potential of the FeB deposit.

All electrochemical testing, including corrosion resistance measurements were performed using a Versastat 4 potentiostat. Agitation was provided using a magnetic stir bar.

Deposit characterization was performed using Nova NanoLab 200 and Helios NanoLab 650 scanning electron microscopes (SEM). X-Ray photoelectron spectroscopy (VersaProbe XPS) was used to measure film composition. A Scintag X-ray diffractometer (XRD) was used to characterize film crystallinity.

2.2 Development of Activation-Free Electroless FeB Process

2.2.1 Limitations of Previously Reported Electroless FeB Process

Preliminary activation-free electroless plating experiments were conducted using a previously reported[30] FeB electroless solution containing 0.13 M ferrous ammonium sulfate, 0.14 M sodium potassium tartrate and 0.05 M potassium borohydride at pH=11 and at 41 ^{o}C. However, these attempts were largely unsuccessful because we found this electrolyte to be highly unstable, leading to large amounts of dark precipitate. The precipitate was determined via XPS to be iron oxide. To alleviate the problem of

precipitation, 0.05 M boric acid was added as a pH buffer. In addition, the concentrations of ferrous ammonium sulfate and sodium potassium tartrate were decreased to 0.05 M and 0.13 M, respectively. Finally, potassium borohydride was replaced with sodium borohydride at the same concentration. With these adjustments, the electrolyte stability was markedly improved. A Cu foil (without Pd-activation) was then placed in this electrolyte. No electroless FeB plating occurred. This was confirmed both visually and via weight gain measurements, both taken after 60 minutes of immersion of Cu in the electroless solution.

Mixed potential theory[55] was then used to characterize the previously reported electrolyte[30] and its inability to provide FeB deposition. Mixed potential theory postulates that when multiple redox reactions occur spontaneously on a surface, the net current via charge conservation must be zero under open circuit conditions, thereby allowing the oxidation and reduction reactions to be treated and analyzed separately. The potential at which the oxidation and reduction currents balance each other is called the mixed potential. Generally speaking, if the oxidation and reduction half reactions polarization curves are measured in their respective half baths (bath compositions described in section 2.1.2 as 'Fe^{2+}-free' and 'borohydride-free' half baths), then the potential at which these two polarization curves have equal magnitudes of current should correspond to the mixed potential measured during electroless deposition. However, in many electroless systems, the stipulation that half-reaction polarization characteristics can be used to accurately describe the electroless mixed potential and deposition rate does not hold true.[56-60] This is due to the fact that many electroless systems experience an autocatalytic effect whereby the oxidation and reduction half reactions are interdependent and catalyzed by one another.

Since the electroless FeB system discussed herein does closely obey the mixed potential theory (because mixed potential theory reliably predicts the surface potential and plating rate in the complete electroless solution as shown below), we can conduct polarization studies of the individual oxidation and reduction reactions.

Polarization measurements were used to investigate the half reactions in electroless FeB deposition using a bath reported in literature (bath compositions described in 2.2.2).[30] Results are shown in Figure 2.2. Since it is known that borohydride (BH) oxidation is affected by the catalytic activity of the substrate, measurements were conducted on both Fe and Cu foil substrates. The potential at which the magnitude of the oxidation current equals the magnitude of the net reduction current corresponds to the mixed potential for the system. For the electroless system where borohydride oxidation occurs on Cu this potential is -0.90 V vs. SHE and for the electroless system where borohydride oxidation occurs on Fe this potential is -0.50 V vs SHE. At pH 11, the Fe^{2+}/Fe^{0} reduction potential is close to -0.78 V vs SHE. Plating of iron is possible only at potentials more cathodic than this reduction potential. Thus, from a thermodynamics viewpoint, it is not possible for iron to spontaneously electroless-deposit onto itself because the mixed potential is positive with respect to the Fe reduction potential. During the early stages of electroless Fe deposition on the Cu substrate, the mixed potential begins at a more cathodic value (-0.90 V vs. SHE) because initially the borohydride oxidation is effectively catalyzed by the Cu substrate. This should facilitate Fe deposition; however, after iron begins to deposit and cover the electrode surface, borohydride oxidation is not effectively catalyzed. This causes the mixed potential to drift in the anodic (positive) direction, eventually reaching -0.50 V vs. SHE

where iron deposition is no longer possible. This behavior is consistent with the observation that, regardless of how long the Cu substrate is allowed to remain in the aforementioned electroless electrolyte, no Fe deposition is visually observed. Such a 'self-terminating' process is undesirable in practical applications that require thick (micron-scale) Fe coatings. This inability to deposit thick iron layers has been reported by a few other investigators as well.[30,37]

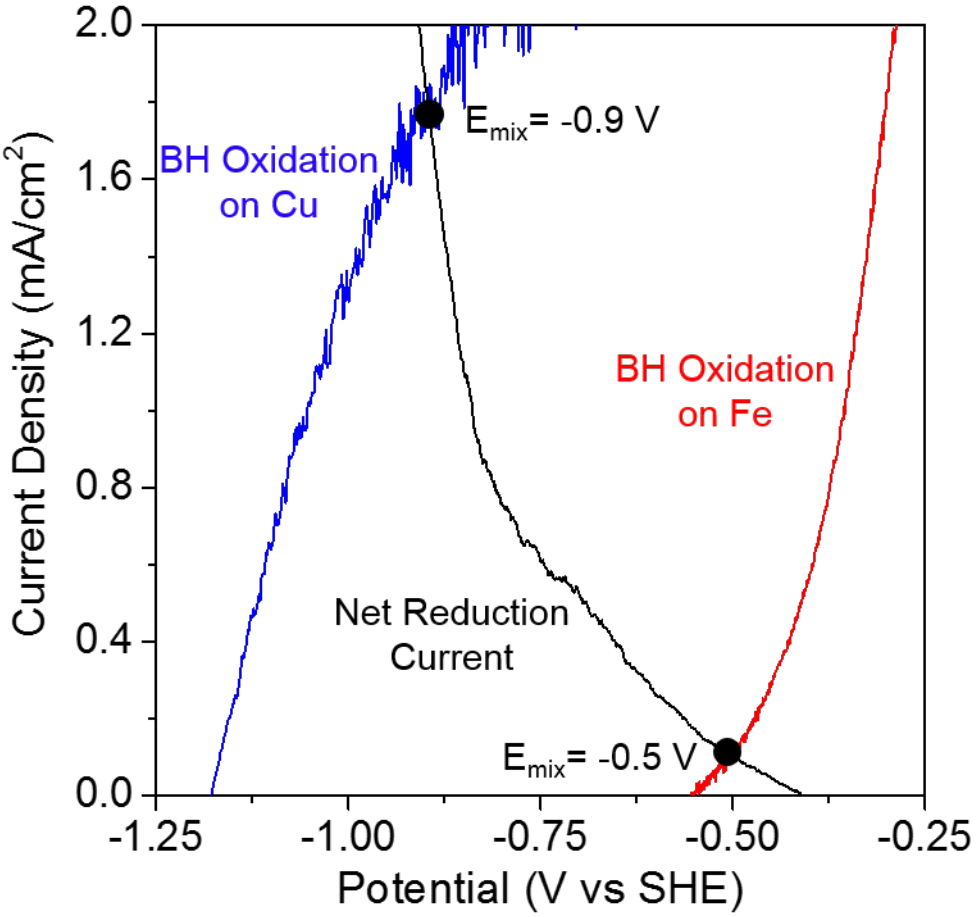

Figure 2.2: Polarization curves for borohydride (BH) oxidation on Cu (blue) and on Fe (red), as well as the polarization curve for the net reduction current (black). Borohydride (BH) oxidation was studied using a 'Fe^{2+}-free' bath containing low (0.05 M) borohydride content, and the net reduction current was studied using a 'borohydride-free' bath and consists of iron deposition and hydrogen evolution. Application of the mixed potential theory to the oxidation and reduction half-reactions indicates that electroless Fe nucleation on the Cu substrate is thermodynamically possible, but growth on the freshly nucleated iron layer is thermodynamically prohibited because the non-catalytic iron surface shifts the mixed potential into an anodic region where iron deposition does not occur.[61]

2.2.2 Development of Activation-Free Electroless FeB Deposition Process

From the polarization studies in Figure 2.2, it is clear that the mixed potential during electroless FeB deposition must be cathodically shifted in order to enable sustained deposition. It was thus postulated that by accelerating the borohydride oxidation rate it might be possible to shift the final mixed potential into a range where sustained electroless FeB deposition is feasible. One practical means of affecting the borohydride oxidation is through the concentration of sodium borohydride. A range of sodium borohydride concentrations were tested, keeping all other parameters of the electroless FeB electrolyte same as the electrolyte described in section 2.1.1. The steady-state electroless mixed potential for several sodium borohydride concentrations is shown in Figure 2.3. It is observed that the mixed potential shifted cathodically from –0.52 V vs SHE for 0.02 M borohydride concentration to –0.95 V vs SHE for 0.30 M borohydride concentration. This cathodic shift in mixed potential is desired as it leads to mixed potentials at which iron deposition is thermodynamically possible. Furthermore, a higher borohydride concentration (0.30 M) did not de-stabilize the bath. A mixed potential of –0.95 V vs SHE (at 0.30 M borohydride concentration) is very close to the potential reported for systems utilizing a sacrificial aluminum anode, thereby offering promise for a ‘activation-free’ electroless FeB process at this higher borohydride concentration.

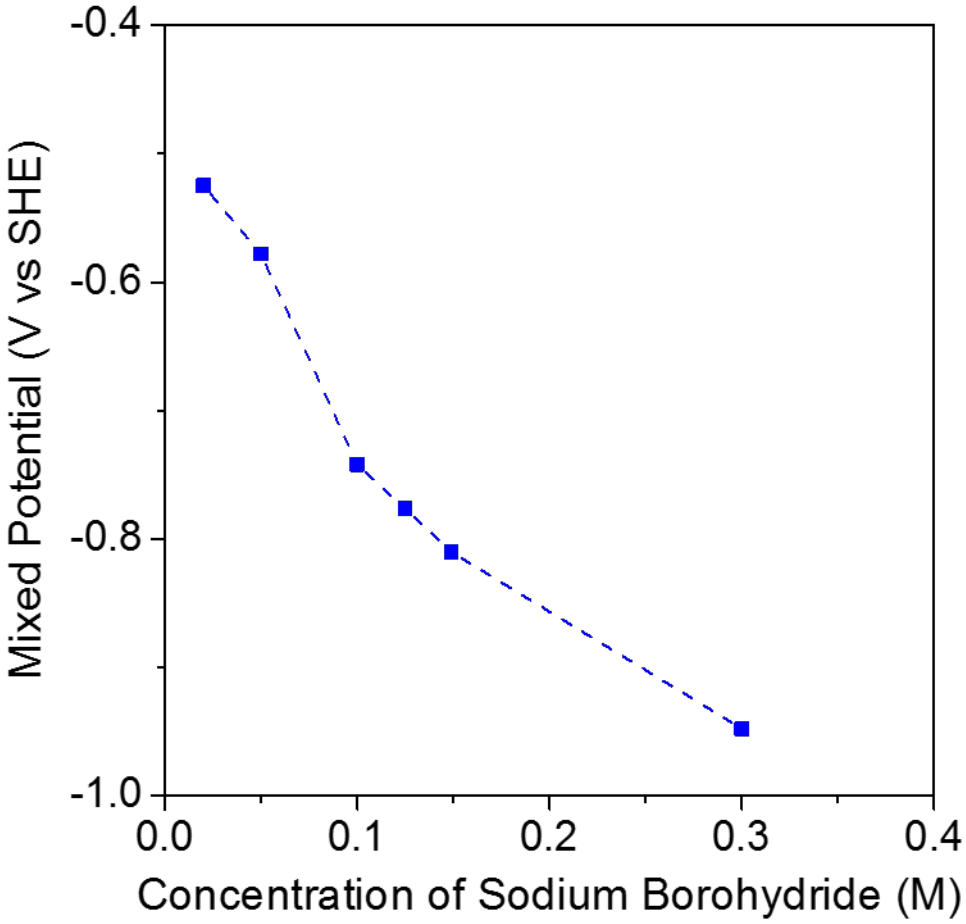

Figure 2.3: Effect of varying borohydride concentration on the mixed potential during electroless FeB plating. Increasing borohydride concentration shifts the mixed potential cathodically as desired.[61]

Electrochemical polarization studies of the anodic and cathodic half-reactions were performed for the bath containing the higher borohydride concentration (0.30 M). As shown in Figure 2.4, the higher borohydride concentration produced a substantial cathodic shift in the polarization behavior of the borohydride oxidation reaction on an Fe-coated Cu foil substrate, *i.e.*, E_{red} = -0.91 V vs SHE as compared to E_{red} = -0.5 V vs SHE for the low (0.05 M) borohydride concentration bath adapted from literature reports (Figure 2.2).[5]

There is also a slight cathodic shift of E_{red} for borohydride oxidation on Cu at this higher (0.30 M) borohydride concentration, leading to a new E_0 = -1.17 V vs SHE. Upon application of the mixed potential theory to the polarization curves of Figure 2.4, the mixed potential during growth when borohydride oxidation occurs on Fe is E_{mix} = -0.90 V vs SHE. This mixed potential is now cathodic of the Fe^{2+}/Fe^0 reduction potential at ~ -0.78 V vs SHE. This implies that sustained electroless Fe plating is achievable from a high concentration borohydride bath. In addition, this calculated mixed potential (i.e., by applying mixed potential theory) matches well with the actual mixed potential measured during electroless plating, providing evidence that the mixed potential theory as described in the previous section applies to the electroless FeB system. As shown below (also in Figure 2.5), electroless FeB deposition from a stable bath containing 0.30 M borohydride concentration indeed yields thick FeB films, consistent with predictions of the polarization study discussed in this section.

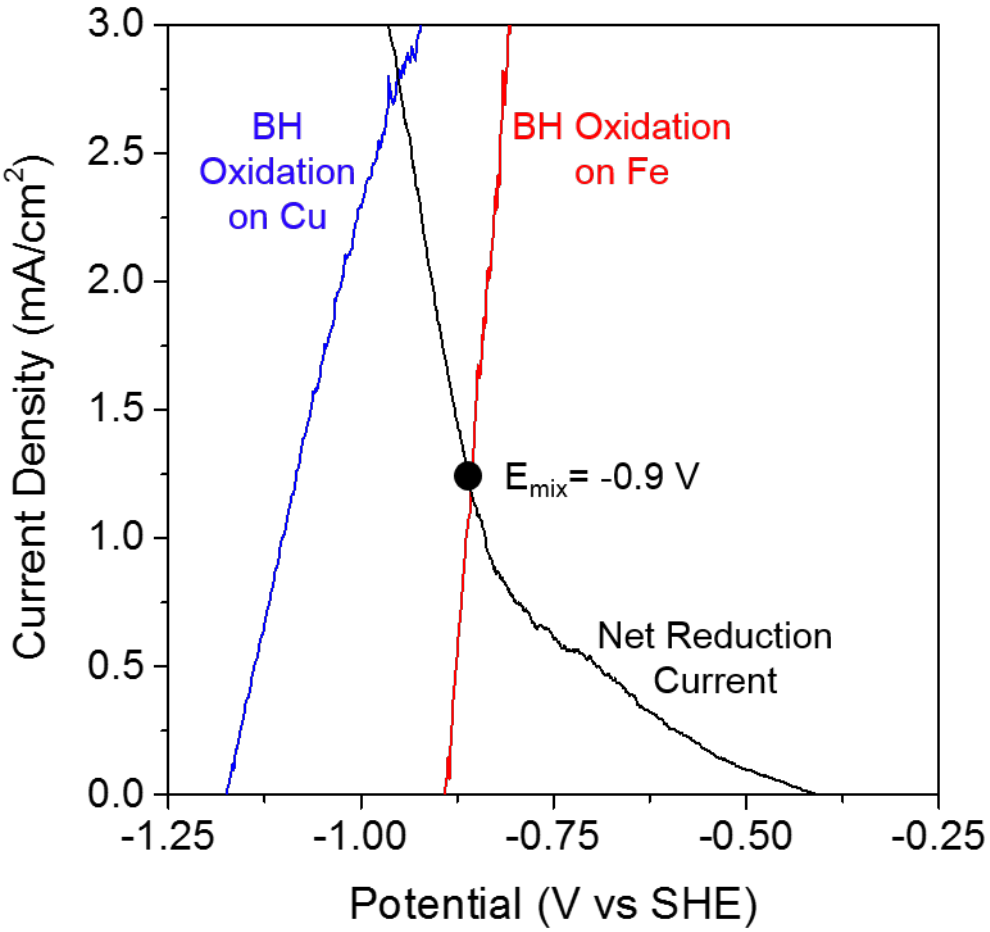

Figure 2.4: Polarization curves for borohydride (BH) oxidation on Cu (blue) and on Fe (red), as well as the polarization curve for the net reduction current (black). Borohydride (BH) oxidation was studied using a 'Fe^{2+}-free' bath containing high (0.30 M) borohydride content, and the net reduction current was studied using a 'borohydride-free' bath and consists of iron deposition and hydrogen evolution. Application of the mixed potential theory to the oxidation and reduction half-reactions indicates that electroless Fe deposition can now be sustained as the borohydride begins to oxidize on freshly plated iron. This is due to the cathodic shift of the mixed potential compared to the previous low (0.05 M) borohydride concentration electrolyte. This puts the mixed potential on iron in a region where iron deposition is thermodynamically permitted.[61]

2.3 Materials Characterization of Electroless FeB Films

As discussed in Chapter 1, for applications in printed circuit boards, electroless FeB films must meet several requirements, including high deposition rate, boron incorporation leading to amorphous structure and suitable corrosion resistance. In this section, the films fabricated using the high borohydride (0.30 M) concentration bath developed in section 2.2.2 are evaluated to ensure that they meet these requirements.

To determine the electroless plating rate, FeB films were deposited on a silicon (Si) wafer pre-coated with silicon dioxide (SiO_2), a sputter-deposited tantalum nitride (TaN) barrier layer, and a 70 nm sputter-deposited Cu seed layer (Figure 2.5). Such a stack enables preparation of clean focused ion beam (FIB) cross-sections, which can then be imaged using SEM. A FeB film thickness of ~120 nm was measured after 30 min of electroless plating, corresponding to an average deposit growth rate of ~0.24 μm/hr. The 'blister' in the FIB cross-section is evidence of parasitic hydrogen evolution which is also evidenced by the observation of gas bubbles during deposition. Similar 'blisters' in films have been reported in previous studies.[62]

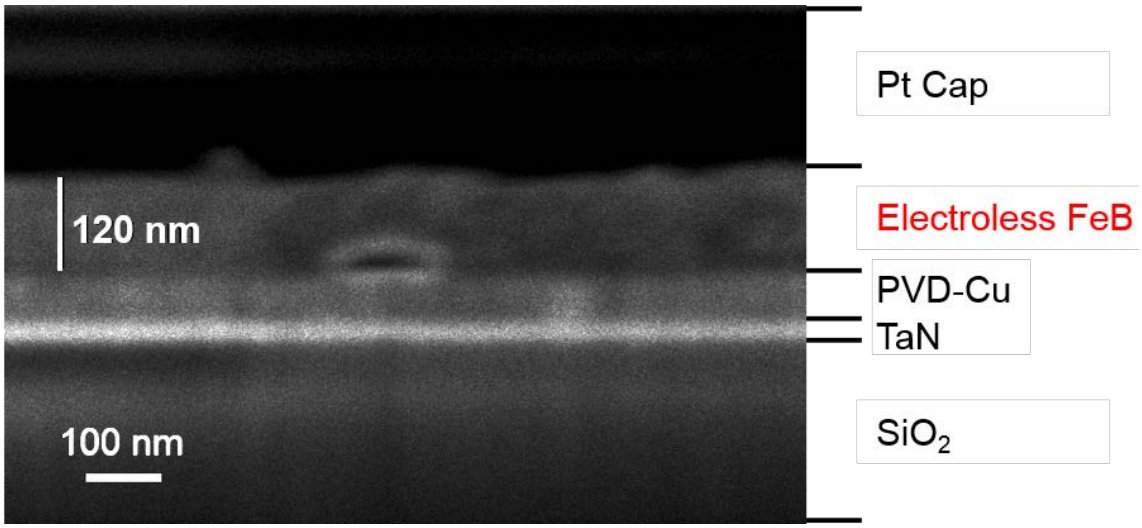

Figure 2.5: FIB cross-section of an electroless FeB film plated over a PVD-Cu substrate, imaged using SEM. Electroless plating time is 30 min leading to an average plating rate of 0.24 μm/hr. The electroless bath contained 0.30 M sodium borohydride, 0.05 M ferrous ammonium sulfate, 0.13 M potassium sodium tartrate and 0.05 M boric acid. Bath pH was 11 and bath temperature was 41 ^{o}C.[61]

The presence of Fe and B in the electroless films was confirmed via XPS (Figure 2.6). The average composition was B = 30.8 at. % and Fe = 69.2 at. % in the bulk deposit. As evidenced by XPS, the FeB film surface showed moderate quantities of oxygen most likely due to surface oxidation upon air exposure. XRD of the FeB films confirms that the electroless FeB films had an amorphous character (Figure 2.7). The presence of small peaks due to iron oxide[63] and boron oxide[64] (inset in Figure 2.7) is attributed to surface oxidation upon air exposure. The XRD peaks detected at 2θ = 43.6, 50.7 and 74.3 are attributed to the polycrystalline Cu substrate used to grow the electroless FeB films.[65]

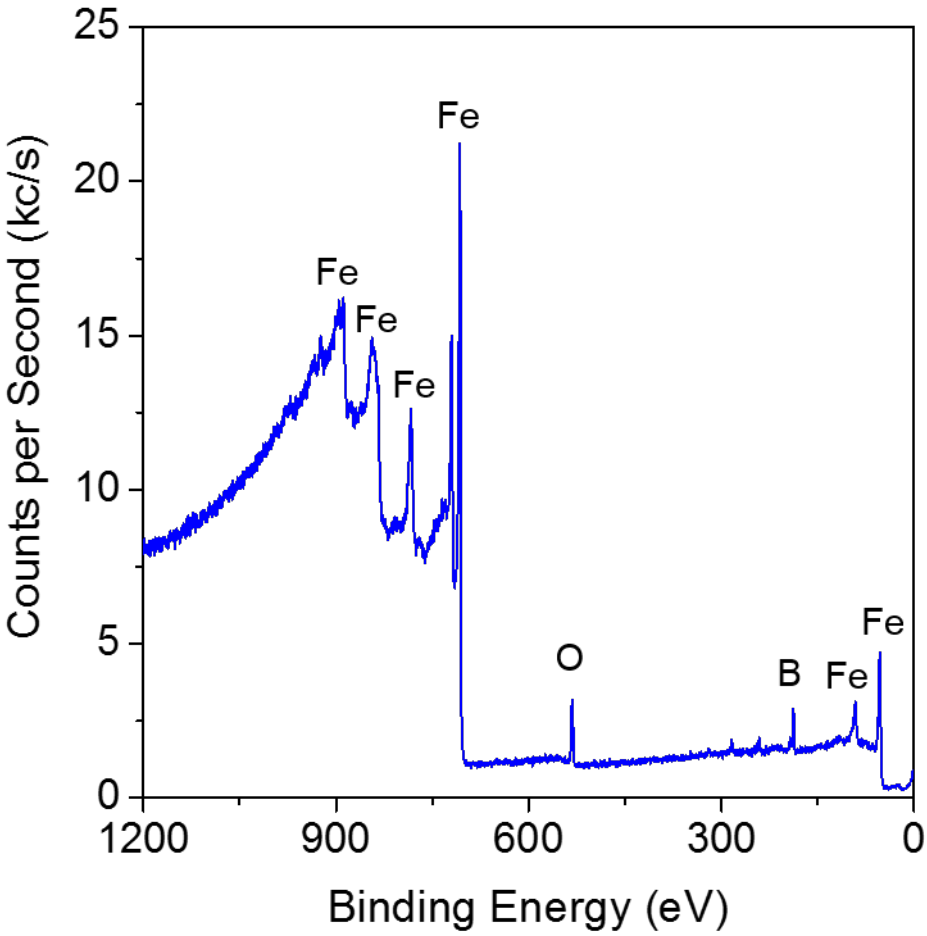

Figure 2.6: XPS of electroless FeB films obtained from the same bath as in Figure 2.5, *i.e.*, using a high (0.30 M) concentration of borohydride. XPS confirms Fe (at 69.2 at. %) and B (at 30.8 at. %). The oxygen peak is likely due to surface oxidation upon air exposure.[61]

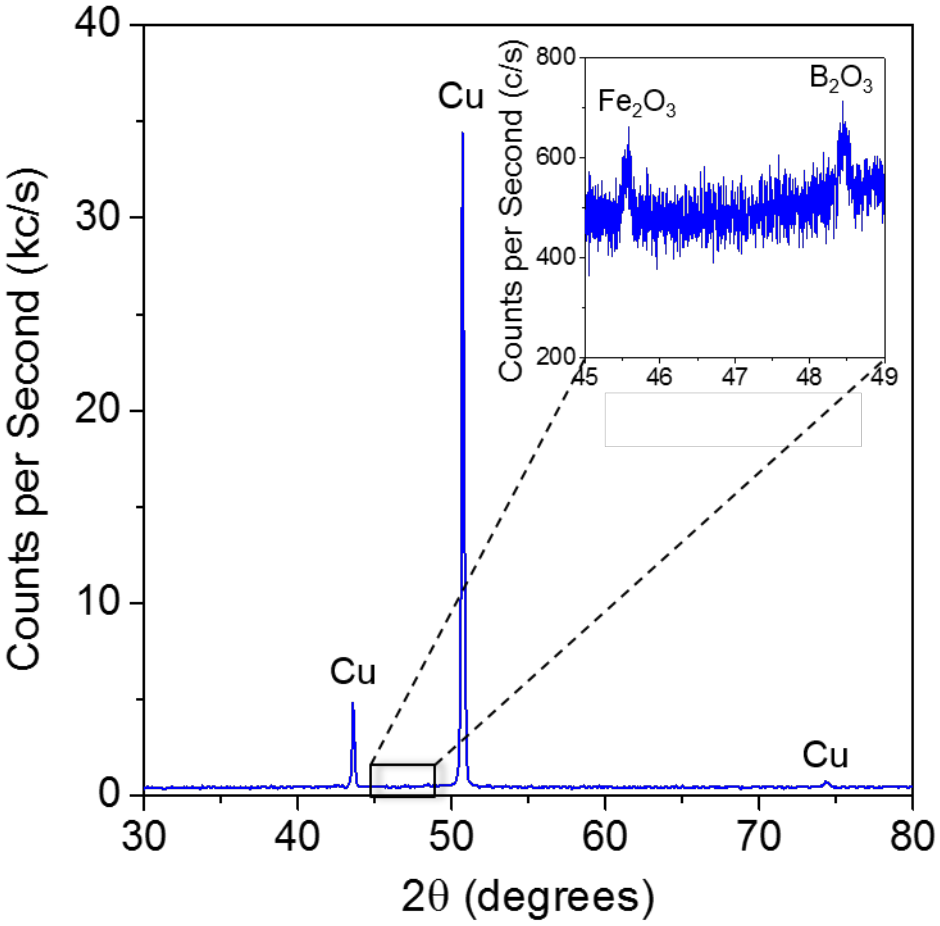

Figure 2.7: XRD of electroless FeB films obtained from the same bath as in Figure 2.5, *i.e.*, using a high (0.30 M) concentration of borohydride. The lack of an iron peak is indicative of amorphous structure. The strong XRD peaks detected at 2θ = 43.6, 50.7 and 74.3 are attributed to the polycrystalline Cu substrate used to grow the electroless FeB films. The weak XRD peaks detected at 2θ = 45.6 and 48.4 (inset) are attributed to iron and boron surface oxides, respectively.[61]

Corrosion properties of electroless FeB films were tested and compared to conventional NiP films. The NiP films were prepared using a procedure described by Agarwala *et al.*[66,67]. Corrosion tests were conducted in a 3.5 wt.% sodium chloride (NaCl) salt solution. Polarization measurements were conducted at a scan rate of 2 mV/s over a 600 mV window (Figure 2.8). Polarization curves indicate a corrosion potential of –0.56

V vs SHE for FeB, which is cathodic to the corrosion potential of –0.18 V vs SHE for NiP. Consistent with the corrosion potential shift, a corrosion current density of 31.1 $\mu A/cm^2$ (for FeB) was measured, which is about an order of magnitude larger than that observed for NiP (3.6 $\mu A/cm^2$). The higher corrosion current density is attributed to the intrinsically higher activity of Fe compared to Ni. Nonetheless, the corrosion current density of FeB is still within acceptable range for application as a solderable finish in electronics and is more than an order of magnitude less than typical corrosion current density of pure iron (~600 $\mu A/cm^2$).[68]

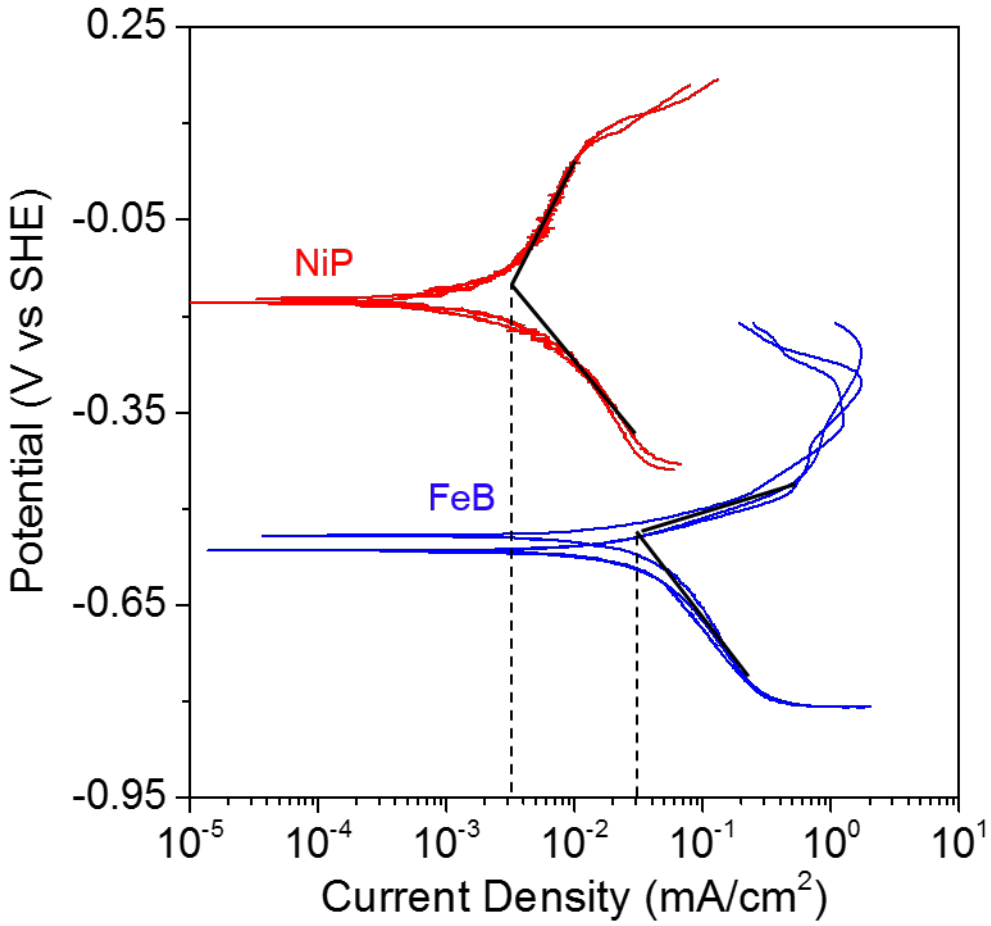

Figure 2.8: Electrochemical corrosion tests comparing electroless FeB films produced from the same bath as in Figure 2.5, *i.e.*, using a high (0.30 M) concentration of borohydride. Polarization tests were conducted in a 3.5 wt.% NaCl solution. Tests indicate a corrosion current density of 31.1 μA/cm^2 for FeB compared to 3.6 μA/cm^2 for NiP. As comparison, the corrosion current density of pure Fe metal is typically ~600 μA/cm^2 and thus FeB has acceptably high corrosion resistance.[61]

2.4 Conclusions

An electroless process for ‘direct’, activation-free plating of FeB on Cu substrates is developed. This process, unlike prior attempts, does not require a sacrificial aluminum anode or palladium activation pretreatment. Electrochemical polarization studies and mixed potential analysis provide valuable optimization tools enabling a ‘direct’ electroless FeB plating process on Cu substrates. Resulting FeB films exhibit the desired composition, amorphous structure and adequate corrosion resistance making them attractive as potential Ni-free coatings for application as solderable finish in PCBs.

CHAPTER 3. Role of Palladium Activation in Electroless Deposition of Iron Phosphorus Coatings

In Chapter 2, a process for achieving electroless deposition of iron boron films directly on copper without the use of any activation step was described.[61] This greatly reduces the complexity and the number of process steps required in applying the coatings via electroless deposition. However, due to the potential toxicity of boron and boron-containing compounds, boron is another element that is under scrutiny and regulation by the European Union.[63] Thus, a hypophosphite-based method of electroless deposition of iron that provides amorphous FeP alloys is of great interest to the electronics and surface finishing industries.

Iron phosphorus (FeP) plating on a copper substrate was first demonstrated by Ruscior and Croiala using an aluminum sacrificial anode in electrical contact with the substrate.[36] The sacrificial anode provided the reducing conditions necessary for enabling the deposition of iron on the substrate surface.[36-39] Use of a sacrificial anode is not ideal

for many practical applications because of the difficulty to establish an electrical contact with all surfaces that need to be plated. Such is the case for plating onto micro-patterned, electrically isolated features present on a printed circuit board. Furthermore, the use of a sacrificial anode is not practical when plating onto an insulator substrate.

In this chapter, a process for electroless iron phosphorus deposition without the use of a sacrificial anode is described. To achieve this, the substrate must be catalytically activated. Catalytic activity of the substrate is achieved through palladium (Pd) activation. Pd-activation refers to the deposition of palladium onto the substrate via a spontaneous, surface-limited redox reaction. When a substrate (*e.g.*, copper – Cu) is immersed in a $PdCl_2$ solution, the surface of the less noble Cu is oxidized and Cu dissolves into solution via the reaction:

$$Cu^0 \rightarrow Cu^{2+} + 2e^- \qquad [3.1]$$

The electrons from this reaction are then spontaneously consumed to reduce Pd^{2+} ions present in the solution to Pd^0 particles on the substrate surface via the reaction:

$$Pd^{2+} + 2e^- \rightarrow Pd^0 \qquad [3.2]$$

This redox chemistry occurs spontaneously upon placement of the Cu substrate in the $PdCl_2$ electrolyte and the net reaction for the entire Pd-activation process is shown in Eq. 3.3:

$$Pd^{2+} + Cu^{0} \rightarrow Pd^{0} + Cu^{2+} \quad [3.3]$$

After Pd-activation of the substrate, Fe is deposited via electroless plating. The cathodic half-reaction during electroless plating is shown:

$$Fe^{2+} + 2e^{-} \rightarrow Fe^{0} \quad [3.4]$$

This reduction reaction requires electrons which are provided by the oxidation of a reducing agent. The reducing agent for FeP deposition is the hypophosphite anion ($H_2PO_2^-$) and its oxidation reaction is shown:

$$H_2PO_2^{-} + 3OH^{-} \rightarrow HPO_3^{2-} + 2H_2O + 2e^{-} \quad [3.5]$$

The net reaction for electroless FeP deposition is shown in Eq. 3.6:

$$Fe^{2+} + H_2PO_2^{-} + 3OH^{-} \rightarrow Fe^{0} + HPO_3^{2-} + 2H_2O \quad [3.6]$$

In addition to providing electrons for the reduction of Fe^{2+} ions, the electrons released via oxidation are also consumed in parasitic reduction reactions such as the oxygen reduction reaction (ORR) and the hydrogen evolution reaction (HER). The hydrogen evolution, being the predominant parasitic reaction, occurs as shown Eq. 3.7:

$$2H_2O + 2e^{-} \rightarrow H_2 + 2OH^{-} \quad [3.7]$$

The operating conditions during Pd-activation, *i.e.*, the activation time, and the composition of the activation electrolyte, determine the Pd coverage of the substrate after activation. The Pd coverage plays an important role in determining if spontaneous iron deposition is facilitated in the subsequent electroless step or not. This role is investigated in further detail herein.

3.1 Experimental Procedure

3.1.1 Materials and Electrolyte Composition

Electroless deposition was performed from an electrolyte containing 0.05 M ferrous ammonium sulfate [$Fe(NH_4)_2(SO_4)_2 \cdot 6H_2O$, Fisher], 1.0 M sodium hypophosphite [$NaH_2PO_2 \cdot H_2O$, Sigma Aldrich] as reducing agent, and 0.13 M potassium sodium tartrate [$C_4H_{12}O_{10}KNa \cdot 4H_2O$, Acros] as complexing agent. Electrolyte pH was adjusted using 2.0 M sodium hydroxide [NaOH, Fisher]. Millipore spec (18.2 MΩ) deionized (DI) water was used to prepare all electrolytes. This electrolyte was developed through empirical trials, changing species concentrations until sufficiently cathodic mixed potential, necessary to deposit iron, were achieved.

Electroless deposition was performed on copper or platinum rotating disk electrodes (Pine). When a platinum electrode was used, it was pre-plated at 1 mA/cm^2 for

150 s in an acidified (pH = 2) electrolyte containing 0.1 M copper sulfate and 500 ppm PEG-4000 additive. The pre-plated Cu thickness was ~0.1 µm. All substrates were polished with alumina micro-slurry and degreased with acetone for five seconds before use. The copper substrates were then activated in a 2.8 mM palladium chloride ($PdCl_2$) solution for varying activation times. During Pd-activation, the nobler Pd replaces the Cu on the substrate surface through a spontaneous displacement reaction, as shown in Eq. 3.3. Pd-activation was followed by a DI water rinse before electroless FeP deposition.

X-ray photoelectron spectroscopy (VersaProbe XPS) was used to measure the film composition. All electrochemical measurements were performed using a Versastat 4-FRA model potentiostat.

3.1.2 Mixed Potential Measurements During Electroless FeP Deposition

A jacketed electrochemical cell with a two-electrode configuration was used for measurements of the mixed potential during electroless FeP plating. The working electrode was a copper rotating disk electrode (RDE) prepared as described above in section 3.1.1. This working electrode was then activated in the 2.8 mM $PdCl_2$ electrolyte for varying amounts of time (0 – 3600 s) in order to achieve various degrees of substrate Pd coverage. The RDE working electrode was rotated at 2000 RPM. The reference electrode was a saturated calomel electrode (SCE, Fisher). The electroless bath was maintained at 75 °C by passing hot water through a recirculating water jacket around the cell. The open circuit

potential, *i.e.*, the electroless mixed potential, was recorded. All electrode potentials below are referenced with respect to the standard hydrogen electrode (SHE).

3.1.3 Polarization Measurements of Hypophosphite Oxidation

A jacketed electrochemical cell with a three-electrode configuration was used for polarization measurements of the hypophosphite oxidation half-reaction during electroless FeP plating. The working electrode was a copper rotating disk electrode (RDE) prepared as described above in section 3.1.1. This working electrode was then activated in the 2.8 mM $PdCl_2$ electrolyte for varying amounts of time (0 – 3600 s) in order to achieve various degrees of substrate Pd coverage. The RDE working electrode was rotated at 2000 RPM. The counter electrode was a platinum wire (Encompass) and the reference electrode was a saturated calomel electrode (SCE, Fisher). Oxidation of hypophosphite was studied in the complete electroless solution, but in an electrode potential range (-0.90 to -0.81 V vs SHE) where other reactions (hydrogen evolution and iron deposition) were minimal. The electroless bath was maintained at 75 °C by passing hot water through a recirculating water jacket around the cell. Scan rate during electrochemical polarization was 10 mV/s.

3.1.4 Polarization Measurements of the Hydrogen Evolution Reaction

Hydrogen evolution polarization measurements were collected similar to hypophosphite oxidation measurements. However, in this case, the electrolyte contained

only the tartrate complexant and sodium hydroxide, *i.e.*, the electrolyte did not contain dissolved iron or sodium hypophosphite reductant. Collecting polarization data in a partial electrolyte is acceptable for hydrogen evolution because it is the only reaction in the electroless iron system that, as far as we know, is not interdependent on other reactions occurring on the electrode surface. Thus, the HER polarization measured in the partial electrolyte should represent that in the complete electroless system. The working electrode was a copper rotating disk electrode (RDE) prepared as described above in section 3.1.1. This working electrode was then activated in the 2.8 mM $PdCl_2$ electrolyte for varying amounts of time (0 – 3600 s) in order to achieve various substrate Pd coverages that represented the 'initial' state of the substrate before electroless FeP plating could commence. All other conditions were kept the same as those used for hypophosphite oxidation polarization measurements described in section 3.1.3.

3.1.5 Polarization Measurements of Iron Deposition

To collect polarization data on the iron plating reaction, iron was first plated potentiostatically on a platinum RDE for 1 hour from the electroless FeP electrolyte described is section 3.1.1. After deposition, the electrode was immersed in acidified DI water (0.6 M H_2SO_4, pH = 0.2). While some iron was oxidized due to air exposure during sample transfer, the polarization measurement was not affected as discussed below. In the acidic electrolyte, the iron layer was oxidized potentiostatically at an applied potential of 0.45 V vs SHE to Fe^{2+}. In addition, any iron (II) oxide formed during air exposure spontaneously dissolved as Fe^{2+} ions. The acid electrolyte was purged continuously with

argon gas to eliminate any dissolved oxygen that could spontaneously oxidize the Fe^{2+} to Fe^{3+} in solution. The dissolved iron (Fe^{2+}) was then oxidized to Fe^{3+} potentiostatically at 1.15 V vs SHE and the mass-transport limited oxidation current was measured. The entire process is summarized below in Figure 3.1. This process was repeated for iron deposits formed at various applied potentials.

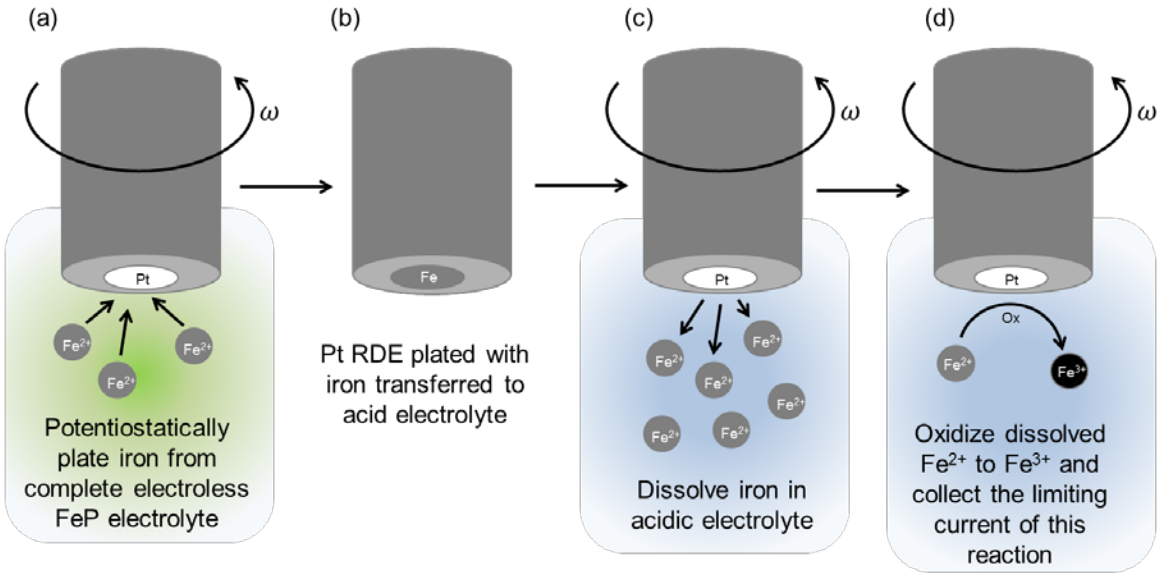

Figure 3.1: Schematic of the process used to obtain iron deposition polarization in the complete electroless FeP system. First, iron was deposited potentiostatically on a platinum RDE from a complete electroless FeP electrolyte (a). The RDE with deposited iron was then removed from the complete electroless FeP electrolyte and placed in an acid electrolyte (b) where all of the plated iron was dissolved into Fe^{2+} potentiostatically (c). The Fe^{2+} was then further oxidized to Fe^{3+} and the limiting current of this reaction was measured to determine the initial amount of iron plated (d).

In step (d) of Figure 3.1, the limiting current was related to the bulk Fe^{2+} concentration via the Levich equation:

$$I_L = 0.62nFAD^{2/3}\omega^{1/2}v^{-1/6}C_b \quad [3.8]$$

In Eq. 3.8, I_L is the limiting current of Fe^{2+} oxidation, n is the number of electrons, F is Faraday constant, A is the area of the electrode, D is the diffusion coefficient, ω is the angular rotation rate, v is the kinematic viscosity, and C_b is the bulk concentration of Fe^{2+}. Since step (d) in Fig. 3.1 provides a measured value of I_L, and all other parameters are known, the bulk Fe^{2+} concentration C_b can be determined.

Knowing the volume of the acid electrolyte and the concentration of the iron C_b dissolved in it, it was possible to determine the mass of iron (m) dissolved in the acid electrolyte. The mass of iron dissolved in the acid electrolyte is equal to the amount of iron deposited in the initial plating step and thus could be related to the plating current of iron in the deposition step via Faraday's law of electrolysis, as shown in Eq. 3.9:

$$m = \frac{Mt}{nF} I \quad [3.9]$$

In Eq. 3.9, m is the mass of iron, M is the molar mass of iron, t is the iron deposition time, n is the number of electrons, F is the Faraday constant and I is the iron deposition current.

This electrochemical method provided the iron deposition rate (current) as a function of the electrode potential during iron deposition step (a), *i.e.*, the iron plating

polarization behavior. A confirmation of the validity and accuracy of this newly developed method is found in section 3.3.2.

3.2 Critical Role of Pd-Activation in Enabling FeP Deposition

When deposition of electroless FeP was attempted on a Pd-activated surface, a variety of Pd-activation times were tested, ranging from 0 s to 3600 s. These Pd-activated substrates were then placed in the FeP electroless bath and the electroless mixed potential was measured. The results of these measurements are shown in Figure 3.2a. As the Pd-activation time increased, the mixed potential during electroless deposition became increasingly negative, *i.e.*, cathodic. This is an important observation because, at low activation times (*i.e.*, below 100 s), the mixed potential measured is anodic in comparison to the reduction potential of iron according to the Pourbaix diagram depicted in Figure 3.2b. From Figure 3.2a and 3.2b, it is clear that low activation times (~100 s) do not result in iron deposition, while high activation times (>1000 s) enable iron deposition.

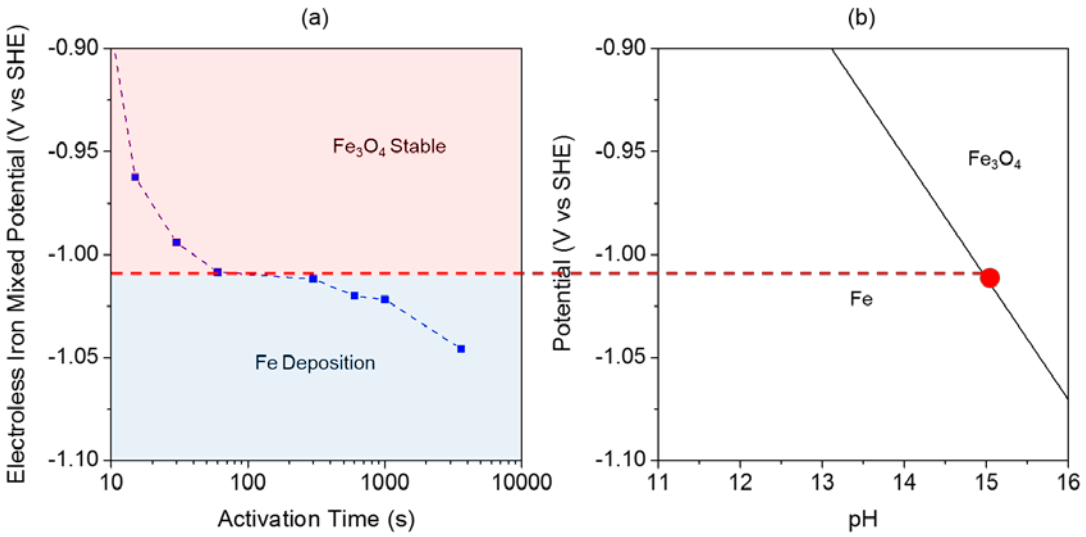

Figure 3.2: (a) Mixed potential of a Pd-activated substrate in an electroless FeP electrolyte as a function to the substrate Pd-activation time. As activation time increases, the mixed potential shifts in the negative (cathodic) direction. The Pourbaix diagram for iron (b) indicates that at mixed potentials anodic to -1.01 V vs SHE (at pH~15, *red dot*), metallic iron deposition is thermodynamically not possible [*red region* of (a)]. With sufficient activation time, the mixed potential shifts cathodic enough [*blue region* of (a)] to be in the region where metallic iron deposition is favored. RDE rotation speed = 2000 RPM.

The observations made from Figure 3.2 were supported by deposit analyses using XPS. Figure 3.3 shows XPS analysis of a Fe-containing film electroless-deposited after a short (60 s) Pd-activation step. This sample resulted in an anodic mixed potential of 0.99 V vs SHE and was found to contain a very thin (~20 nm, Fig. 3.3) iron oxide film with large portions of exposed substrate (Cu). For such low activation times, no evidence of metallic Fe was present in the XPS analysis. In contrast, Figure 3.4 shows XPS analysis of an Fe-containing film electroless-deposited after prolonged (1000 s) Pd-activation of the substrate. This sample resulted in a cathodic mixed potential (-1.05 V vs. SHE) and showed metallic iron in the bulk deposit. Only the near surface region was oxidized perhaps during air exposure. From these results, it is apparent that the length of the Pd-activation step is a

critical variable in controlling the catalytic activity of the substrate, which in turn determines whether spontaneous electroless iron deposition proceeds or not. To understand and more importantly quantify the mechanism underlying this observation, it is essential to examine the process through which the Pd-activation influences the electroless half-reactions and thereby the electroless mixed potential during early stages of electroless deposition.

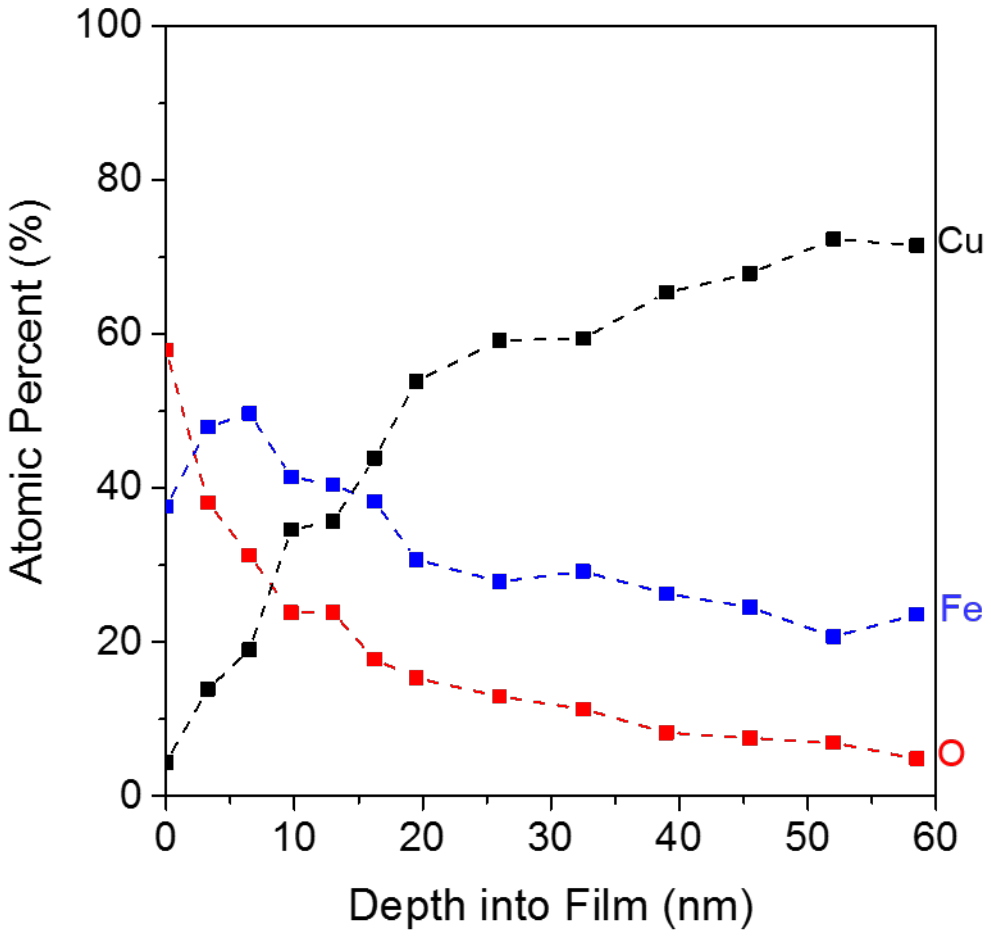

Figure 3.3: XPS depth profiling of an electroless FeP film (mixed potential = -0.95 V vs SHE) deposited after activating the substrate with Pd for a short activation time (60 s). XPS analysis shows that the film is a surface iron oxide layer with a thickness in the range of about 20 nm. The lack of any metallic iron plating is consistent with the analysis presented in Figure 3.2b. Electrode area = 0.196 cm^2; RDE rotation speed = 2000 RPM. Electroless bath composition is provided in section 3.1.1.

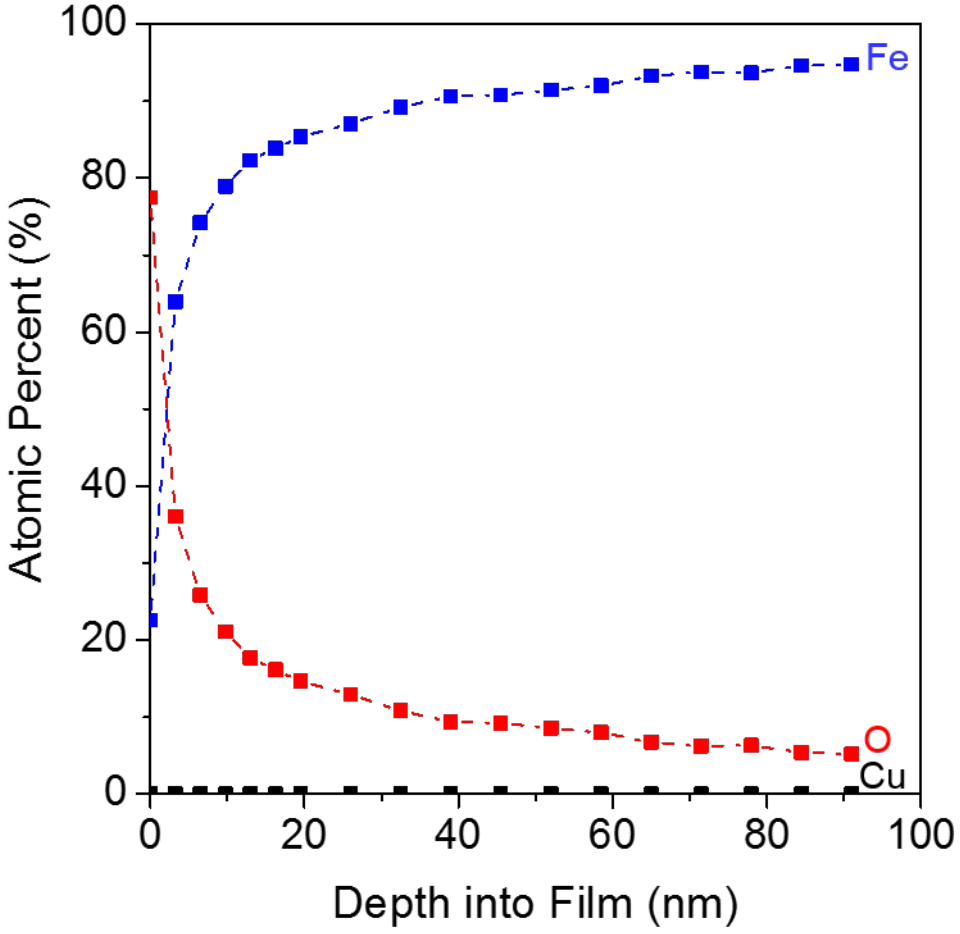

Figure 3.4: XPS depth profiling of an electroless FeP film (mixed potential = -1.05 V vs SHE) deposited after activating the Cu substrate with Pd for 1000 s. XPS analysis shows that, while there is a surface oxide present due to air exposure, the bulk of the film is metallic iron. This result is consistent with the analysis using the Pourbaix diagram presented in Figure 3.2b. Electrode area = 0.196 cm^2; RDE rotation speed = 2000 RPM. Electroless bath composition is provided in section 3.1.1.

3.3 Polarization Studies to Characterize the Effect of Substrate Pd-Activation on the Electroless FeP Mixed Potential

3.3.1 Hypophosphite Oxidation on Pd-Activated Cu Substrates

It is hypothesized that hypophosphite oxidation is poorly catalyzed by copper, but strongly catalyzed by Pd after substrate is activated. As the substrate is activated with Pd, the surface coverage of Pd increases gradually with the Pd-activation time. At low activation times, the Pd coverage is not large enough to catalyze sufficiently the hypophosphite oxidation reaction. As this Pd coverage increases, the hypophosphite oxidation current also increases because of increased availability of catalytic sites on the substrate surface. The dependence of hypophosphite oxidation current on Pd-activation time is confirmed via electrochemical polarization shown in Figure 3.5. It is observed that the catalytic activity of the substrate towards hypophosphite oxidation increases with Pd-activation time because of enhanced coverage of the Cu substrate with catalytic Pd.

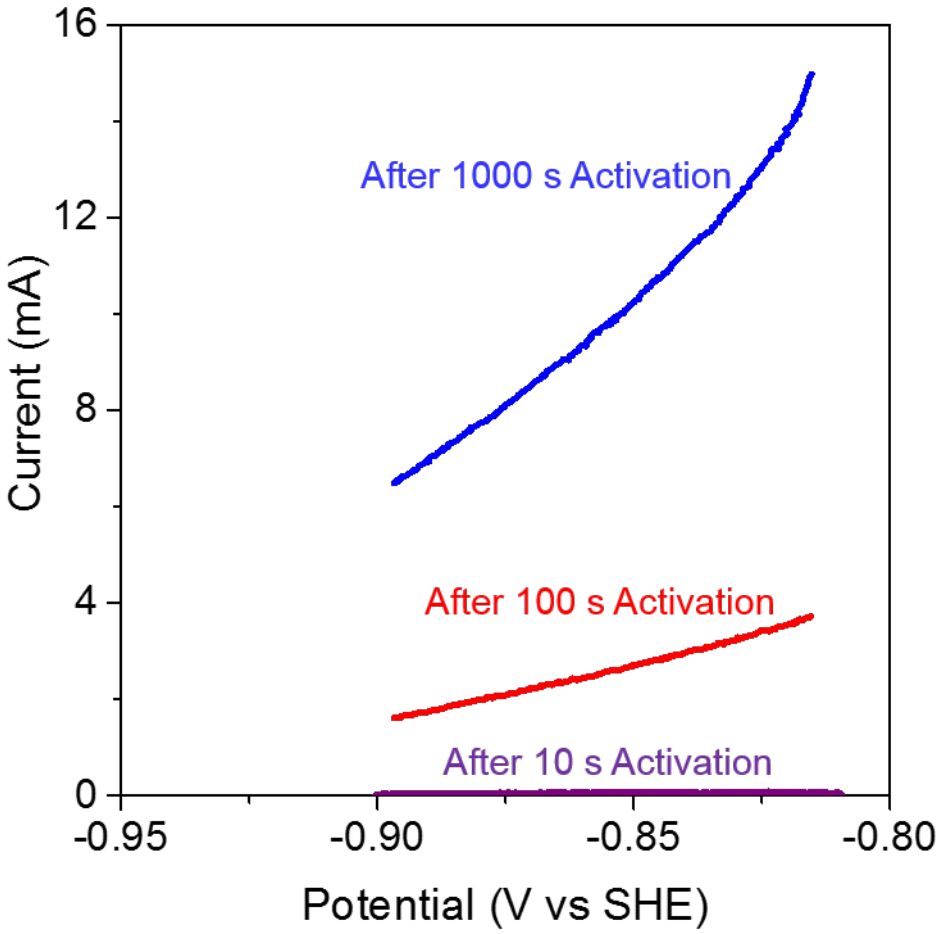

Figure 3.5: Hypophosphite oxidation polarization on a Cu substrate after activating it with Pd for various activation times. As Pd-activation time increases, the coverage of Pd on the substrate increases. This increase in Pd coverage leads to a higher hypophosphite oxidation current. Electrode area = 0.196 cm^2; RDE rotation speed = 2000 RPM. Electrolyte composition is discussed in section 3.1.1.

3.3.2 Polarization Behavior of the Iron Deposition Half-Reaction

Iron deposition occurs in the potential range where both hypophosphite oxidation and hydrogen evolution currents are not negligible. Thus, iron deposition polarization

cannot be obtained using measurements of the current in the complete electroless bath similar to measurements of the hypophosphite oxidation (Figure 3.5). Often mass measurements are used to determine the amount of deposited material, but for electroless FeP the plating rate is too slow to collect measurable masses before the plating rate changes due to evaporation. In such circumstances, another common technique used is one in which the metal is first deposited potentiostatically and then selectively dissolved at a different applied potential. The dissolution charge can be used to compute the amount of iron plated and thus the iron plating current. Iron presents a key challenge for implementing such a dissolution-based method. First, iron does not dissolve when an oxidizing potential is applied. In the electroless FeP electrolyte (alkaline, pH = 15.3), oxidation leads to iron oxide surface passive film formation. This hindrance can be alleviated by dissolving the iron in an acidic media; however, iron oxidizes in air during sample transfer from the alkaline electroless bath to the acidic solution leading to discrepancies in the measured mass. Thus, a new method for collecting polarization information of iron deposition was devised and this method was described in detail in section 3.1.5.

We first ascertained the accuracy and reliability of this new method (Figure 3.1) for determination of iron deposition polarization behavior. For validation, acidic solutions (0.6 M H_2SO_4, pH = 0.2) with known concentrations of Fe^{2+} ranging from 0.01 mM to 250 mM were first prepared. With these known concentrations, it was possible to apply the Levich equation (Eq. 3.8) to determine the expected (theoretical) limiting current density on an RDE for the oxidation reaction: $Fe^{2+} \rightarrow Fe^{3+} + e^-$. The expected limiting current densities are shown in *red* in Figure 3.6. The limiting current density was then measured

experimentally using the procedure described in section 3.1.5. These experimentally measured limiting current densities are shown in *blue* in Figure 3.6. The good agreement between the expected and measured limiting current values confirms that this is a reliable method to quantify the Fe^{2+} content of acidic solutions. While the discrepancy between the Levich equation prediction and the experimentally measured current grows larger as the bulk Fe^{2+} concentration increases, the discrepancy is rather small (only 15 %) in the concentration range (0.1 mM to 1 mM) applicable to the solutions prepared by dissolving iron deposits in step (c) of Figure 3.1.

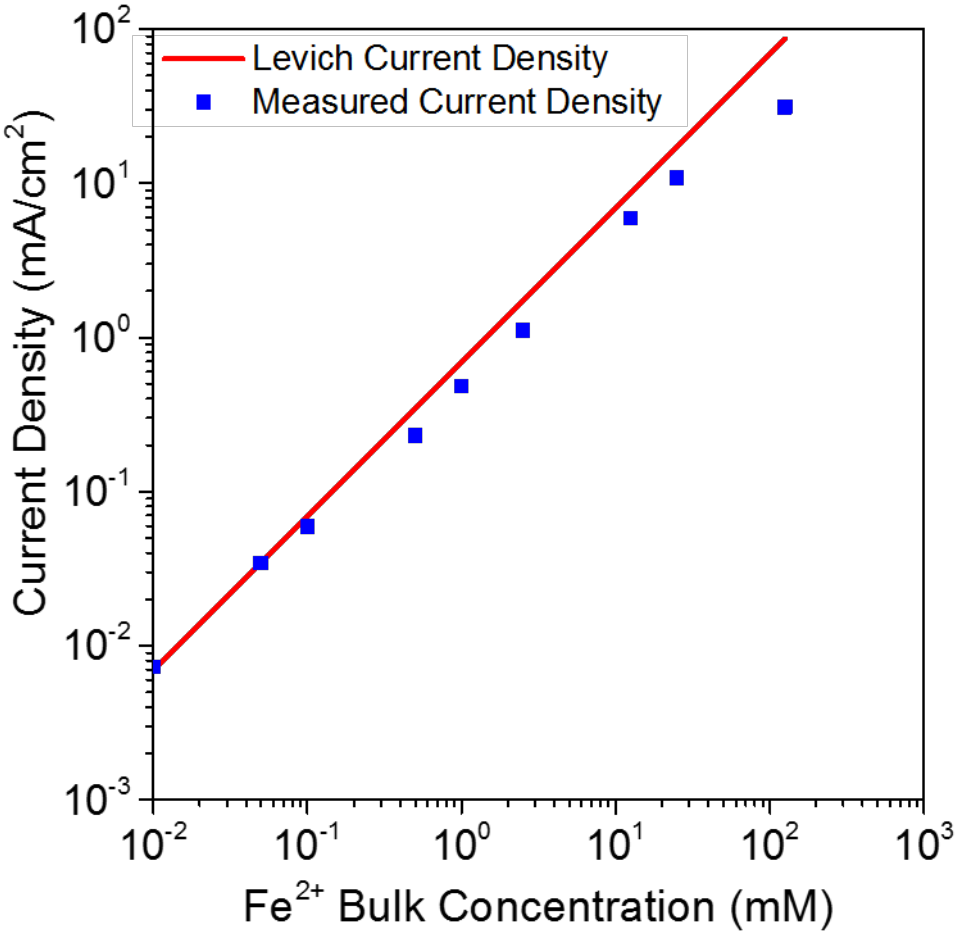

Figure 3.6: The expected limiting current density, determined via the Levich equation, as a function of the Fe^{2+} concentration (*red*) is compared to that experimentally measured on an RDE using an electrolyte containing the specified concentration of Fe^{2+} (*blue*). Good agreement between the two is noted. Electrode area = 0.196 cm^2; RDE rotation speed = 2000 RPM. Electrolyte contained 0.6 M H_2SO_4 (pH = 0.2) with Fe^{2+} concentrations ranging from 0.01 mM to 250 mM.

In addition to the above confirmation, the method developed herein for quantifying the iron deposit mass was validated against conventional weight gain measurements. Iron was first deposited onto an RDE from an electroless FeP electrolyte at an applied potential of -1.05 V vs SHE for 8-12 hours. The change in mass of the RDE electrode was

determined using a weighing balance and this data is shown in *blue* in Figure 3.8. The same electrode was then transferred to the acid bath where the deposit mass was determined using the $Fe^{2+} \rightarrow Fe^{3+}$ limiting current method (section 3.1.5). Reasonable agreement between the two deposited masses was observed (Figure 3.7).

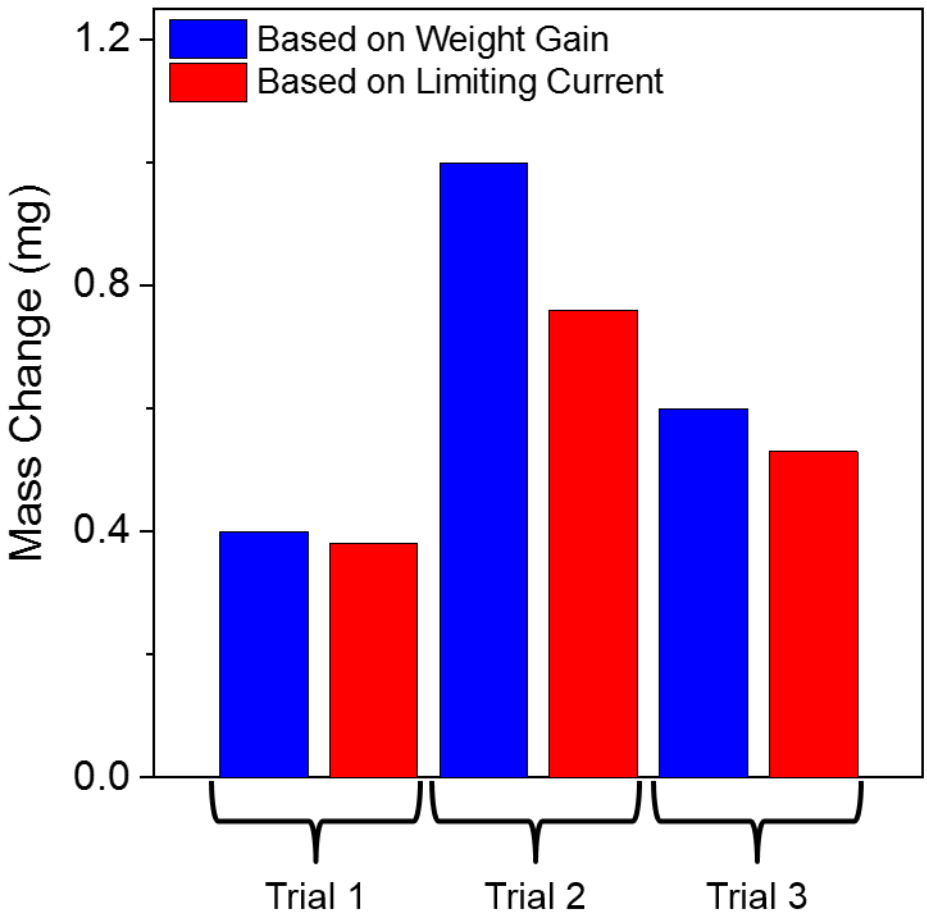

Figure 3.7: For the three trials, iron was first deposited potentiostatically (-1.05 V vs SHE) from a electroless FeP electrolyte and the weight gain of the working electrode was measured (*blue*). The deposited iron was then dissolved in an acid electrolyte and the limiting current of Fe^{2+} oxidation was measured. Based on this limiting current, the plated Fe mass was calculated (*red*). The two methods of mass measurement match reasonably well. Electrode area = 0.196 cm^2; RDE rotation speed = 2000 RPM.

With confidence in the newly developed technique for Fe mass measurement, it is now possible to collect the actual iron deposition polarization curve. This polarization curve is shown in Figure 3.8. From Figure 3.8, it is observed that the iron deposition very quickly reaches a limiting rate as the potential is shifted cathodically. This occurs because much of the Fe^{2+} in the electroless FeP electrolyte precipitates out of solution, leaving only a low concentration of dissolved Fe^{2+} available for deposition. This behavior was confirmed using inductively coupled plasma mass spectrometry (ICP-MS) of the electrolyte, which revealed the dissolved Fe^{2+} to be just about 4 mM. The low Fe^{2+} concentration imposes mass transport (diffusion) limitations, which restrict the plating rate to ~ 4 μm/hr. The inability to have large amounts of dissolved Fe^{2+} in the electroless FeP electrolyte may prove problematic in the future as larger plating rates are desired for practical applications. With the knowledge of iron polarization behavior (Figure 3.8), it is now possible to look at the entire electroless FeP system and determine the mixed potential at which electroless deposition takes place.

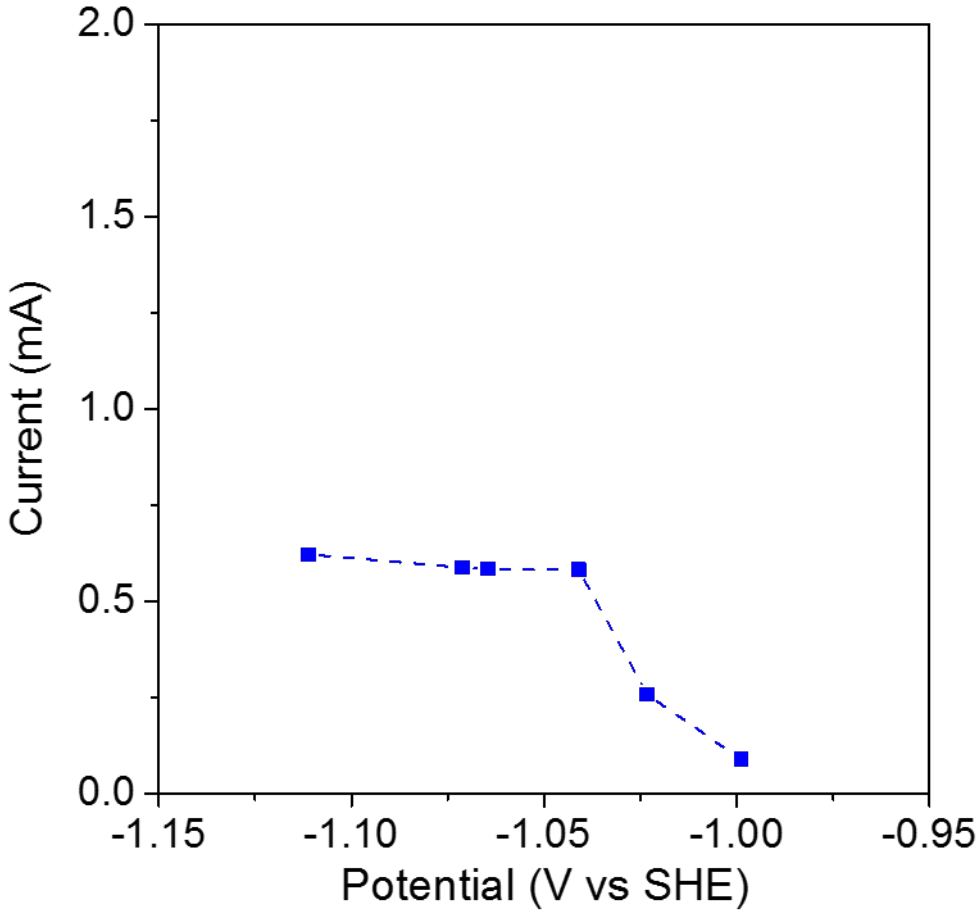

Figure 3.8: Polarization behavior of iron deposition in an electroless FeP plating electrolyte. The behavior was determined using the method described in section 3.1.5. Iron deposition reaches a limiting current at cathodic potentials because of diffusion limitations. Electrode area = 0.196 cm^2. RDE rotation speed = 2000 RPM.

3.3.3 Predicting the Electroless FeP Mixed Potential by Applying Mixed Potential Theory to Partial Polarization Curves

To predict the mixed potential during electroless FeP deposition, charge conservation was applied to the cathodic and anodic reaction partial currents. Based on the

mixed potential theory, the potential at which the net cathodic and anodic currents are equal becomes the predicted mixed potential. This is shown for the lower Pd-activation time (*i.e.*, 100 s) in Figure 3.9. Hypophosphite oxidation currents near the mixed potential (in *black*) were extracted from extrapolation of the data collected in the potential range -0.90 to -0.81 V vs SHE (Figure 3.5). For extrapolation, Butler Volmer kinetics were used. In this case of lower Pd-activation time, the anodic charge is balanced merely by the cathodic reaction of hydrogen evolution, resulting in a predicted mixed potential close to -0.98 V vs SHE. As seen, this potential is slightly more positive than the reduction potential of iron, indicating that iron deposition at this potential is not thermodynamically favored (Figure 3.9). This prediction correlates well with the previous observations (Figures 3.2 and 3.3) that such a low activation time does not facilitate plating of metallic iron.

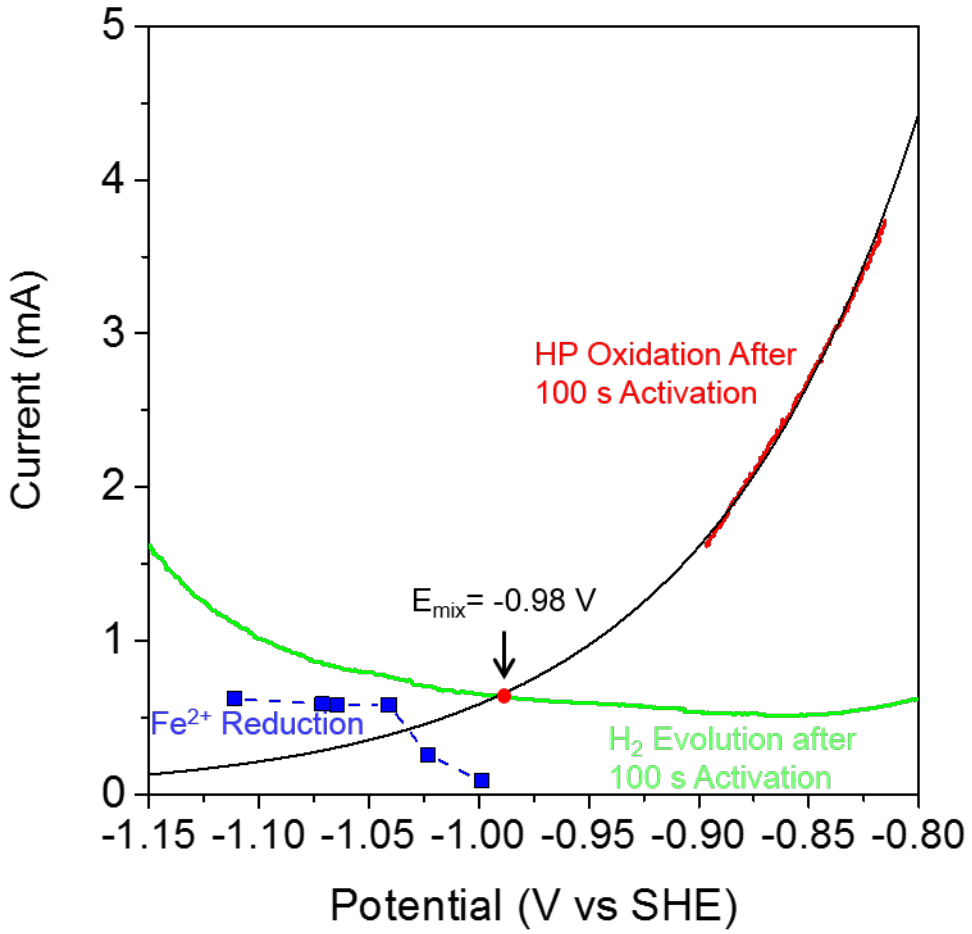

Figure 3.9: Polarization curves for all cathodic and anodic reactions on a substrate that was Pd-activated for 100 s (*i.e.*, low Pd coverage). In order to achieve charge conservation, the net cathodic currents must match the net anodic currents. This occurs at -0.98 V vs SHE, which is the estimated mixed potential of the system. This potential is not cathodic enough to initiate the electroless deposition of Fe – a prediction consistent with observations in Figure 3.2 and 3.3. Electrode area = 0.196 cm^2; RDE rotation speed = 2000 RPM.

In the case of longer Pd-activation time (1000 s) resulting in a substrate that has much higher Pd coverage, applying charge conservation results in a mixed potential of -1.04 V vs SHE (Figure 3.10). Again, hypophosphite oxidation currents near the mixed potential (*black* curve in Figure 3.10) were extracted from extrapolation of the data

collected in the potential range -0.90 to -0.81 V vs SHE (Figure 3.5). For extraction, Butler Volmer kinetics were applied. This mixed potential is cathodic compared to the reduction potential of Fe, and thus electroless deposition of metallic iron is enabled. This again correlates well with experimental data (Figure 3.2 and Figure 3.4) which confirms that a 1000 s Pd-activated Cu substrate can be coated with a thick electroless iron deposit. Furthermore, at the mixed potential of -1.04 V vs SHE, a deposition rate corresponding to 3.0 mA/cm^2 is expected per Figure 3.10. This translates into a deposition rate of 3.9 μm/hr, which too is consistent with experimental measurements of the electroless Fe deposition rate on a 1000 s Pd-activated Cu substrate (4.1 μm/hr based on weight gain measurement).

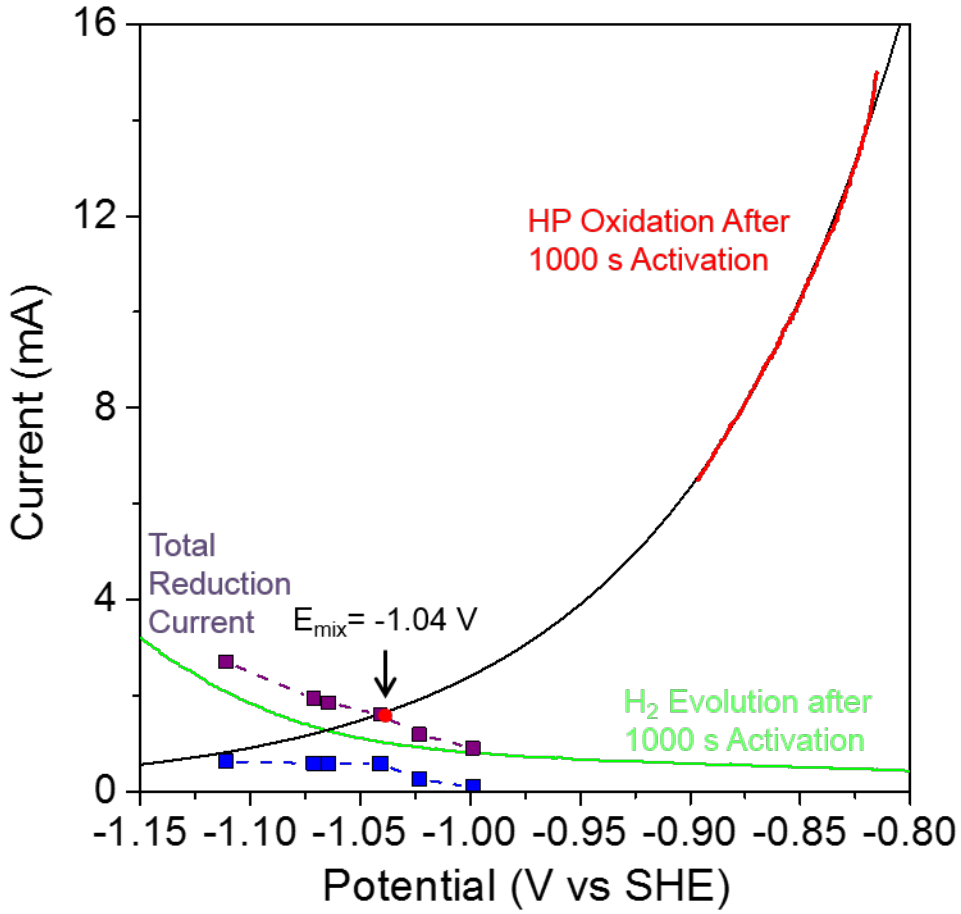

Figure 3.10: Polarization curves of cathodic and anodic reactions on a Cu substrate activated with Pd for 1000 s (*i.e.*, high Pd coverage). Charge conservation requires that the net cathodic current must be equal to the net anodic current. This occurs at -1.04 V vs SHE which is the mixed potential of the electroless Fe deposition system. Thus, the mixed potential is in a region where Fe^{2+} reduction to Fe occurs, and thus electroless Fe deposition is possible. Electrode area = 0.196 cm^2. RDE rotation speed = 2000 RPM.

3.5 Conclusions

During electroless FeP deposition on a Cu substrate from hypophosphite-containing electroless baths, Pd-activation of the Cu substrate plays an important role in

determining whether a sufficiently cathodic mixed potential is established for Fe deposition to be initiated. As the Pd-activation time is increased, the Pd coverage of the Cu substrate increases. This higher Pd coverage leads to higher substrate catalytic activity for hypophosphite oxidation reaction. Using polarization curves measured for all cathodic and anodic half-reactions, and applying the mixed potential theory to balance the cathodic and anodic reaction currents, the mixed potential of the electroless FeP system was correctly estimated as a function of the Pd-activation time. It was shown that, as the Pd-activation time increases, the rate of hypophosphite oxidation also increases. This shifts the surface mixed potential in the cathodic direction. For short Pd-activation times (~100 s), the mixed potential is not cathodic enough for iron deposition to occur. However, after longer activation times (*e.g.*, 1000 s), the mixed potential shifts sufficiently cathodic to be in the region where iron deposition can occur. These studies provide a mechanistic underpinning for the variation of the electroless mixed potential with the Pd-activation time and the visual observation of metallic Fe deposits on Cu substrates treated with Pd above a critical activation time period. A quantitative mathematical process model for this interdependence is developed below in Chapter 4.

CHAPTER 4. Mathematical Model for the Prediction of the Surface Mixed Potential during Early Stages of Electroless Iron Deposition

In chapter 2, a process for plating iron boron (FeB) without the need for palladium (Pd) activation was developed. In chapter 3, a process was developed for deposition of iron phosphorus (FeP) and the critical role of substrate activation by Pd was demonstrated. While Pd-activation is critically needed to enable FeP plating, the amount of Pd used must be minimized due to the high cost of this metal. Pd is a precious metal with price in the range of $20,00-25,000 per kg.[44-46] Moreover, this price is volatile[46] as discussed in detail in the introduction (section 1.4). Because $PdCl_2$ is produced using Pd metal as a reactant, $PdCl_2$ also exhibits price instability. As a result of this price instability, the amount of $PdCl_2$ used in an activation process should be kept at a minimum in order to reduce materials cost

and reduce the dependency of the process on a commodity that is prone to large, sudden fluctuations in price.[44-46,52,53]

In this chapter, a mathematical model is formulated for determining the 'initial' electroless mixed potential during FeP deposition. The model captures the dependence of the electroless mixed potential on the Pd-activation time. Here, 'initial' refers to the early stage process of electroless FeP nucleation on a Pd-activated surface. Note that this stage precedes the FeP growth stage. In the nucleation stage, the surface mixed potential is related to the surface composition, *i.e.*, the Pd coverage of the underlying Cu substrate. Model parameters are measured experimentally as discussed below. It is shown below that the model correctly predicts the critical Pd-activation needed for electroless plating of FeP to initiate. While the numerical parameters in the model are specific to the electroless FeP system developed in chapter 3, the general model development can be applied to other electroless systems which too require activation of a non-catalytic substrate before electroless deposition can commence.[67,69,70]

4.1 Experimental Procedure

4.1.1 Materials and Electrolyte Composition

Electroless deposition was performed from an electrolyte containing 0.05 M ferrous ammonium sulfate [$Fe(NH_4)_2(SO_4)_2 \cdot 6H_2O$, Fisher], 1 M sodium hypophosphite [$NaH_2PO_2 \cdot H_2O$, Sigma Aldrich] as reducing agent, and 0.13 M potassium sodium tartrate

[$C_4H_{12}O_{10}KNa \cdot 4H_2O$, Acros] as complexing agent. Electrolyte pH was set by adding 2 M sodium hydroxide [NaOH, Fisher]. Millipore spec (18.2 MΩ) deionized (DI) water was used to prepare all electrolytes.

Electroless deposition was performed on copper rotating disk electrodes (Pine). When a platinum RDE was used, it was first pre-plated at 1 mA/cm^2 for 150 s in an acidified (pH = 2) electrolyte containing 0.1 M copper sulfate and 500 ppm PEG-4000 additive. The pre-plated Cu thickness was ~0.1 μm. All substrates were polished with alumina micro-slurry and degreased with acetone before use. The copper substrates were then activated in a 2.8 mM palladium chloride ($PdCl_2$) solution for varying activation times. During Pd-activation, the nobler Pd replaces the Cu on the substrate surface through a spontaneous displacement reaction. Pd-activation was followed by a DI water rinse before electroless FeP deposition.

4.1.2 Methods

A jacketed electrochemical cell with a three-electrode configuration was used for polarization measurements of the hypophosphite oxidation half-reaction during electroless Fe plating. The working electrode was a copper rotating disk electrode (RDE) prepared as described above in section 4.1.1. This working electrode was then activated in the 2.8 mM $PdCl_2$ electrolyte for 10800 s (3 hours) to ensure that complete Pd coverage was achieved. The RDE working electrode was rotated at 2000 RPM. The counter electrode was a platinum wire (Encompass) and the reference electrode was a saturated calomel electrode

(SCE, Fisher). Oxidation of hypophosphite was studied in the complete electroless solution, but in an electrode potential range (-0.90 to -0.81 V vs SHE) where other reactions (hydrogen evolution and iron deposition) did not proceed at appreciable rates, thereby allowing reliable measurements of the hypophosphite oxidation rate. All electrochemical tests were performed using a VersaStat Model 4 potentiostat. The electroless bath was maintained at 75 °C by passing hot water through a recirculating water jacket around the cell. Scan rate during electrochemical polarization was 10 mV/s.

Hydrogen evolution polarization measurements were collected similar to hypophosphite oxidation measurements. However, in this case, the electrolyte contained only the tartrate complexant and sodium hydroxide, *i.e.*, the electrolyte did not contain dissolved iron or sodium hypophosphite reductant. Working electrode was either a non-activated Cu RDE or a Cu RDE activated with Pd (procedure described above) for 10800 s to ensure complete Pd coverage.

To collect polarization data for the iron plating half-reaction, iron was deposited potentiostatically on a platinum RDE for 1 hour from the electroless FeP electrolyte described is section 4.1.1. After deposition, the electrode was immersed in acidified DI water (pH~0.2) and the Fe layer was stripped potentiostatically at an applied potential of 0.45 V vs SHE. The dissolved iron (Fe^{+2}) was then oxidized to Fe^{3+} potentiostatically at 1.15 V vs SHE and the limiting oxidation current was measured. This measured limiting current provided the bulk Fe^{+2} concentration (via the Levich equation) and thus the amount of Fe deposited initially on the Pt electrode could be determined. This electrochemical

method provided the Fe deposition rate as a function of the electrode potential during Fe deposition, *i.e.*, the Fe plating polarization behavior. This method was described in more detail in chapter 3 (section 3.1.5).

During the process of substrate activation by Pd (prior to electroless Fe deposition), the surface mixed potential was measured with respect to a reference electrode. The working electrode was the Cu RDE stub that was being activated by Pd. The reference electrode was saturated calomel electrode (SCE) similar to that used in above polarization experiments. Electrode potentials provided below are referenced to the standard hydrogen electrode (SHE).

4.2 Mathematical Model for Predicting the Surface Mixed Potential during Early Stage Electroless Fe Deposition on Pd-activated Cu

4.2.1 Rates of Anodic and Cathodic Reactions during Electroless Fe Deposition

When anodic and cathodic reactions occur spontaneously on a surface that is not biased externally (*i.e.*, at open circuit), the cathodic and anodic currents should be equal in magnitude so that charge conservation is obeyed.[55] Under such conditions, the surface potential is called the 'mixed potential'. During electroless FeP deposition, the surface mixed potential was experimentally measured and reported in a previous chapter (Chapter 3, section 3.2). It was determined that at surface mixed potentials positive to –0.99 V vs

SHE, no iron deposition is observed. To determine the optimal activation time needed to enable electroless FeP deposition, the critical Pd coverage necessary to activate the electrode surface (*i.e.*, to facilitate mixed potentials negative with respect to –0.99 V vs SHE) must be determined.

In the electroless FeP deposition system, the sum of the cathodic (iron deposition, hydrogen evolution and oxygen reduction) and anodic (hypophosphite oxidation) reaction currents must be zero. Here, we use the sign convention that cathodic currents are negative and anodic currents are positive. Furthermore, we assume that the oxygen reduction current is negligibly small. At the electroless process temperature of 75 ^{o}C, the saturation concentration of dissolved oxygen is very small (~10 μA/cm^2) and thus the rate (current) at which it is reduced can be neglected. The mixed potential range of interest being cathodic to the reduction potential for hydrogen evolution suggests that H_2O reduction to H_2 gas is thermodynamically possible and thus must be accounted for in current balance. We now assume that the substrate surface during the initial stage of electroless Fe nucleation is comprised of Pd-activated sites and exposed Cu sites. Assuming I_1 is the hypophosphite oxidation current on Pd, I_2 is the hypophosphite oxidation current on Cu, I_3 is the hydrogen evolution current on Pd, I_4 is the hydrogen evolution current on Cu, and I_5 is the iron deposition current, we can apply current balance:

$$I_1 + I_2 + I_3 + I_4 + I_5 = 0 \qquad [4.1]$$

It has been shown in a previous section (3.3.1) that the current due to hypophosphite oxidation on Cu (I_2) is very small (Figure 3.5) because Cu does not effectively catalyze the hypophosphite oxidation reaction. Thus, we assume I_2=0. The current (I) of any reaction is the product of the local current density (i) and the portion of the electrode area over which the current occurs. Because some electrochemical reactions are only catalyzed by specific surface sites, the area over which these reactions occur can be related to the total area of the substrate (A) multiplied by the surface coverage of the catalytic sites present on the surface (θ):

$$I = (A\theta)i \qquad [4.2]$$

Applying Eq. 4.2, each of the relevant currents in Eq. 4.1 can be expressed in terms of current density and the respective surface site coverage:

$$Ai_1\theta_1 + Ai_3\theta_1 + Ai_4\theta_2 + Ai_5 = 0 \qquad [4.3]$$

In Eq. 4.3, θ_1 is the surface coverage of Pd and θ_2 is the surface coverage of Cu. i_1 is the hypophosphite oxidation current density on Pd, i_3 is the hydrogen evolution current density on Pd, i_4 is the hydrogen evolution current density on Cu, and i_5 is the iron deposition current density. Since all terms contain the total electrode area (A), this term cancels out providing:

$$i_1\theta_1 + i_3\theta_1 + i_4\theta_2 + i_5 = 0 \qquad [4.4]$$

Initially (t=0), the surface consists only of Pd and Cu sites. Thus:

$$\theta_1 + \theta_2 = 1 \qquad [4.5]$$

Combining Eq. 4.4 and Eq. 4.5 leads to Eq. 4.6:

$$i_1\theta_1 + i_3\theta_1 + i_4(1-\theta_1) + i_5 = 0 \qquad [4.6]$$

Eq. 4.6 relates the Pd coverage (θ_1) to the current densities of the various anodic and cathodic reactions prevalent in the electroless system. However, the ultimate goal of the model development is to arrive at a relationship between the Pd coverage (or activation time) and the surface mixed potential during electroless Fe nucleation. In order to determine this relationship, the reaction current densities (i_1, i_3, i_4, i_5,) must be related to the surface potential via established current-potential correlations as shown below.

4.2.2 Current Density – Mixed Potential Relationship

For electrochemical reactions, the general form of the current-overpotential relationship is shown in Eq. 4.7:[71]

$$\frac{i}{i_0} = \frac{C_O(0,t)}{C_O^b} e^{-\alpha f \eta} - \frac{C_R(0,t)}{C_R^b} e^{(n-\alpha) f \eta} \qquad [4.7]$$

$$f = \frac{nF}{RT} \quad [4.8]$$

where i is the current density, i_0 is the exchange current density, $C_O(0,t)$ is the concentration of the oxidized form of a species at the electrode surface, C_O^b is the bulk concentration of the oxidized form of a species, α is the charge transfer coefficient, η is the overpotential, $C_R(0,t)$ is the concentration of the reduced form of a species at the surface, C_R^b is the bulk concentration of the reduced form of a species, and n is the number of electrons. f is a constant that groups the invariant parameters, *i.e.*, the number of electrons (n), Faraday's constant (F), the universal gas constant (R), and temperature (T), as seen in Eq. 4.8.

When electrochemical reaction rates that are well below the mass-transport limit associated with the system, we may neglect concentration gradients and thus assume:

$$\frac{C_O(0,t)}{C_O^b} = 1 \qquad and \qquad \frac{C_R(0,t)}{C_R^b} = 1 \quad [4.9]$$

This assumption leads to the well-known Butler-Volmer equation:[11]

$$\frac{i}{i_0} = e^{-\alpha f \eta} - e^{(n-\alpha) f \eta} \quad [4.10]$$

During electroless Fe plating, the surface mixed potential (E_{mix}) determines the overpotential η for each partial reaction:

$$\eta = E_{mix} - E_o \qquad [4.11]$$

where E_o is the equilibrium potential. Combining Eq. 4.10 and Eq. 4.11 leads to:

$$i = i_0\left[e^{-\alpha f(E_{mix}-E_o)} - e^{(n-\alpha)f(E_{mix}-E_o)}\right] \qquad [4.12]$$

Eq. 4.12 applies to hypophosphite oxidation and hydrogen evolution reactions during electroless Fe deposition because these reactions proceed at rates well below the mass-transport limit. However, for the iron deposition reaction, mass-transport limitations can be quite significant. While 50 mM ferrous ammonium sulfate is present in the electrolyte, much of it precipitates out as solid ferrous oxide upon heating the electroless solution to 75 ^{o}C. The result is that the actual concentration of Fe^{2+} available in the electrolyte is very low (estimated to be ~4 mM based on inductively coupled plasma mass spectrometry). Thus, even small Fe deposition partial currents will cause substantial concentration depletion within the boundary layer and the assumption made above ($C_O(0,t) = C_O^b$) will no longer be correct. In the case where mass transport effects are dominant, we use the well-known Tafel equation that incorporates only the cathodic branch in Eq. 4.7:

$$\frac{i}{i_0} = -\frac{C_O(0,t)}{C_O^b} e^{(\eta-\alpha)f} \qquad [4.13]$$

Current density is related to the gradient of concentration for the reacting species:

$$i = -nFD\nabla C_O \quad [4.14]$$

where n is the number of electrons, F is Faraday's constant, and D is the diffusion coefficient. If a linear concentration gradient is assumed (under steady-state conditions), then we get:

$$i = -\frac{nFD\left(C_O^b - C_O(0,t)\right)}{\delta} \quad [4.15]$$

where δ is the diffusion boundary layer thickness. In the specific case where the deposition current equals the limiting current (i_l), the surface concentration reaches zero, and thus:

$$i_l = -\frac{nFD\left(C_O^b\right)}{\delta} \quad [4.16]$$

Dividing Eq. 4.15 by Eq. 4.16 yields:

$$\frac{i}{i_l} = 1 - \frac{C(0,t)}{C_O^b} \quad [4.17]$$

$$\frac{C(0,t)}{C_O^b} = 1 - \frac{i}{i_l} \quad [4.18]$$

Equations 4.11, 4.13 and 4.18 can be combined to provide:

$$i = -i_0\left(1-\frac{i}{i_l}\right)e^{(\eta-\alpha)f(E_{mix}-E_o)} \qquad [4.19]$$

Combining both forms of the current-potential relationship (Eq. 4.12 for hypophosphite oxidation and hydrogen evolution, and Eq. 4.19 for iron deposition) into the current balance equation (Eq. 4.6) yields an expression (Eq. 4.20) for the relationship between the electroless FeP mixed potential (E_{mix}) and the coverage of palladium (θ_1):

$$\begin{aligned} i_{0,1}\left[-e^{-\alpha_1 f(E_{mix}-E_{o,1})}-e^{(n-\alpha_1)f(E_{mix}-E_{o,1})}\right]\theta_1 \\ +\, i_{0,3}\left[e^{-\alpha_3 f(E_{mix}-E_{o,3})}-e^{(n-\alpha_3)f(E_{mix}-E_{o,3})}\right]\theta_1 \\ +\, i_{0,4}\left[e^{-\alpha_4 f(E_{mix}-E_{o,4})}-e^{(n-\alpha_4)f(E_{mix}-E_{o,4})}\right](1-\theta_1) \\ -\, i_{0,5}\left(1-\frac{i_5}{i_{l,5}}\right)e^{(\eta-\alpha_5)f(E_{mix}-E_{o,5})}=0 \end{aligned} \qquad [4.20]$$

4.2.3 Experimental Determination of the Kinetics Parameters in Eq. [4.20]

To utilize Eq. 4.20 to compute the electroless mixed potential, the various kinetics parameters, *i.e.*, for the hypophosphite oxidation on Pd ($i_{0,1}$, α_1), hydrogen evolution on Pd ($i_{0,3}$, α_3), hydrogen evolution on Cu ($i_{0,4}$, α_4) and iron deposition ($i_{0,5}$, α_5), must be determined. Experimental polarization data (as shown in Figures 3.5, 3.8, 3.9 and 3.10) must be used to determine these kinetic parameters. Experimental polarization curves for each half-reaction were fitted in Origin to the Butler-Volmer or Tafel expressions and the kinetics parameters that provided the best fit were determined. The fitting results for the hypophosphite oxidation reaction on Pd are shown in Figure 4.1. The exchange current

density ($i_{0,1}$) value that provided the best fit was 5.92 mA/cm^2 and the best fit charge transfer coefficient (α_1) was determined to be 1.76.

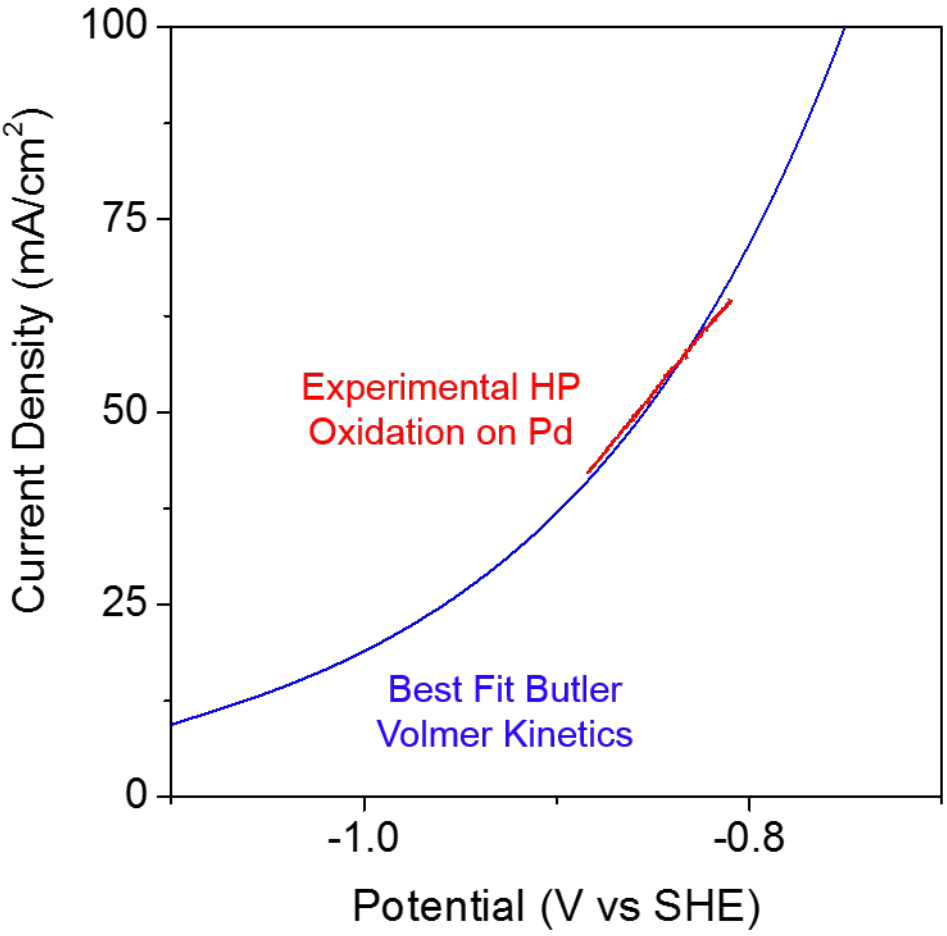

Figure 4.1: Butler-Volmer kinetics for hypophosphite (HP) oxidation on Pd (*blue*). Experimental polarization data (*red*) was collected on a rotating disc electrode (details provided in section 4.1.2). The best fit parameters were: exchange current density ($i_{0,1}$) of 5.92 mA/cm^2 and charge transfer coefficient (α_1) of 1.76.

The comparison between Butler-Volmer theory and experimental polarization data for hydrogen evolution reaction on both Pd and Cu is shown in Figure 4.2. From this

comparison, the exchange current density for H_2 evolution on Pd ($i_{0,3}$) was determined to be 0.102 mA/cm^2 and the corresponding charge transfer coefficient for H_2 evolution on Pd (α_3) was determined to be 0.25. The exchange current density for H_2 evolution on Cu ($i_{0,4}$) was determined to be 0.059 mA/cm^2 and the corresponding charge transfer coefficient (α_4) was determined to be 0.24.

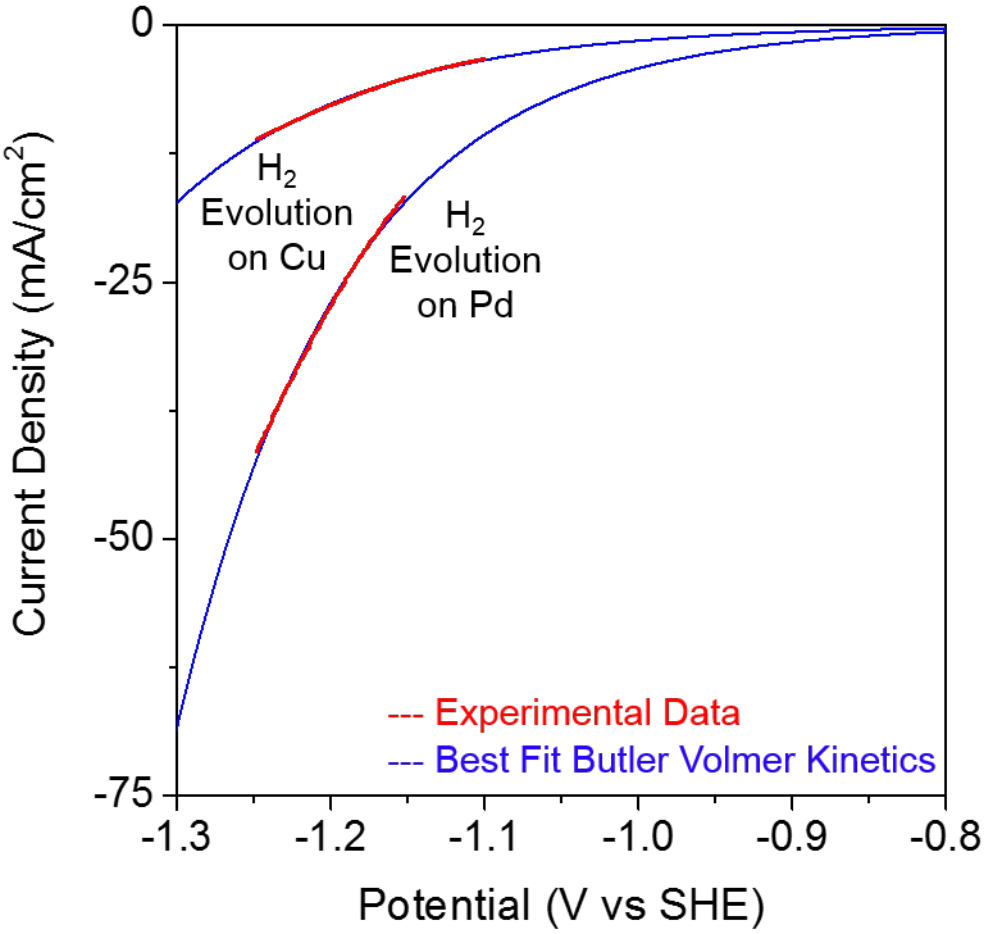

Figure 4.2: Comparison between Bulter-Volmer theory (*blue*) and experimental data (*red*) for the hydrogen (H_2) evolution reaction on Pd and Cu substrates. Experimental polarization data was collected on a rotating disc electrode (details provided in section 4.1.2). The best fit parameters in the Butler-Volmer equation are as follows: exchange current density for H_2 evolution on Pd ($i_{0,3}$) is 0.102 mA/cm^2 and charge transfer coefficient (α_3) is 0.25; exchange current density for H_2 evolution on Cu ($i_{0,4}$) is 0.059 mA/cm^2 and charge transfer coefficient (α_4) is 0.24.

A comparison between Tafel kinetics (Eq. 4.19) and experimental polarization data for the Fe plating half-reaction is provided in Figure 4.3. The kinetics parameters that provide the best agreement between theory and experiment were determined to be:

exchange current density ($i_{0,5}$) of 0.13 mA/cm^2 and corresponding charge transfer coefficient (α_5) of 1.80.

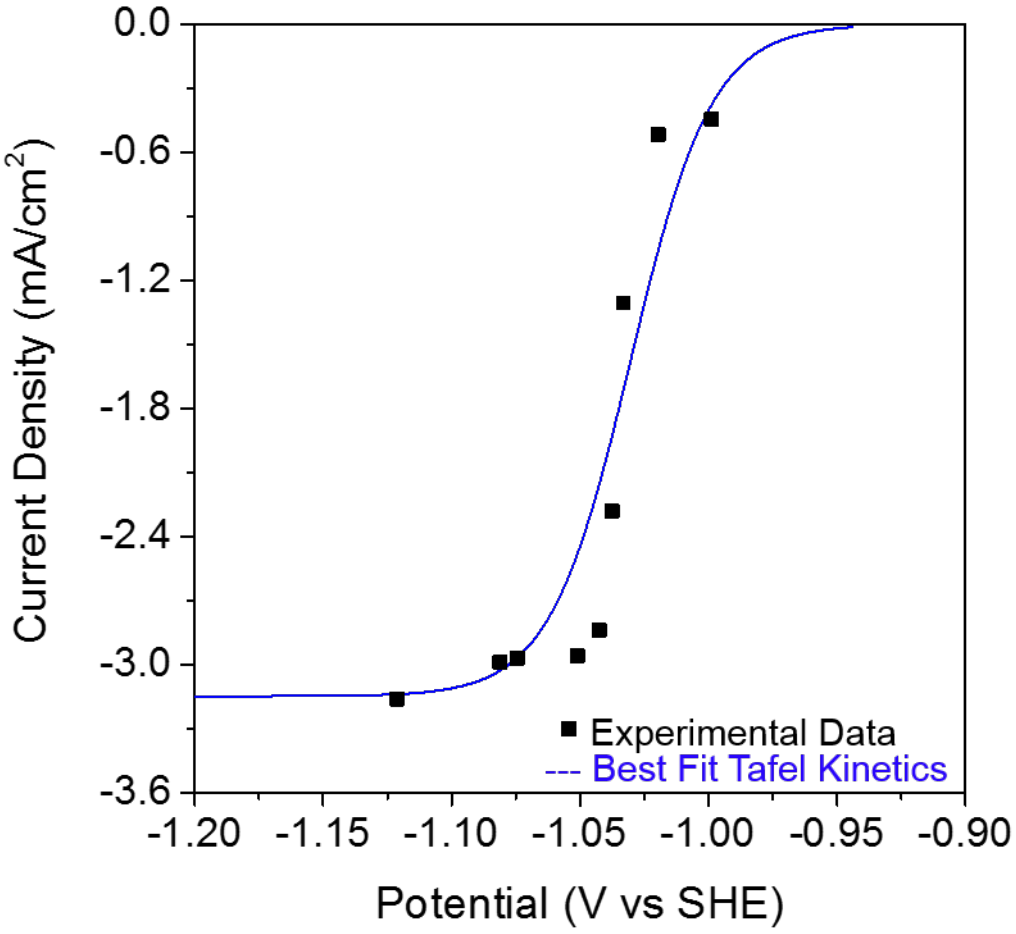

Figure 4.3: Tafel kinetics (Eq. 4.19) for the iron deposition partial current during electroless Fe plating (*blue*). Experimental polarization data points were collected on a rotating disc electrode under conditions described in section 4.1.2. Following kinetics parameters provide the best agreement between theory and experiment: exchange current density ($i_{0,5}$) of 0.13 mA/cm^2 and charge transfer coefficient (α_5) of 1.80.

4.2.4 Predicting the Electroless Mixed Potential as a Function of the Palladium Surface Coverage

Once all the kinetic parameters were determined, it was possible to use Eq. 4.20 to plot the relationship between the mixed potential during electroless FeP nucleation and the initial Pd surface coverage. This relationship is depicted in Figure 4.4. It is known, based on the Pourbaix diagram for iron (Figure 3.2b) that iron deposition occurs only if the mixed potential is cathodic with respect to the reduction potential of Fe (–0.99 V vs SHE in alkaline media). This cathodic region of iron deposition is marked in blue in Figure 4.4. It is thus evident from Figure 4.4 that a minimum Pd coverage of 10.6% (θ_1=0.106) is needed to enable metallic iron deposition. However, in practical applications, Pd surface coverage during surface activation cannot be controlled directly. It can be indirectly controlled through variation of the Pd-activation time and other activation bath parameters such as Pd^{+2} concentration. Thus, a mathematical relationship between the Pd surface coverage and Pd-activation time is required, which can allow us to formulate a model that predicts the minimum activation time needed to provide enough surface catalytic activity for electroless Fe deposition, *i.e.*, one that meets the criterion: $E_{mix} < -0.99$ V vs SHE. This is developed in the next section.

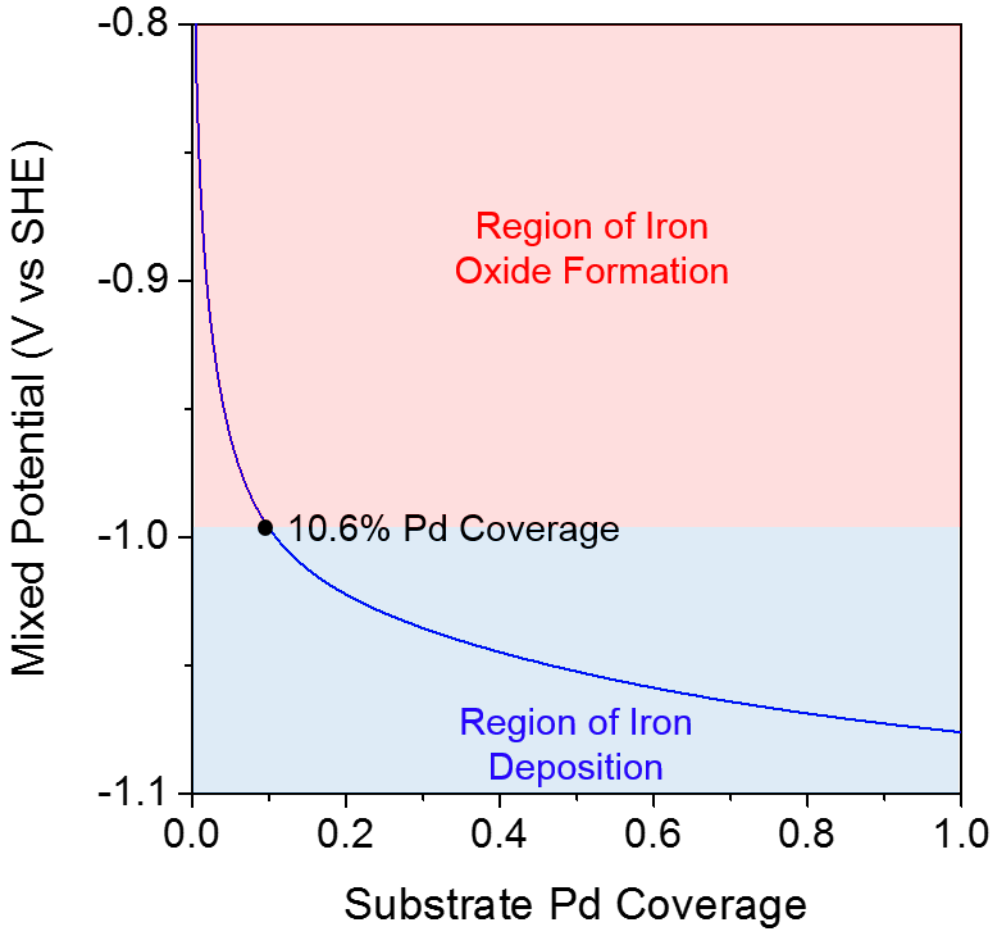

Figure 4.4: Model prediction of the surface mixed potential during electroless FeP deposition as a function of the Pd coverage provided by activation. Iron is deposited only in the region where the mixed potential is cathodic to the reduction potential (–0.99 V vs SHE, blue region). When the mixed potential is anodic to the reduction potential (red region), only iron oxide formation is possible as shown in Chapter 3. It is thus inferred that a minimum Pd coverage of 10.6% is required for spontaneous electroless iron deposition under the conditions employed in this study.

4.3 Time Evolution of the Pd Surface Coverage during Activation Treatment

4.3.1 Mixed Potential Transients during Palladium Activation

Figure 4.5 shows the change in mixed potential of a Cu RDE substrate during the process of activating it with Pd in a 2.8 mM $PdCl_2$ solution. During activation, the surface mixed potential of the Cu RDE is established by the Cu oxidation reaction and the Pd^{+2}-reduction reaction. Both these reactions proceed simultaneously:

$$Cu^0 \rightarrow Cu^{2+} + 2e^- \qquad [4.21]$$

$$Pd^{2+} + 2e^- \rightarrow Pd^0 \qquad [4.22]$$

As the Cu surface gets gradually covered with Pd, the surface mixed potential gradually drifts in the anodic (positive) direction. From such potential transients, the magnitude of change in the surface mixed potential ($\Delta E_{mix} = E_{mix} - E_{mix,t=0}$) could be determined. Typical mixed potential changes over time during Pd-activation of Cu are shown in Figure 4.5.

It should be noted that, in addition to the reactions 4.21 and 4.22, parasitic reactions such as oxygen reduction could also occur; however, these do not drastically alter the mixed potential transients during Pd-activation. Mixed potential change measured during Pd-activation from a de-oxygenated electrolyte showed similar trends as in Figure 4.5.

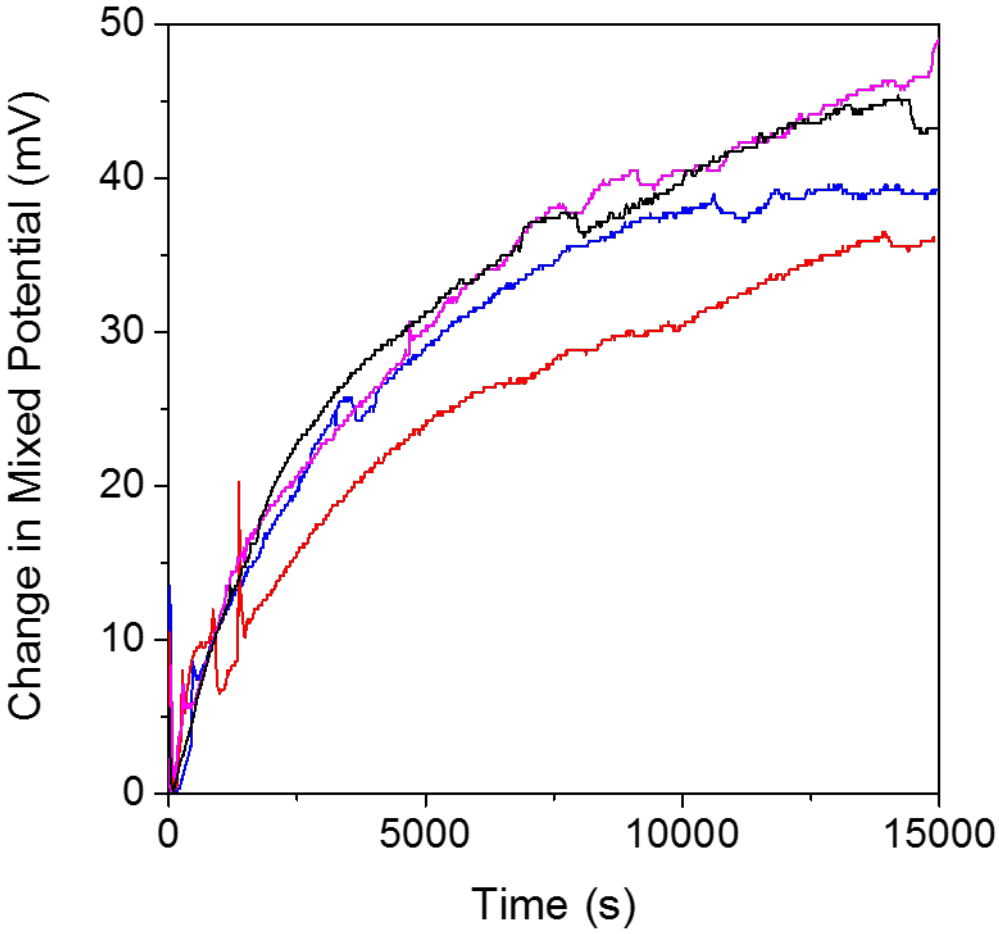

Figure 4.5: Repeated trials showing the change of the surface mixed potential (ΔE_{mix}) over time during Pd-activation of Cu RDE. Results of several trials are shown to highlight the noise associated with the mixed potential measurements. In spite of the noise, the general trends (graduate drift in mixed potential in the positive direction) appear reproducible.

The mixed potential during Pd-activation is the potential at which the magnitude of the oxidation current (for reaction 4.21) equals the magnitude of the reduction current (for reaction 4.22). Thus, we can write:

$$I_6 + I_7 = 0 \quad [4.23]$$

In Eq. 4.23, I_6 is the Cu oxidation current and I_7 is the Pd^{2+}-reduction current. Cu oxidation takes places on exposed Cu sites whereas Pd^{+2}-reduction has been observed to occur both on exposed Cu portions as well as on freshly deposited Pd. Thus, Eq. 4.23 can be written as:

$$A\theta_3 i_6 + A(\theta_3 + \theta_4) i_7 = 0 \quad [4.24]$$

where A is the total surface area, i_6 is the Cu oxidation current density and i_7 is the Pd^{2+} reduction current density. The surface coverage of Cu (θ_3) and that of Pd (θ_4) are related as:

$$\theta_3 + \theta_4 = 1 \quad [4.25]$$

Eq. 4.25 and Eq. 4.24 can be combined to yield:

$$(1 - \theta_4) i_6 + i_7 = 0 \quad [4.26]$$

Next, the current densities for each electrochemical reaction are related to the surface mixed potential. The potential-current relationship of the Cu oxidation reaction can be represented by the Tafel equation:[71,72]

$$i_6 = i_{0,6} e^{\alpha_6 f(V_{mix} - E_{0,6})} \quad [4.27]$$

In this equation $i_{0,6}$ is the exchange current density, α_6 is the anodic charge transfer coefficient, and f is the same parameter as defined in Eq. 4.8. V_{mix} is the mixed potential during Pd-activation of Cu and $E_{0,6}$ is the equilibrium potential.

For the Pd deposition reaction (4.22), due to the fact that the bulk $PdCl_2$ concentration is very low (2.8 mM), we assume that this reaction is mass transport limited. Thus, the rate of this reaction is:

$$i_7 = i_{l,7} = -\frac{nFD[Pd^{2+}]}{\delta} \quad [4.28]$$

This steady-state approximation is only valid at long times ($t > \delta^2/D$).[71,72] Taking the boundary layer at the Cu RDE to be δ ~ 0.01 cm, the diffusion coefficient of Pd^{2+} to be D ~10^{-5} cm^2 s^{-1}, the time needed to achieve pseudo steady-state is t~10 s. Since the mixed potential transient during Pd-activation develops over the course of ~10000 s, the assumption of pseudo steady-state is valid.

Eq. 4.27 and 4.28 can be inserted into the charge balance equation (Eq. 4.26) to provide a relationship between mixed potential (V_{mix}) and Pd surface coverage (θ_4):

$$(1-\theta_4)i_{0,6}e^{\alpha_6 f(V_{mix}-E_{0,6})} + i_{l,7} = 0 \quad [4.29]$$

$$e^{\alpha_6 f(V_{mix}-E_{0,6})} = \frac{-i_{l,7}}{(1-\theta_4)i_{0,6}} \quad [4.30]$$

$$\alpha_6 f\left(V_{mix} - E_{0,6}\right) = ln\left(\frac{-i_{l,7}}{(1-\theta_4)i_{0,6}}\right) \quad [4.31]$$

$$V_{mix} = E_{0,6} + \frac{1}{\alpha_6 f} ln\left(\frac{-i_{l,7}}{(1-\theta_4)i_{0,6}}\right) \quad [4.32]$$

$$V_{mix} = E_{0,6} + \frac{1}{\alpha_6 f}\left[ln\left(\frac{-i_{l,7}}{i_{0,6}}\right) - ln(1-\theta_4)\right] \quad [4.33]$$

Initially, *i.e.*, at t=0 s, θ_4=0. Thus, the initial mixed potential is:

$$V_{mix,t=0} = E_{0,6} + \frac{1}{\alpha_6 f}\left[ln\left(\frac{-i_{l,7}}{i_{0,6}}\right)\right] \quad [4.34]$$

It is important to determine how the mixed potential changes as a function of the Pd coverage, so we define a parameter $\Delta V_{mix} = V_{mix} - V_{mix,t=0}$ which, from Eq. 4.33 and Eq. 4.34, is given as:

$$\Delta V_{mix} = \frac{1}{\alpha_6 f}[-ln(1-\theta_4)] \quad [4.35]$$

For small values of θ_4, $ln(1-\theta_4)$ can be approximated as $-\theta_4$. This reduces Eq. 4.35 to that shown in Eq. 4.36:

$$\Delta V_{mix} = \frac{1}{\alpha_6 f}\theta_4 \quad [4.36]$$

This shows that the relationship between the change in the mixed potential and the Pd coverage is linear for small θ_4 (typically $\theta_4 < 0.25$). In the next section, we relate the Pd coverage to time using a first-order reaction kinetics model. The time-dependence of surface coverage together with Eq. 4.36 allows us to relate ΔV_{mix} to Pd-activation time, thereby facilitating a direct comparison of the model predictions to experimental data (Figure 4.5).

4.3.2 Kinetics Model of the Pd Surface Activation Process

Let us assume that the rate of Pd deposition during surface activation is linearly proportional to the un-activated surface area fraction $1 - \theta_4$. Thus, the rate of change of Pd surface coverage during activation can be written as:

$$\Gamma_s \frac{d\theta_4}{dt} = kC_s(1 - \theta_4) \quad [4.37]$$

where Γ_s is the saturation Pd surface concentration, k is the first order reaction rate constant and C_s is the concentration of Pd^{2+} ions near the electrode surface.

The concentration of palladium ions at the electrode surface (C_s) is not known *a priori*. To determine the Pd ion surface concentration, the transport of Pd ions towards the electrode surface must be considered. Pd ions diffuse from the bulk to the electrode surface where they are consumed to produce metallic Pd. Assuming that there is no accumulation of Pd ions at the surface, the two processes of diffusion and surface reaction must occur at equal rates:

$$D \frac{dC}{dx} = kC_s(1 - \theta_4) \quad [4.38]$$

The left side of Eq. 4.38 is the diffusion flux of Pd ions to the surface with D being the diffusion constant of Pd ions. The right side of Eq. 4.38 represents the rate of Pd ion consumption (through deposition) and is thus the same as the right side of Eq. 4.37.

It is assumed that a pseudo steady-state is reached during the Pd deposition process so that after a short concentration relaxation time (typically 10 s), the concentration profile becomes linear. Assuming a linear concentration profile, Eq. 4.38 thus becomes:

$$D\frac{C_b - C_s}{\delta} = kC_s(1-\theta_4) \qquad [4.39]$$

In Eq. 4.39, C_b is the bulk concentration of Pd ions and δ the boundary layer thickness. Eq. 4.39 can be rearranged to express the Pd ion surface concentration (C_s) as a function of the Pd surface coverage (θ_4):

$$C_s = \frac{\frac{DC_b}{\delta k}}{1 + \frac{D}{\delta k} - \theta_4} \qquad [4.40]$$

This function for Pd ion surface concentration (Eq. 4.40) can then be implemented into Eq. 4.37, resulting in Eq. 4.41:

$$\Gamma_s \frac{d\theta_4}{dt} = \frac{\frac{DC_b}{\delta}(1-\theta_4)}{1 + \frac{D}{\delta k} - \theta_4} \qquad [4.41]$$

We now define two constants, A and B, as:

$$A = \frac{DC_b}{\delta} \quad [4.42]$$

$$B = 1 + \frac{D}{\delta k} \quad [4.43]$$

Given Eq. 4.42 and 4.43, Eq. 4.41 now becomes:

$$\Gamma_s \frac{d\theta_4}{dt} = \frac{A(1-\theta_4)}{B-\theta_4} \quad [4.44]$$

Eq. 4.44 can be integrated knowing that at the initial time (*t*=0) there is no Pd on the surface, *i.e.*, $\theta_4 = 0$.

$$\int_0^{\theta_4} \frac{B-\theta_4}{1-\theta_4} d\theta_4 = \frac{A}{\Gamma_s} \int_0^t dt \quad [4.45]$$

$$\theta_4 - (B-1)ln(1-\theta_4) = \frac{A}{\Gamma_s} t \quad [4.46]$$

For small changes in Pd coverage (less than 25%), $ln(1-\theta_4)$ can be approximated to $-\theta_4$. With this approximation, Eq. 4.46 becomes:

$$\theta_4 - (B-1)(-\theta_4) = \frac{A}{\Gamma_s} t \quad [4.47]$$

$$\theta_4 = \frac{A}{B\Gamma_s} t = mt \quad [4.48]$$

Thus, the Pd surface coverage increases linearly with time when θ_4 is small (typically < 0.25), where *m* is the slope or constant of proportionality.

4.3.3 Modeling Pd Coverage as a Function of Pd-Activation Time

Eq. 4.36 established a proportionality between ΔV_{mix} and θ_4 as:

$$\Delta V_{mix} = \frac{1}{\alpha_6 f} \theta_4 \quad [4.49]$$

Eq. 4.36 combined with Eq. 4.48 provides:

$$\Delta V_{mix} = \frac{1}{\alpha_6 f} \frac{A}{B\Gamma_s} t = mt \quad [4.50]$$

System behavior consistent with Eq. 4.50 is seen in Fig 4.6 (experimental data). In Fig 4.6, the potential changes linearly with time by ~8 mV in 700 s, *i.e.*, a 20% change in the mixed potential during the first 700 s of Pd deposition. During the first 700 s then, Eq. 4.48 would

suggest that the Pd surface coverage should also increase to about 20%. This provides a slope m of 3.1×10^{-4} s^{-1} such that we may write:

$$\theta_4 = mt = (3.1 \times 10^{-4})t \qquad for\ \theta_4 < 0.25 \qquad [4.51]$$

Eq. 4.37 is shown by the model curve in Fig 4.6.

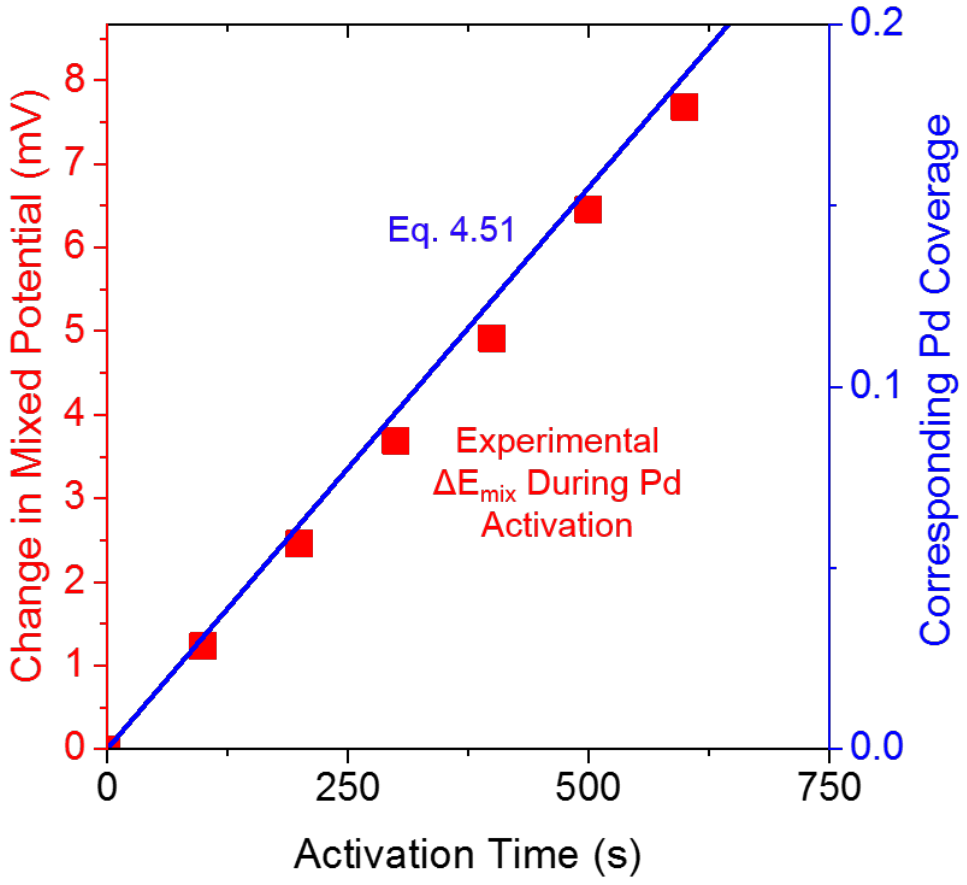

Figure 4.6: Experimental data for the change in mixed potential during Pd-activation is shown (*red*, left y-axis). On the right y-axis, the corresponding Pd coverage is shown. Both variables change linearly with respect to time per Eq. 4.48 and Eq. 4.50.

4.4 Mathematical Model for Predicting the Mixed Potential during Electroless FeP Initiation on a Pd-Activated Cu Substrate.

In section 4.2, a model was formulated for computing the mixed potential during early stage electroless Fe nucleation as a function of the Pd coverage (Eq. 4.20) of the underlying Cu substrate. In section 4.3, a model was developed for determining the Pd coverage as a function of the Pd-activation time (Eq. 4.48). Combining these two models provides a means for determining the mixed potential in the electroless FeP system as a function of the Pd-activation time. This is shown is Eq. 4.52.

$$\begin{aligned} & i_{0,1}\left[e^{-\alpha_1 f\left(E_{mix}-E_{0,1}\right)}-e^{(n-\alpha_1)f\left(E_{mix}-E_{0,1}\right)}\right]mt \\ & \quad + i_{0,3}\left[\,e^{-\alpha_3 f\left(E_{mix}-E_{0,3}\right)}-e^{(n-\alpha_3)f\left(E_{mix}-E_{0,3}\right)}\right]mt \\ & \quad + i_{0,4}\left[\,e^{-\alpha_4 f\left(E_{mix}-E_{0,4}\right)}-e^{(n-\alpha_4)f\left(E_{mix}-E_{0,4}\right)}\right](1-mt) \\ & \quad - \; i_{0,5}\left(1-\frac{i_5}{i_{l,5}}\right)e^{(\eta-\alpha_5)f\left(E_{mix}-E_{0,5}\right)}=0 \end{aligned} \qquad [4.52]$$

Eq. 4.52 can be used to evaluate the dependence of the mixed potential (E_{mix}) on the Pd-activation time (t). The parameters needed for computing E_{mix} vs. t are provided in Table I, with $i_{l,5} = 3.1$ mA/cm^2. Figure 4.7 shows the E_{mix} vs. t dependence. Iron deposition is expected at a mixed potential cathodic with respect to the Fe^{2+}/Fe^0 equilibrium potential (-0.99 V vs SHE). Figure 4.7 indicates that the critical Pd-activation time ($t_{critical}$) needed to provide sufficient surface catalytic activity and enable electroless Fe deposition is $t_{critical}$ = 278 s. This point is marked with a red dot on Figure 4.7. In chapter 3 (section

3.2), it was discussed that iron deposition is not visually observed on a Cu substrate until it was activated by Pd for more than 300 s (black line on Figure 4.7). This observation of critical Pd activation time agrees well with the model prediction.

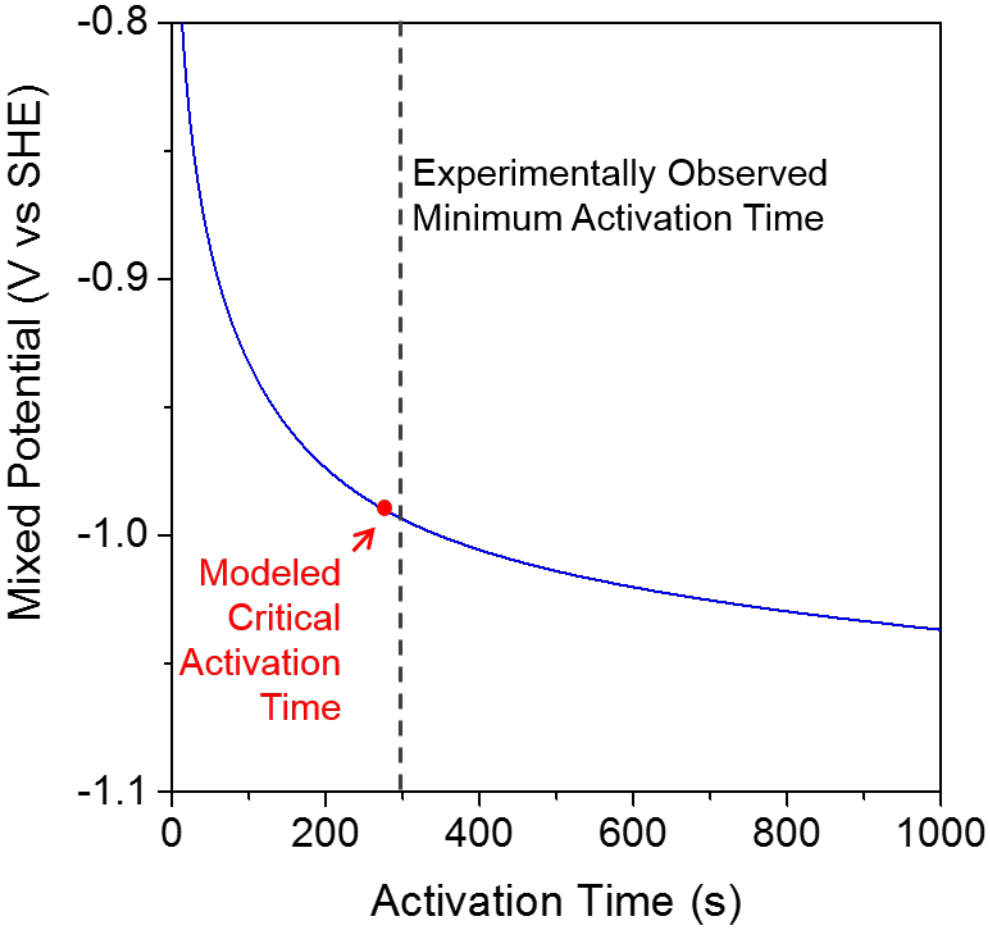

Figure 4.7: Model of the electroless FeP mixed potential as a function of Pd-activation time. The model indicates that the minimum activation time needed to achieve iron deposition is 278 s (shown as *red* dot). Experimental observations have indicated that the minimum activation time necessary for iron deposition is 300 s (section 3.2). Good agreement between model and experimental data is noted.

Table I: System Parameters for Modeling the Initial Electroless FeP Mixed Potential as a Function of Pd-Activation Time.

Half-reaction Parameter	HP Oxidation on Pd (1)	H_2 Evolution on Pd (3)	H_2 Evolution on Cu (4)	Iron Deposition (5)
i_0 (mA/cm^2)	5.92	0.102	0.059	0.13
α	1.76	0.25	0.24	1.80
E_0 (V vs SHE)	-1.15	-0.80	-0.80	-0.99
m	3.1×10^{-4}	3.1×10^{-4}	3.1×10^{-4}	3.1×10^{-4}

4.5 Conclusions

A mathematical model for the 'initial' mixed potential, *i.e.*, that during the nucleation stage of electroless FeP deposition was developed. Model parameters, such as electrochemical kinetics and mass-transport properties associated with the various half-reactions, were first measured and then applied in the model. The model provides the quantitative dependence of the surface mixed potential during Fe deposition as a function of the substrate's Pd-activation time. Higher the activation time, more cathodic is the surface mixed potential. At a critical Pd-activation time, the electroless mixed potential enters the regime where metallic Fe deposits are formed. For the conditions employed herein, this critical Pd-activation time was determined to be 278 s, very similar to that observed experimentally (300 s). The model developed herein may be used to design optimal activation treatments of the substrate before electroless Fe deposition. Furthermore, the model can be applied to other electroless systems (*e.g.*, Ni and Co) where

Pd-activation is a necessary surface treatment step to impart catalytic activity to an otherwise non-catalytic substrate.

CHAPTER 5. Conclusions and Future Work

5.1 Conclusions

Investigations into the polarization and the mixed potential behavior of the electroless iron boron (FeB) system showed that increasing the concentration of the reducing agent (sodium borohydride) accelerated the kinetics of borohydride oxidation on iron. This enabled the development of an electroless FeB deposition process that required neither palladium (Pd) activation of the substrate nor the use of a sacrificial anode. FeB films deposited using the electroless process developed in this work were characterized using scanning electron microscopy (SEM), X-ray photoelectron spectroscopy (XPS) and X-ray diffraction (XRD). These studies confirmed that the films contained boron and were amorphous in nature. Electroless plating rate was 0.24 μm/hr. Electrochemical corrosion testing showed reasonable corrosion resistance which was somewhat inferior to that of amorphous nickel films yet the FeB corrosion resistance was acceptable for practical applications in PCBs.

A process for deposition of electroless iron phosphorus (FeP) films without the use of a sacrificial anode was developed. By observing the dependence of the mixed potential on the Pd-activation time and by measuring the deposit composition via XPS, it was demonstrated that Pd-activation plays a critical role in enabling sustained iron deposition. Through polarization measurements it was determined that, as the Pd-activation time increased, the kinetics of the hypophosphite oxidation reaction increased due to the larger Pd coverage of the underlying copper substrate. This increased catalytic activity of the substrate enables a cathodic shift in the electroless mixed potential thereby facilitating growth of electroless Fe deposits.

A mathematical model was then formulated to determine the minimum or critical Pd-activation time ($t_{critical}$) necessary to achieve iron deposition. Charge conservation was applied as a basis for relating the electroless FeP mixed potential to the Pd coverage (and thus the Pd-activation time) of the Cu substrate. Knowing how cathodic the mixed potential must be for electroless Fe deposition, we could compute the critical Pd-activation time to be $t_{critical} = 278\ s$ for the conditions used in the present work. The critical activation time determined based on the model matched well with experimental data.

5.2 Outlook and Future Work

Electroless FeP shows promise as a candidate material to replace electroless amorphous nickel-alloys. The processes for electroless iron deposition developed herein eliminate the use of a sacrificial anode and minimize the use of palladium activation. This

allows for the possibility that electroless iron could be used in many applications such as printed circuit boards. However, for electroless FeP in particular, there are still two key shortcomings that must be addressed before process implementation.

The first issue that must be resolved is the slow electroless FeP plating rate. The electroless FeP electrolyte is highly alkaline since the kinetics of hypophosphite oxidation are fast only at high pH. Unfortunately, this alkalinity also makes the electrolyte susceptible towards precipitation in the form of Fe_3O_4, which is a dark-colored mixed iron oxide. Due to this precipitation, the actual concentration of Fe^{2+} in the electrolyte is very low, *i.e.*, in the ~4 mM range as measured via inductively coupled plasma mass spectrometry. Limited by this low concentration of Fe^{2+}, the electroless Fe plating rates are usually low. This is apparent in the low transport-limited currents seen in the polarization curve in Figure 3.8. In order to increase the plating rate of electroless FeP, the concentration of Fe^{2+} dissolved in solution must be increased. To increase the Fe^{2+} concentration, new complexing agents are desired. Tartrate is a good complexant for Fe^{3+}; however, above pH 8, its ability of complex Fe^{2+} decreases with increasing pH.[73] In order to increase the availability of Fe^{2+} for deposition, an alternative complexing agent that forms stable iron complexes at high pH (>14) should be investigated. The release of Fe^{2+} from the complex should also be relatively fast, so that the electroless FeP deposition does not encounter kinetic hindrances. Some complexing agents common to other electroless systems that may improve Fe^{2+} include citrate, ethylenediaminetetraacetic acid, acetate, and succinate.

A second complication with electroless FeP is that the phosphorus content of the films is not sufficiently large for the desired amorphous characteristic to be present. The FeP films fabricated herein had only 1.2 wt.% of P as measured using energy-dispersive X-ray spectroscopy. Investigations into electroplated FeP films confirmed amorphous characteristic after incorporation of ~10 wt.% phosphorus. In order to increase the phosphorus incorporation during electroless FeP deposition, a better understanding of the mechanism through which phosphorus is incorporated will be required. For the analogous system of electroless nickel phosphorus (NiP), numerous mechanistic studies on phosphorus incorporation have been performed and yet there is no consensus on the incorporation mechanism.[74-79] It is possible that the mechanism for phosphorus incorporation in the electroless FeP system is different than that for the electroless NiP system. It is thus proposed that an electrochemical study be undertaken in future work to unravel first the mechanism of P incorporation in electroless FeP deposition. Once such mechanistic knowledge is available, the process may be modified or optimized to facilitate high-P films with desired amorphous characteristics and improved corrosion resistance, micro-hardness and solderability.

APPENDIX A. Corrosion Resistance of Electrodeposited Amorphous Iron Phosphorous

Efforts to produce electroless amorphous iron phosphorous (FeP) deposits have up to this point been unsuccessful due to low phosphorus incorporation. In order to show that amorphous FeP film have improved corrosion resistance over metallic iron, FeP films with high concentrations of P can be electrodeposited from an electrolyte containing hypophosphite. In this appendix, the corrosion resistance of amorphous electrodeposited FeP films is shown to be higher than that of metallic iron.

A.1 Experimental Procedure

A.1.1 Materials and Electrolyte Composition

An electrolyte adapted from the work of Vitkova *et al.* was used for the electrodeposition of amorphous FeP.[80] The electrolyte contained 0.72 M ferrous

ammonium sulfate [$Fe(NH_4)_2(SO_4)_2 \cdot 6H_2O$, Fisher], 0.66 M sodium hypophosphite [$NaH_2PO_2 \cdot H_2O$, Sigma Aldrich], and 0.20 M boric acid [H_3BO_3, Acros] which served as a pH buffer. Electrolyte pH was adjusted to 1.6 using sulfuric acid [H_2SO_4, Fisher].

Electroless nickel phosphorus (NiP) was deposited using an electrolyte containing 0.10 M nickel sulfate [$NiSO_4 \cdot 6H_2O$, Sigma Aldrich], 0.20 M sodium hypophosphite [$NaH_2PO_2 \cdot H_2O$, Sigma Aldrich] as reducing agent, and 0.30 M sodium citrate [$Na_3C_6H_5O_7 \cdot 2H_2O$, Fisher Chemical] as complexant. The pH was adjusted to 9 using sodium hydroxide [NaOH, Fisher].

To determine the corrosion rate, both deposits were tested in a 3.5 wt.% sodium chloride [NaCl, Fisher] solution that contained 0.30 M sodium citrate [$Na_3C_6H_5O_7 \cdot 2H_2O$, Fisher Chemical] in order to facilitate dissolution and prevent the buildup of a passivating oxide layer. Millipore spec (18.2 MΩ) deionized (DI) water was used to prepare all electrolytes.

Gold plated quartz crystal microbalance (QCM) substrates (Fil-Tech) were used. The QCM quartz crystal electrodes were degreased with acetone and rinsed with DI water before use. The reference electrode was a saturated calomel electrode (SCE, Radiometer Analytical) and the counter electrode was a platinum wire electrode (Encompass).

A.1.2 Methods

Electrodeposition of FeP was performed on the gold plated quartz crystals in the FeP electrolyte described in section A.1.1 above. Films were deposited at a constant average current density of 100 mA/cm^2 for 15 minutes. NiP films were deposited via electroless deposition on the gold plated quartz crystal in the electrolyte described in section A.1.1. Electrolyte temperature was maintained at 90 ^oC using a heated jacketed cell. Electroless deposition time was 120 minutes.

Both prepared films, FeP and NiP, were corrosion tested at room temperature in the salt electrolyte described in section A.1.1. During dissolution, the mass loss of FeP and NiP was measured using the QCM. Phosphorus content was measured using energy-dispersive X-ray spectroscopy (EDS) and determined to be 10.1 at. % for FeP and 16.0 at. % for NiP. Both films were determined to be amorphous using X-ray diffraction (XRD).

A.2 Corrosion Rate of Electrodeposited Amorphous FeP

The mass loss of FeP submerged in a 3.5 wt. % sodium chloride solution is shown in Figure A.1. This rate of mass loss corresponds to a corrosion current density (i_{corr}) of 2.6 $\mu A/cm^2$. The mass loss for FeP is compared to the mass loss of NiP in the same test electrolyte (Figure A.1). The rate of mass loss of NiP was equivalent to i_{corr} = 0.9 $\mu A/cm^2$. Thus, the corrosion current of amorphous FeP is within the same order of magnitude as

amorphous NiP. Also, the FeP corrosion current is two orders of magnitude lower than typical corrosion current density of crystalline (pure) iron, *i.e.*, ~600 µA/cm^2.[68]

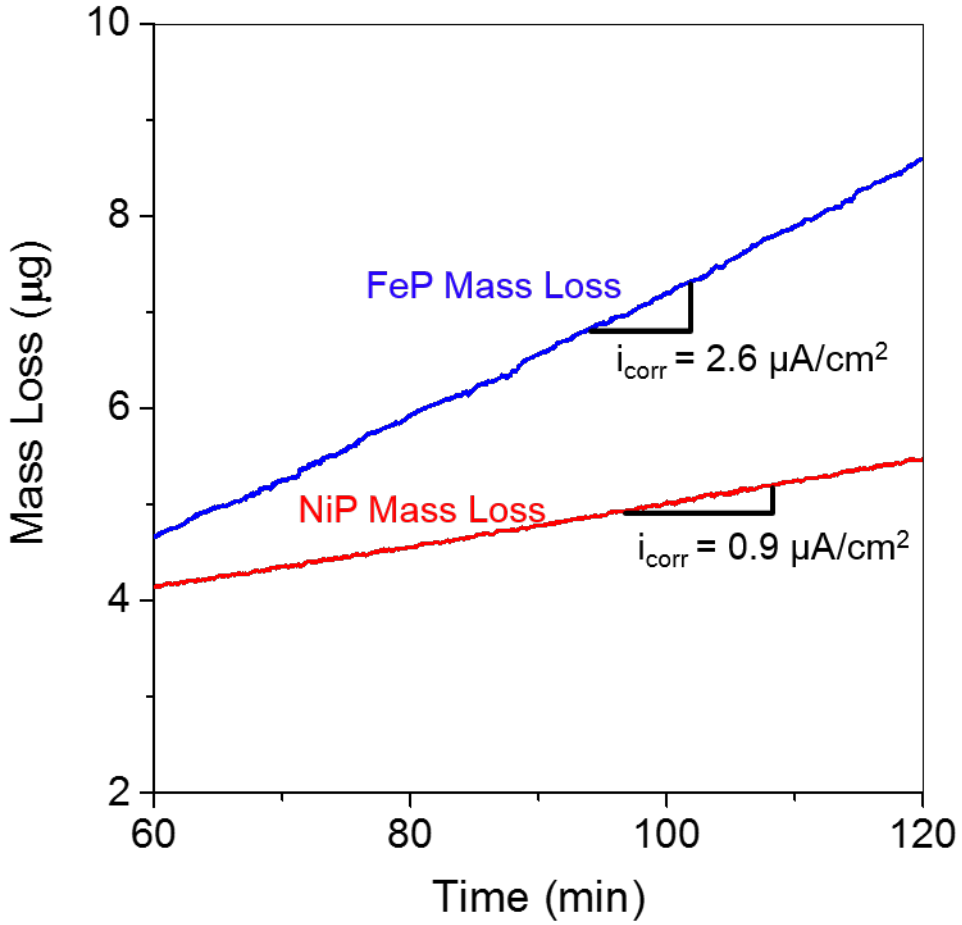

Figure A.1: Mass loss of amorphous FeP (*blue*) and NiP (*red*) in a 3.5 wt. % sodium chloride electrolyte measured using a QCM. Mass loss with time is converted into corresponding corrosion current densities (i_{corr}). The corrosion current density of FeP (i_{corr} = 2.6 µA/cm^2) is within an order of magnitude of the corrosion current density of NiP (i_{corr} = 0.9 µA/cm^2).

A.3 Conclusions

The corrosion resistance of electrodeposited (high P-content) amorphous FeP films was measured and shown to be similar to that of electroless-deposited amorphous NiP films. The corrosion resistance of amorphous FeP is markedly improved over typical corrosion resistance of pure iron. This high corrosion resistance renders these FeP films suitable for use in many processes where amorphous nickel is currently in use such as printed circuit boards.

BIBLIOGRAPHY

1. K. N. Tu, “Interdiffusion and reaction in bimetallic CuSn thin films”, *Acta Metall.*, **21**, 347 (1973).

2. P. Oberndorff, M. Dittes, L. Petit, C. Chen, J. Klerk, and E. Kluizenaar, “Tin whiskers on lead-free platings”, *Proc. Semiconductor Technology Symp. Advanced Packaging Technology II*, 51 (2002).

3. G. T. T. Sheng, C. F. Hu, W. J. Choi, K. N. Tu, Y. Y. Bong, and L. Nguyen, “Tin whiskers studied by focused ion beam imaging and transmission electron microscopy”, *J. Appl. Phys.*, **92**, 64 (2002).

4. W. Zhang, A. Egli, F. Schwager and N. Brown, “Investigation of Sn-Cu intermetallic compounds by AFM: new aspects of the role of intermetallic compounds in whisker formation”, *IEEE Trans. on Electronics Packaging Manufacturing*, **28**, 85 (2005).

5. J. Richardson, and B. Lasley, “Tin whisker initiated vacuum metal arcing in spacecraft electronics”, Proc. 1992 Government Microcircuit Applications Conference, **18**, 119 (1992).

6. Food and Drug Administration, “ITG #42: Tin whiskers- problems, causes and solutions”, http://www.fda.gov/ora/inspect_ref/itg/itg42.html, (1986).

7. United States Nuclear Regulatory Agency, “Accession number: 9907290189” (1999).

8. M. Anik, E. Körpe and E. Sen, “Effect of coating bath composition on the properties of electroless nickel–boron films”, *Surf. Coat. Tech.*, **202**, 2718 (2008).

9. J. L. Carbajal and R. E. White, “Electrochemical production and corrosion testing of amorphous Ni-P”, *J. Electrochem. Soc*., **135**, 2952 (1988).

10. Y. M. Chow, W. M. Lau and Z. S. Karim, “Surface properties and solderability behavior of nickel–phosphorus and nickel–boron deposited by electroless plating”, *Surf. Interface Anal.*, **31**, 321 (2001).

11. A. M. Elsherik and U. Erb, “Synthesis of bulk nanocrystalline nickel by pulsed electrodeposition”, *J. Mater. Sci.*, **30**, 5743 (1995).

12. K.M. Gorbunova, M V. Ivanov and V. P. Moiseev, “Electroless deposition of nickel-boron alloys”, *J. Electrochem. Soc.*, **120,** 613 (1973).

13. C. C. Hu and A. Bai, “Influences of the phosphorus content on physicochemical properties of nickel–phosphorus deposits”, *Mater. Chem. Phys.*, **77**, 215 (2003).

14. A. Ramalho and J. C. Miranda, “Friction and wear of electroless NiP and NiP + PTFE coatings”, *Wear*, **259**, 828 (2005).

15. B. D. Barker, “Electroless deposition of metals”, *Surf. Tech.*, **12**, 77 (1981).

16. W. O. Rogers, “Method for enhancing the solderability of nickel layers”, US Patent Number 4603805, (1986).

17. T. Schafer, E. Bohler, S. Ruhdorfer, L. Weigl, D. Wessner, B. Filipiak, H. E. Wichmann and J. Ring, “Epidemiology of contact allergy in adults”, *Allergy*, **56**, 1192 (2001).

18. J. P. Thyssen, A. Linneburg, T. Menne, and J. D. Johansen, “The epidemiology of contact allergy in the general population – prevalence and main findings”, *Contact Dermatitis*, **57**, 287 (2007).

19. E. Denkhaus and K. Salnikow, “Nickel essentiality, toxicity, and carcinogenicity”, *Crit. Rev. Oncol. Hemat.*, **42**, 35 (2002).

20. International Agency for Research on Cancer, “IARC monographs on the evaluation of carcinogenic risks to humans, chromium, nickel and welding”, *IRAC*, **49**, (1990).

21. Regulation (EC) No. 1907/2006 of The European Parliament and of the Council; website: www.eur-lex.europa.eu.

22. R. Balasubramaniam, *Story of the Dehli Iron Pillar*, p. 7, Foundation Books, Delhi (2005).

23. G. Wranglén, “The “rustless” iron pillar at Delhi”, *Corrosion Science*, **10**, 761 (1970).

24. R. Balasubramaniam, “On the corrosion resistance of the Delhi iron pillar”, *Corrosion Science*, **42**, (2000).

25. M. K. Ghosh, “The Delhi iron pillar and its iron”, *NML Technical J.*, **5**, 31 (1963).

26. R. Hadfield, “Discussion on Friend and Thorneycraft’s paper on ancient iron”, *J. Iron and Steel Inst.*, **112**, 233 (1925).

27. W. E. Bardgett and J. F. Stanners, “The Delhi iron pillar — a study of the corrosion aspects”, *J. Iron and Steel Inst*., **210**, 3 (1963).

28. J. C. Hudson, “The Delhi iron pillar”, *Nature*, **172**, 499 (1953).

29. Y. Ge, Z. Bangwei, W. Lingling, O. Yifang and X. Haowen, “Preparations and properties of amorphous Fe-Mo-B alloy deposits by chemical plating”, *J. Electrochem. Soc.*, **160**, D403 (2013).

30. W. Y. Hu and B. W. Zhang, “Electroless deposition of iron-boron alloys”, *T. I. Met. Finish.*, **71**, 30 (1993).

31. Y. Meng, L. L. Wang, G. F. Huang, W. Q. Huang and B. S. Zou, “The influence of Nd on the corrosion behavior of electroless-deposited Fe-P”, *Int. J. Mater. Res.*, **98**, 217 (2007).

32. L. L. Wang, L. H. Zhao, G. F. Huang, X. J. Yuan, B. W. Zhang and J. Y. Zhang, “Composition, structure and corrosion characteristics of Ni-Fe-P and Ni-Fe-P-B alloy deposits prepared by electroless plating”, *Surf. Coat. Tech.*, **126**, 272 (2000).

33. H. F. Zhou, J. D. Guo and J. K. Shang, “Electroless deposition of highly solderable Fe-Ni films”, *J. Electrochem. Soc.*, **160**, D233 (2013).

34. H. F. Zhou, J. D. Guo, Q. S. Zhu and J. K. Shang, “Application of electroless FeL42Ni(P) film for under-bump metallization on solder joint”, *J. Mater. Sci. Technol.*, **29**, 7 (2013).

35. Y. Luo, S. K. Kang, O. Jinka, M. Mason, S. A. Cordes and L. T. Romankiw, "Development of electroless nickel-iron plating process for microelectronic applications," *2014 IEEE 64th Electronic Components and Technology Conference (ECTC)*, Orlando, FL, 1782 (2014).

36. C. Ruscior and E. Croiala, “Chemical iron-phosphorus films”, *J. Electrochem. Soc.*, **118**, 696 (1971).

37. N. Fujita, A. Tanaka, E. Makino, P. T. Squire, P. B. Lim, M. Inoue and T. Fujii, "Fabrication of amorphous iron-boron films by electroless plating", *Appl. Surf. Sci.*, **113**, 61 (1997).

38. G. F. Huang, W. Q. Huang, L. L. Wang, Y. Meng, Z. Xie and B. S. Zou, "Electrochemical study of electroless deposition of Fe–P alloys", *Electrochim. Acta*, **51**, 4471 (2006).

39. G. F. Huang, W. Q. Huang, L. L. Wang, B. S. Zou, Q. L. Wang and J. H. Zhang, "Studies on the Fe-P film plating from a chemical bath: deposition mechanism and parameter effects", *Int. J. Electrochem. Soc.*, **3**, 145 (2008).

40. M. A. Dinderman, W. J. Dressick, C. N. Kostelansky, R. R. Price, S. B. Qadri and P. E. Schoen, "Electroless plating of iron onto cellulose fibers", *Chem. Mater.*, **18**, 4361 (2006).

41. L. Z. Li, W. C. Hu, Y. W. Zhang, X. B. Wan and L. Zhang, "Investigation of effect of additives on electroless iron deposition", *T. I. Met. Finish.*, **89**, 95 (2011).

42. X. Zhang, W. Han, D. Fan and Y. Zheng, "Electroless iron plating on pure magnesium for biomedical applications", *Mater. Let.*, **130**, 154 (2014).

43. Scientific Committee on Consumer Safety (SCCS), "Opinion on Boron compounds" *European Commission*, (2010).

44. P. J. Loferski and P. R. Neely "Platinum-Group Metals in January 2017" *USGS Mineral Industry Surveys January 2017*, 126 (2017).

45. P. J. Loferski, "Platinum-group metals, 2017", *USGS Mineral Commodities Summary*, 126, (2016).

46. P. J. Loferski, “Platinum-group metals, 2014”, *USGS 2014 Minerals Yearbook*, 57.1 (2016).

47. P. J. Loferski, “Platinum-group metals, 2012”, *USGS Mineral Commodities Summary*, 120, (2011).

48. P. J. Loferski, “Platinum-group metals, 2013”, *USGS Mineral Commodities Summary*, 120, (2012).

49. P. J. Loferski, “Platinum-group metals, 2014”, *USGS Mineral Commodities Summary*, 120, (2013).

50. P. J. Loferski, “Platinum-group metals, 2015”, *USGS Mineral Commodities Summary*, 120, (2014).

51. P. J. Loferski, “Platinum-group metals, 2016”, *USGS Mineral Commodities Summary*, 126, (2015).

52. T. R. Yager, Y. Soto-Viruet, and J. J. Barry, “Recent strikes in South Africa’s platinum-group metal mines—effects upon world platinum-group metal supplies”, *U.S. Geological Survey Open-File Report 2012–1273*, 18 (2012).

53. M. L. Zientek, J. D. Causey, H. L. Parks, and R. J. Miller, “Platinum-group elements in southern Africa—mineral inventory and an assessment of undiscovered mineral resources”, *U.S. Geological Survey Scientific Investigations Report 2010–5090–Q*, 126 (2014).

54. T. L. Humby, “Redressing mining legacies: the case of the South African mining industry”, *J. of Business Ethics*, **135**, 653 (2016).

55. C. Wagner and W. Traud, “Über die Deutung von Korrosionsvorgängen durch Überlagerung von elektrochemischen Teilvorgängen und über die Potentialbildung an Mischelektroden”, *Z. Elektrochem.*, **44**, 391 (1938).

56. I. Ohno, “Electrochemistry of electroless plating.” *Mat. Sci.and Eng.: A* **146.1-2**, 33 (1991).

57. L. Yu, L. Guo, R. Preisser, and R. Akolkar, “Autocatalysis during electroless copper deposition using glyoxylic acid as reducing agent”, *J. Electrochem. Soc.*, **160**, 3006 (2013).

58. P. Bindra and J. Roldan, “Mechanisms of electroless metal plating. III. Mixed potential theory and the interdependence of partial reactions”, *J. Appl. Electrochem.*, **17**, 1254 (1987).

59. G. Salvago, P.L. Cavallotti, “Characteristics of the chemical reduction of ni alloys with hypophosphite” *Plating*, **59**, 665 (1972).

60. R. M. Lukes. “The mechanism for the autocatalytic reduction of nickel by hypophosphite ion.”, *Plating*, **51**, 969 (1964).

61. J. Blickensderfer, P. Altemare, K. O. Thiel, H. J. Schreier and R. Akolkar, “Direct electroless plating of iron-boron on copper” *J. Electrochem. Soc.*, **161**, D495 (2014).

62. S. Nakahara and Y. Okinaka, “Microstructure and ductility of electroless copper deposits”, *Acta Metall.*, **31**, 713 (1983).

63. R. Schrader and G. Buttner, “Untersuchungen über γ-eisen (III)-oxid”, *Z. Anorg. Allg. Chem.*, **320**, 205 (1963).

64. A. M. Berger, “The crystal structure of boron oxide”, *Acta Chem. Scand.*, **7**, 611 (1953).

65. H. E. Swanson and E. Tatge, “Standard X-ray diffraction powder patterns”, *Natl. Bur. Stand.*, **1**, 359 (1953).

66. R. C. Agarwala and V. Agarwala, “Electroless alloy/composite coatings: A review”, *Sadhana-Acad. P. Eng. S.*, **28**, 475 (2003).

67. M. Schlesinger, “Electroless Deposition of Nickel” in *Modern Electroplating*, 5th ed., M. Schlesinger and M. Paunovic, Editors, p. 447, John Wiley & Sons, Hoboken (2010).

68. V. S. Rao, "A review of the electrochemical corrosion behaviour of iron aluminides.", *Electrochimica Acta*, **49**, 4533 (2004).

69. M. Paunovic, “Electroless deposition of Copper” in *Modern Electroplating*, 5th ed., M. Schlesinger and M. Paunovic, Editors, p. 443, John Wiley & Sons, Hoboken (2010).

70. F. Pearlstein and R. F. Weightman, “Electroless cobalt deposition from acid baths”, *J. Electrochem. Soc.*, **121**, 8 (1974).

71. A. J. Bard and L. R. Faulkner, *Electrochemical Methods: Fundamentals and Applications*, 2nd ed., p. 99, John Wiley & Sons, Hoboken (2001).

72. J. Newman and K. E. Thomas-Alyea, *Electrochemical Systems*, 5th ed., p. 205, John Wiley & Sons, Hoboken (2004).

73. J. J. Lingane, “Polarographic investigation of oxalate, citrate and tartrate complexes of ferric and ferrous iron”, *J. of the Amer. Chem. Soc.*, **68**, 2448 (1946).

74. L. M. Abrantesa and J. P. Correia, “On the mechanism of electroless Ni-P plating”, *J. Electochem. Soc.*, **141**, 2356 (1994).

75. B. J. Hwang and S.H. Lin, “Reaction mechanism of electroless deposition: observations of morphology evolution during nucleation and growth via tapping mode AFM”, *J. Electochem. Soc.*, **142**, 3749 (1995).

76. J. Van Den Meerakker, “On the mechanism of electroless plating. II. One mechanism for different reductants”, *J. Appl. Electrochem.*, **11**, 395 (1981).

77. G. O. Mallory, in *Electroless Plating: Fundamentals and Applications,* G. O. Mallory and J. B. Hajdu, Editors, p. 8, Noyes Publications, Norwich (1990).

78. A. P. Ordine, S. L. Diaz, I. C. P. Margarit, O. E. Barcia, and O. R. Mattos, “Electrochemical study on Ni–P electrodeposition”, *Electrochemica Acta*, **51**, 1480 (2006).

79. X. Liu, W. Richtering, R. Akolkar, “Investigation of the kinetics and mass transport aspects of hydrogen evolution during electroless deposition of nickel–phosphorus”, *J. Electochem. Soc.*, **164**, D498 (2017).

80. S. Vitkova, M. Kjuchukova and G. Raichevski, “Electrochemical preparation of amorphous Fe-P alloys”, *J. Appl. Electrochem.*, **18**, 637 (1988).